Thesis for plag check (1).docx

by Arpit GOYAL

Submission date: 16-Mar-2025 06:11PM (UTC+0530)
Submission ID: 2615903482
File name: Thesis_for_plag_check_1_.docx (27.51M)
Word count: 40609
Character count: 242980

Chapter 1

Introduction

1.1 Background of the study

In recent years, outdoor and indoor air pollution has become a significant global concern, threatening environmental sustainability and public health. The swift growth in urbanization, industrialization, and dependency on fossil fuels has intensified outdoor air pollution, whereas contemporary lifestyle and modern building designs are responsible for heightened concentrations of indoor air pollutants. Overall, these pollutants degrade air quality and exert considerable socio-economic and health-related repercussions [1], [2].

Outdoor air pollution is defined by the presence of hazardous compounds like nitrogen oxides (NO_x), carbon monoxide (CO), sulfur dioxide (SO_2), volatile organic compounds (VOCs), and particulate matter (PM) in the outdoor environment. According to the report by the World Health Organization (WHO) [3], [4], ambient air pollution is responsible for over 4.2 million premature deaths each year, classifying it as a primary environmental risk factor for mortality. One of the world's most polluted cities is New Delhi, India, where extremely high levels of $PM_{2.5}$ and PM_{10} frequently surpass WHO-recommended safe thresholds. The principal contributors to pollution comprise industrial operations, automobile emissions, construction activities, and periodical rural stubble burning in nearby states [5]–[7]. A study by the Centre for Science and Environment [8–10] indicated that extended exposure to air pollution in Delhi results in respiratory disorders, heightened cardiovascular risks, decreased lung functioning, and potential cognitive disorders (Figure 1.1). Despite implementing measures such as enhanced public transportation, odd-even traffic rules, and launching more sustainable fuel standards, the city still faces significant air quality challenges [8].

Similarly, indoor air pollution is equally detrimental despite its lack of visibility. Indoor contaminants originate from tobacco smoke, burning of solid fuels, microbial agents including mold and bacteria, and volatile chemicals in household products. The situation is especially significant in low to middle-class-income countries such as Sub-Saharan Africa, where conventional cooking practices employing biomass fuels lead to elevated indoor particulate

matter levels [9], [10]. As per the report given by WHO [11], [12], exposure to indoor smoke resulted in over 400,000 deaths each year in these parts of the world, predominantly affecting women and children who are close to cooking fires. Nevertheless, developed nations are also not immune to the issue as modernly designed buildings constructed for energy efficiency frequently entrap these pollutants, increasing their concentrations. Indoor air pollution has adverse health consequences (represented in Figure 1.1.) that include chronic obstructive pulmonary disease (COPD) and acute respiratory infections, as well as long-term risks such as cancer and neurological disorders [13], [14].

Air pollution is a worldwide issue because of its adverse health effects and extensive impact on several societal domains, including social behavior, technology, education, economics, politics, and governance. Outdoor air pollution influences climate change via greenhouse gas emissions, and particulate matter impacts regional weather patterns and visibility [15]. On the other hand, indoor air pollution disproportionately affects vulnerable populations, such as older adults, children, and individuals with existing medical conditions [16]. Furthermore, the economic impact of air pollution is significant, covering healthcare costs, decreased working efficiency, and adverse ecological effects [17], [18].

Initiatives to address outdoor and indoor air pollution have been made, such as government regulations, technological advancements, and public education efforts. International agreements, including the Paris Climate Accord, seek to reduce emissions, while innovations in air purification systems and architectural ventilation techniques provide potential solutions for indoor environments [19]. Despite these initiatives, substantial challenges persist, including imperfections in policy implementation, technological availability, and public acceptance.

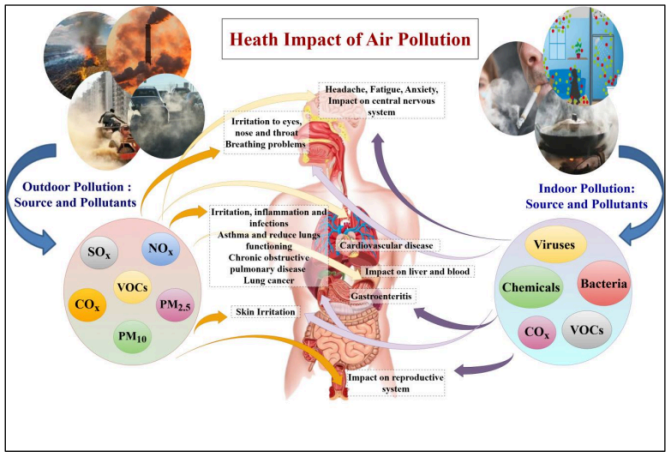

Figure 1.1 Impact of indoor and outdoor air pollution on human health

1.2 Indoor Air Pollution: Bioaerosols and Hospital Acquired Infections (HAIs)

Bioaerosols are a key category of indoor pollutants, distinguished by their unique properties and substantial health impacts. They are defined as airborne biological particulates comprising bacteria, fungi, viruses, and pollen that emerge from living organisms, and different environmental resources. In contrast to chemical pollutants, bioaerosols could stay viable and proliferate under favorable conditions, rendering them persistent and challenging to manage. Their involvement in transmitting contagious diseases, inducing allergic responses, and worsening respiratory problems emphasizes their significance as a major public health issue [20], [21].

The significance of bioaerosols among indoor air pollutants can be demonstrated by their capacity to impact human health substantially. For example, the COVID-19 pandemic considerably raised awareness of bioaerosols as an agent for disease transmission. SARS-CoV-2, the virus that causes the epidemic of COVID-19, is predominantly transmitted by respiratory

droplets and aerosols in enclosed environments. Research [22] indicates that super-spreader incidents were frequently seen in inadequately ventilated environments, including meeting rooms and public transportation. Similarly, hospital-acquired infections (HAIs) constitute a primary global concern, with bioaerosols substantially contributing to their transmission.

HAIs, also called nosocomial infections, are infections that patients encounter during their hospitalization that were neither present nor incubated during admission. These infections typically appear 48 hours or more post-hospitalization and may affect different body parts, including the surgical areas, bloodstream, respiratory system, and urinary tract [23], [24].

HAIs are predominantly induced by pathogens such as viruses, fungi, and bacteria that flourish in medical environments. Typical infection agents comprise *Escherichia coli*, *Staphylococcus aureus* (notably methicillin-resistant *S. aureus*, or *MRSA*), *Pseudomonas aeruginosa*, and *Klebsiella pneumoniae* [25]–[27]. These microorganisms propagate via infected medical instruments, inappropriate sanitation of the hands, poor sterilizing protocols, and airborne transmission. Aspects such as overcrowded healthcare facilities, extended utilization of invasive apparatus like ventilators, and improper usage of antibiotics increase the risk of HAIs. The chain of transmission of HAIs is illustrated in Figure 1.2, along with the symptoms that can be used to identify the infection.

HAIs can cause an immense burden on a global scale, impacting millions of patients every year. The WHO predicts that more than 7% of hospitalized patients in high-income nations and 10% in low- and middle-income nations get at least one healthcare-associated infection [28]. Additionally, due to inadequate infection control strategies, the infection rate could exceed 25% in low-resource/ low-income nations [29]. Thus, HAIs represent a significant risk to patient safety, extending hospitalizations, escalating healthcare expenditures, and resulting in elevated mortality and morbidity rates globally. For example, an analysis conducted across European nations showed that HAIs resulted in approximately 16 million extra hospitalizations per year, with over 37,000 related fatalities [28]. In developing countries, HAIs adversely affect vulnerable populations, particularly infants, with neonatal infections responsible for up to 75% of neonatal fatalities in certain areas [28], [30]. In addition to affecting human health, HAIs worsen the worldwide antibiotic resistance conflict by increasing the prevalence of multidrug-resistant pathogens.

The situation is especially concerning in undeveloped and emerging nations such as India, where resource limitations, inadequate healthcare facilities, and shortage of effective infection control techniques are communal and, thus, intensify the situation. Inadequate ventilated infrastructure, overcrowded wards, and poor sanitizing techniques accelerate the spread of bioaerosols in these environments. Research performed in Indian hospitals during the COVID-19 pandemic [31] indicated higher concentrations of infectious virus in inadequately ventilated wards, resulting in outbreaks among healthcare personnel and patients.

Resolving the interconnected challenges of HAIs and bioaerosols necessitates an extensive understanding of existing technology and their constraints. Technologies like ultraviolet germicidal irradiation (UVGI), high-efficiency particulate air (HEPA) filtration, and improved ventilation have demonstrated efficacy in mitigating the risk of airborne transmission [32]. Although these approaches effectively eliminate specific pollutants such as particulate matter and bioaerosols, they frequently require considerable energy consumption and maintenance, hence constraining their scalability in resource-limited environments, especially in low- and middle-income countries. Recognizing these limitations highlights the necessity for novel, sustainable, and affordable technology to reduce indoor air pollution successfully. Future studies and policy initiatives must emphasize integrated strategies that utilize renewable energy, circular economy concepts, and community involvement to guarantee equitable and environmentally friendly solutions for global air quality improvement.

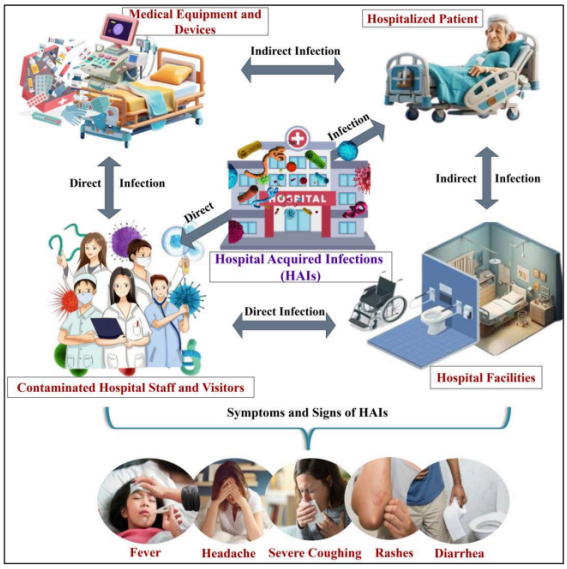

Figure 1.2 The transmission chain of HAIs and the symptoms that aid in identifying the infection.

1.3 Technologies Available For Air Purification

1.3.1 Advanced Oxidation Process: TiO_2- assisted Photocatalysis

The growing global concerns about indoor and outdoor air pollution have prompted considerable focus on developing innovative air treatment techniques. As discussed, airborne pollutants, such as VOCs, bioaerosols, and fine particulate matter, present significant risks to human health and the environment. Conventional air purification techniques, including adsorption, filtration, and chemical cleansing, frequently exhibit constraints in entirely degrading contaminants, resulting in secondary contamination or buildup. Therefore, Advanced oxidation processes (AOPs) have emerged as a viable alternative for effective air purification processes, as they can mineralize different pollutants into harmless byproducts such as water (H_2O) and carbon dioxide (CO_2) [33].

Photocatalysis is recognized as an efficient and environmentally friendly method for air treatment among different AOPs available. It refers to the activation process of semiconductor compounds through light, resulting in the generation of reactive oxygen species (ROSs), including superoxide anions ($\bullet O_2^-$) and hydroxyl radicals (•OH), capable of oxidizing both organic and inorganic contaminants. The advancement of nanotechnology has led to the emergence of unique semiconductor nano-compounds, including TiO_2 [34], ZnO [35], ZnS [36], CdO [37], and Bi_2O_3 [38], for efficiently treating air contaminants when coupled with other approaches. Since titanium oxide (TiO_2) is inexpensive, nontoxic, highly stable, and photosensitive, it has been extensively researched among various semiconducting photocatalytic materials [39]. Exposure of TiO_2 to ultraviolet (UV) light results in the generation of electron-hole (e^-/h^+) pairs, which initiates a redox reaction that leads to the degradation of contaminants in the air (Figure 1.3).

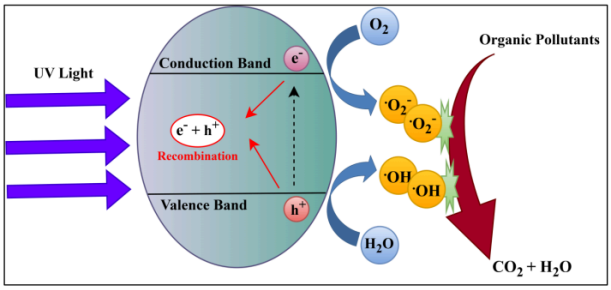

Figure 1.3 TiO_2 photocatalytic process under UV irradiations and (e^-/h^+) pair recombination limitation.

TiO_2-based photocatalysis effectively eliminates pathogenic microbial organisms, SO_x, NO_x, and VOCs in air treatment applications. Research indicates its potential to entirely oxidize airborne contaminants under optimal conditions [40]. It has three crystal structures: anatase, rutile, and brookite. The anatase type is more widely used because it has a higher photoactivity than the other types of TiO_2. However, its photocatalytic efficacy is limited by the fast recombination rate of e^-/h^+ pairs [41], as depicted in Figure 1.3 under UV light.

Furthermore, the wide band gap energy of 3.2 eV for the anatase phase of TiO_2 restricts its application in the visible light spectrum [42]. Considerable studies have been dedicated to improving the photocatalytic efficiency of TiO_2 in the visible light spectrum by the introduction of metal dopants or deposits, sensitization with organometallic dyes, and integration with smaller band gap semiconductor compounds like WO_3, Fe_2O_3, and Bi_2O_3 [43]–[45]. The hybridization of semiconductor nanomaterials results in the formation of a novel energy level, facilitating the separation of charge carriers and improving the photocatalytic efficiency in the visible light spectrum.

With a bandgap of 2.1 eV, hematite (α-Fe_2O_3) is the most thermally stable form of iron oxide, ecologically suitable, widely accessible, inexpensive, and highly corrosion-resistant [46]. The distinctive characteristics of α-Fe_2O_3 render it a viable candidate for integrating with TiO_2. Nanocomposite materials of TiO_2 and Fe_2O_3 are synthesized using well-established physical and chemical techniques such as hydrothermal, sono-chemical, sol-gel, solvo-thermal, and mechano-chemical synthesis [47]. The developed Fe_2O_3/TiO_2 heterojunction nanoparticles have also been used in several environmental applications, including wastewater treatment, NO_x, SO_x, CO_x, and VOCs removal from polluted air [48]–[52]. But these methods necessitate using hazardous chemicals like organic solvents, pluronic, etc., and templating agents like sodium dodecyl sulfate (SDS) [48], [53] and pluronic 123 [52], [54], [55] under adverse circumstances. These techniques produce toxic and potentially harmful unwanted products like formaldehyde and need significant energy and economic expenditure. Also, there is limited research on treating bioaerosols in indoor environments using visibly-active Fe_2O_3/TiO_2 heterojunction photocatalytic material. Table 1.1 presents some typical examples of photocatalytic systems involving Fe_2O_3/TiO_2 heterojunction photocatalytic materials used for different environmental remediations. Up to now, only a limited number of scientific studies have been conducted to synthesize this remarkable nanomaterial using environmentally friendly/green techniques.

Furthermore, incorporating TiO_2 into building materials, including cement and coatings, has broadened its applicability for extensive use in indoor and outdoor environments. Thus, these photocatalytic surfaces effectively reduce airborne contaminants and demonstrate self-cleaning and antibacterial capabilities, rendering them beneficial for sustainable building design (Pacheco-Torgal et al., 2013). While significant advancements have been made, an extensive

understanding of involved reaction mechanisms, material properties improvement, and long-lasting durability evaluation are essential for the broader implementation of TiO_2-based photocatalysis in construction materials. Hence, the present study seeks to investigate and improve the applications of TiO_2 photocatalysis for air treatment, emphasizing resolving existing constraints and increasing efficiency in practical environments. This research aims to develop an eco-friendly and efficient air purification technology by integrating innovative materials and techniques.

Table 1.1 Examples of photocatalytic systems utilizing Fe_2O_3/TiO_2 heterojunction photocatalytic materials for air purification.

Nanomaterial	Stimulation	Application	Reference
Fe_2O_3/TiO_2 heterostructure	UV light-induced oxygen activation	AsH_3 removal with 98.6% efficiency	[56]
n-n TiO_2/α-Fe_2O_3 branched heterostructure	--	Manufacturing of conductometric acetone gas sensors with a high response rate of 21.9.	[57]
Eco-friendly α-Fe_2O_3/TiO_2 heterojunction	Visible light	Decomposition of organic dye with improved cycling characteristics.	[48]
β-FeOOH/Fe-TiO_2 heterojunction on Ti	Visible light	Antibacterial, Anti-inflammation, and improved sealing in an *S. aureus* infection model. Lab-scale practice.	[58]
Ag, Pd, and Fe modified TiO_2	Black Light irradiation	Heterogeneous photocatalytic reactor for the inactivation of three airborne bacteria: *Escherichia coli*, *Bacillus subtilis*, and *Staphylococcus aureus*.	[59]–[61]

1.3.2 Photocatalytic Construction Material For Air Purification

The research scientists are trying to explore eco-friendly and novel strategies across different societal domains to prevent and treat airborne contamination hazards. One option is to utilize photocatalytic construction materials, providing in-situ treatment with fewer economic constraints. Nanomaterials like SiO_2, TiO_2, Al_2O_3, ZnO, carbon nanofibers, etc., have been utilized in cement-based materials to have more durable infrastructures [62]–[64]. Also, among the above-stated nanomaterials, TiO_2 is the most broadly utilized photocatalyst, with researchers developing "smart construction materials" such as TiO_2-coated ceramic tiles [65]–[67],

pavement blocks, roof, and window glasses [68]–[71]. These sorts of items are now commercially accessible and have been confirmed as one of the promising operations to mitigate urban contaminants without necessitating extra energy consumption [72]–[75]. Thus, photocatalytic building materials are recognized for enhancing air quality passively and sustainably.

Numerous researches have proven the efficacy of these photocatalytic construction materials in treating outdoor air contaminants. For example, Fang M. et al. (2021) [76] documented a reduction of 25% in NO_x concentration in regions with TiO_2-coated pavements. Similarly, Lee et al. (2022) [77] showed substantial VOC breakdown with photocatalytic concrete panels under a modeled urban environment. A pilot experiment in Milan, Italy, employed TiO_2-coated concrete in a residential area, reducing ambient NOx concentrations significantly [78]. A study conducted in Delhi, India, indicated that using photocatalytic pavement tiles can potentially diminish ground-level ozone and particulate matter concentrations, thus enhancing air quality in one of the world's most polluted cities [79]. Therefore, these research results highlight the capacity of photocatalytic building materials to improve urban air quality and promote better community health.

Additionally, due to the advancements in nanotechnology, modifying building materials with multi-functional photocatalytic coatings is evolving as a groundbreaking technique. These coatings incorporate supplementary features, including self-cleaning, self-disinfecting, antimicrobial properties, and different contaminant degradation [80]–[82]. Considering the abundance of literature on outdoor air purification with these materials, there is a shortage of studies concerning indoor air applications. Table 1.2 presents some illustrative examples of photocatalytic building materials utilized for indoor air treatment. Designing sustainable and affordable techniques for integrating these materials into infrastructure is essential for their extensive adoption. For instance, applying sol-gel technology and sophisticated spray deposition methods has enabled the installation of photocatalytic coatings over vast surfaces, guaranteeing uniformity and efficacy [83].

While promising, conventional photocatalytic construction materials (mentioned in Table 2) encounter limitations such as inadequate performance under visible light spectrum or low-light conditions and issues related to long-term durability. Also, TiO_2-coated photocatalytic building

materials have primarily been used for outdoor applications, indicating their activity under the UV light spectrum. Extending their wavelength to the visible light spectrum presents significant challenges, accompanied by financial and technological costs. Thus, the research area concerning using visibly active photocatalytic construction materials for indoor microbial disinfection remains underexplored and limited.

Table 1.1: Illustrative examples of photocatalytic building materials employed for indoor air purification.

Photocatalytic Building Material	Stimulation Under	Employed For	Reference
TiO_2-coated ceramic filter	Black light lamps	Air purifier filter for medical indoor environments, Air disinfection (bacteria, viruses) and purification (VOCs).	[84]
Glass-supported TiO_2 thin film	UV	Air purifying prototype for residential indoor air quality, Air disinfection (bacteria, viruses), and purification (VOCs).	[85]
Cu^{2+} and Fe^{3+} nanocluster-grafted TiO_2	White fluorescent light	Air purification and disinfection. Product (tile and film) subjected to Field-scale testing.	[86]
Fabric filter-supported Ag-doped TiO_2 thin film.	UV	Indoor air purification device for bio-terrorism defense and air Disinfection (bacteria, viruses, and fungi).	[87]
Glass-supported thin film of Ag-TiO_2, Pd-TiO_2, Fe-TiO_2.	Black light lamps	Air disinfection, Lab-scale photocatalytic reactor.	[88]

1.4 Sustainable Building Materials: Usage of Iron-rich Industrial Waste Products

Previously discussed photocatalytic scientific solutions do not align with the current need for sustainable and environmentally friendly solutions. As discussed before, the primary limitation of traditional TiO_2-assisted photocatalytic construction materials is that their activity is restricted to the UV light spectrum, rendering them unsuitable for visible light applications in indoor environments. Various nanotechnological advancements offer modification techniques to enhance the band gap energy of TiO_2 [89], [90]; however, it raises production costs,

compromising the technique's sustainability and low energy consumption. In light of this, the present study proposes using iron-rich industrial waste materials (IWPs) as natural or in-situ heterojunction formation agents in developing photocatalytic construction materials. This approach seeks to fabricate a visibly active Fe_2TiO_5 heterostructure material that demonstrates photocatalytic and antimicrobial characteristics, as elaborated in the subsequent section 1.4. The proposed technique aims to develop a sustainable, cost-effective, and novel method for degrading the urban indoor microbial environment, incorporating circular economy principles.

The construction sector contributes to worldwide ecological problems, such as the depletion of natural resources and solid waste. At the same time, industrial operations globally generate approximately 13 billion tons of waste (such as silica fume, waste glass, plastic waste, gypsum waste, bottom ash etc.) every year, with a considerable fraction remaining underutilized, resulting in adverse environmental consequences [91]. This waste generally ends up in landfills or unmanaged dumps, contaminating soil and groundwater and releasing toxic gases. The effective use of these industrial waste products has become a key focus in sustainable development initiatives. Amongst these, the usage of IWPs has grown significantly due to their diverse applications in environmental remediation and construction practices [92].

Major categories of IWPs consist of fly ash (FA) (global production of approximately 750 million tons annually), steel slag (160 million tons), blast furnace slag (BS) (300 million tons), foundry sand (FS) (100 million tons), and red mud (120 million tons) [93]–[95]. If untreated, these waste materials may lead to leachate contamination, greenhouse gas emissions, and the depletion of valuable resources. For example, inappropriate handling of FA contributes to air and water contamination due to its fine particulate nature and the leaching of heavy metals [96]. Unsupervised BS can similarly result in an emission of sulfur-based compounds, which contribute to soil acidification [97]. The disposal of FS also presents ecological issues due to residual binders and additives, which can potentially leach toxic chemicals into the surrounding environment [98].

The significant production of these IWPs and environmental impacts have led to incorporating these materials in sustainable construction practices as a viable solution. These IWPs exhibit distinct physical and chemical properties and provide notable benefits, such as increased pozzolanic activity, better sorption capacity, and improved durability [99]. In the building

industry, these waste materials can substitute traditional raw materials, facilitating the advancement of sustainable cementitious composites, concrete, and geopolymer. For example, FA, a byproduct of the coal industry, has been extensively studied as a partial substitute for Portland cement. Cement manufacturing contributes roughly 8% of global CO_2 emissions [100], and including FA can remarkably decrease this percentage. Research demonstrates that substituting 10-20% of cement with FA can reduce CO_2 emissions by 25%, enhancing cementitious materials' durability and strength properties [101]. Similarly, BS, a byproduct of the steel industry, enhances cement mortar performance and decreases emissions—a 50% substitution of cement results in a 40% drop in carbon emissions [102]. Foundry sand (FS), characterized by its high silica content, is a sustainable alternative to natural sand in concrete, cement mortar, and asphalt mixtures [103]. In addition to keeping industrial waste materials off landfills, this approach lowers emissions and energy expenditure throughout the material production process. Thus, integrating these waste products into the building process diminishes the environmental impact of waste disposal and reduces the need for virgin raw materials, thereby successfully tackling the dual concerns of waste management and sustainable construction.

Besides the construction applications, IWPs also demonstrate significant efficiency in environmental remediation. Their higher surface area, porosity, and chemical affinity render them suitable for adsorption-based applications in wastewater treatment. For instance, modified red mud has been used to extract heavy metals from industrial wastewater, including arsenic, phosphate, and chromium [104]. Steel slag has been employed to neutralize acidic drainage from mine industries and to eliminate pollutants, including lead and cadmium, from wastewater [105]. These materials can also potentially improve soil stability and carbon sequestration and exhibit catalytic functions for pollution control. For example, few studies have investigated the potential of FA and FS as low-cost iron (Fe) substitute sources for wastewater treatment applications, especially concerning their catalytic application [106]–[109]. Thus, IWPsmexhibit multifunctionality and efficacy, establishing them as promising materials for sustainable development. Their implementation in environmental remediation and construction practices coincides with worldwide ecological sustainability plans.

While a majority of research indicates the potential of these IWPs in sustainable building practices; however, challenges persist regarding their environmental impact, economic viability, and role as a pollutant-degrading agent. The present research addresses these gaps by analyzing the mechanical, environmental, and financial attributes of using FA, BS, and FS in producing sustainable and photocatalytic Fe_2TiO_5 heterostructure materials. The study investigates the innovative usage of IWPs, highlighting their potential as transformative agents for long-term viability. Hence, the present research advances circular economy principles and reduces reliance on virgin resources, contributing to developing green building practices and supporting global sustainability objectives.

1.5 Proposed Technology: Indoor Air Treatment using Fe_2TiO_5 Heterostructure for Cementitious Composite

The present research paper presents a pragmatic visible light-responsive antimicrobial sustainable system that utilizes an innovative, in-situ, and naturally occurring heterojunction formation concept to produce a surface-active Fe_2TiO_5 heterostructure for cementitious composite, all within an economically feasible range. The study seeks to develop an iron-rich, sustainable cementitious composite. Consequently, it employs an inert composition of three IWPs: FA, BS, and FS. These waste products were substituted with cement and sand in varying proportions to encourage a circular economy and green building practices. The resulting sustainable cement-based building material was outer-coated with photocatalyst TiO_2. Subsequently, the material experiences a temperature-time treatment process, resulting in a naturally occurring surface-active Fe_2TiO_5 heterojunction outer layer on the sustainable cementitious material. Thus, the fabricated Fe_2TiO_5 heterostructure maintains its structural integrity while exhibiting enhanced photocatalytic and antimicrobial properties under the visible light spectrum. Hence, this Fe_2TiO_5 heterostructure for cementitious composite can be used to create smart coatings, making it an excellent choice for indoor microbial treatment applications.

The principal objective is to design and manufacture a sustainable, real-time product that is economical and efficient in mitigating microbial load in an indoor-urban environment. Thus, the developed method is relatively cost-effective, as only a minimal investment was required to modify the photocatalyst and cast the construction material. Therefore, the present work's originality lies in the fact that this concept's implementation within the construction sector has

not been documented as of yet. Furthermore, no literature report has yet documented the application of this particular heterostructure composite material to treat indoor microbial contamination.

The proposed Fe_2TiO_5 heterostructure also resolves the problem of electron-hole recombination in the TiO_2 photocatalytic technique by the reaction of the photo-excited electrons (e^-) being captured by Fe^{3+} ions during the TiO_2 photocatalytic process. This results in the creation of Fe^{2+} ions (equation (3)), which in turn enhances the photocatalytic process, as demonstrated in equations (1.1) to (1.11). A detailed discussion of the same is carried out in the results and discussion chapter section (4.2) of the present research study. The generated radical ions facilitate the inactivation process of bioaerosols by utilizing Fe_2TiO_5 heterostructure composite materials in indoor environments.

$$TiO_2 + hv\ (viisble\ irradiation) \rightarrow e^- + h^+ \quad \textbf{1.1}$$

$$h^+ + H_2O \rightarrow H^+ + \dot{O}H \quad \textbf{1.2}$$

$$Fe^{3+} + e^- \rightarrow Fe^{2+} \quad \textbf{1.3}$$

$$Ti^{3+} \rightarrow e^- + Ti^{4+} \quad \textbf{1.4}$$

$$Fe^{2+} + O_{2(abs)} \rightarrow Fe^{3+} + \dot{O}_2^- \quad \textbf{1.5}$$

$$Fe^{2+} + Ti^{4+} \rightarrow Fe^{3+} + Ti^{3+} \quad \textbf{1.6}$$

$$Fe^{3+} + h_{vb}^+ \rightarrow Fe^{4+} \quad \textbf{1.7}$$

$$Fe^{3+} + hv \rightarrow Fe^{4+} + e^- \quad \textbf{1.8}$$

$$Fe^{4+} + OH^- \rightarrow Fe^{3+} + \dot{O}H \quad \textbf{1.9}$$

$$e^- + O_2 \rightarrow \dot{O}_2^- \quad \textbf{1.10}$$

$$\dot{O}_2^- + e^- + H^+ \rightarrow H_2O_2 \quad \textbf{1.11}$$

At the same time, this study aims to apply the circular economy principle to processing IWPs to conserve natural resources, reduce the environmental impact of metal casting waste, and achieve a zero-waste goal. Hence, the present research tackles multiple ecological challenges within a single antimicrobial system. Thus, in light of the scarcity of literature concerning using photocatalytic cement-based building materials to remediate indoor microbial contamination, the current study examines the efficacy of the cast surface-active Fe_2TiO_5 heterostructure for cementitious composite in neutralizing bioaerosols. The findings of this research demonstrate the

viability of implementing waste materials as a viable and substantive approach to treat domestic microbial contamination. This is the first study to document an in-situ photocatalytic process that is visibly active and effectively deactivates bioaerosols.

1.6 Selected Microorganism for the Study

The current research utilized *Escherichia coli (E. coli)* to investigate the antimicrobial efficiency of the Fe_2TiO_5 heterostructure for cementitious composite. *Escherichia coli (E. coli)*, a Gram-negative bacteria commonly found in the human gastrointestinal microbiome, is acknowledged for its dual role as a commensal and pathogenic organism. Under typical circumstances, *E. coli* facilitates the proper functioning of the digestive system; however, certain strains, including *enteropathogenic*, *uropathogenic*, and *enterohemorrhagic E. coli*, can induce severe health conditions [110]. These strains are not only difficult to treat but have also been linked to increasing mortality rates. In addition to foodborne and waterborne transmission, recent research has emphasized the potential of *E. coli* as a bioaerosol, a sort of microbial contamination observed in airborne particulate matter [111]. This poses significant challenges, especially in medical facilities where immunocompromised patients are at greater risk [112]. Following inhalation or deposition on the mucous membranes, pathogenic *E. coli* strains can induce urinary and respiratory tract infections, gastroenteritis, and sepsis [111]. Inhaling *E. coli* bioaerosols could worsen pre-existing respiratory illnesses, including asthma and chronic obstructive pulmonary disease (COPD) [112].

Despite some researchers doubting its suitability as a bioaerosol indicator bacterium, substantial evidence validates its application in the present study. The present study utilized *E. coli* K12 type strain and its structure is depicted in Figure 1.4. This specific strain is non-pathogenic and serves as a reliable indicator of bacteria that has been used in several disinfection investigations due to its close similarity to the wild Gram-negative type, as seen in Figure 1.4 The ease of cultivation at the laboratory scale has established it as a vital instrument in relevant studies. However, the reaction may differ considerably among different strains.

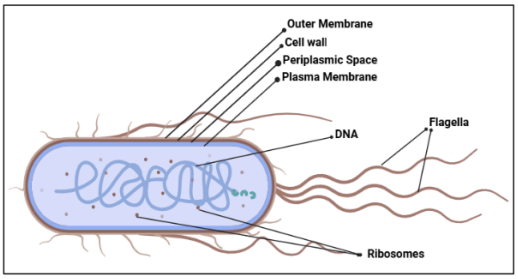

Figure 1.4 Structure of *Escherichia coli (E. coli)*

1.7 Aim of the Study

This research aimed to develop a novel in-situ, visibly-active Fe_2TiO_5 heterostructure composite to neutralize bioaerosols in indoor environments. The study is organized into three distinct development stages, including:

1. The construction of a sustainable cementitious building material utilizing IWPs, i.e., FA, FA, and BS, and assessing its suitability for construction.

2. The synthesis and characterization of the novel Fe_2TiO_5 heterostructure composite material and an investigation of its claimed novelty and antibacterial properties under the visible light spectrum are discussed.

3. Laboratory-scale Photocatalytic disinfection of *E. coli* bioaerosols using Fe_2TiO_5 heterostructure composite, including reactor design, process optimization, boundary condition, and efficiency comparisons.

1.8 Thesis Outline

The first chapter of the thesis includes an informative overview of the concepts of advanced oxidation processes, namely TiO_2-photocatalysis, photocatalytic building materials, and their applications in air purification. The section also examines the implications of sustainable construction methods on preserving natural reservoirs and advancing the circular economy idea.

The second chapter addresses the review of existing literature on analytical and experimental research. This chapter also defines the objective of the current investigation.

The third chapter elaborates on the comprehensive procedure of fabricating sustainable cementitious material and applying a TiO_2 catalyst on its outer surface, forming a Fe_2TiO_5 heterostructure for cementitious composite. This chapter also addresses the experimental program and the procedure for estimating the bioaerosols disinfection process using the Fe_2TiO_5 heterostructure for cementitious composite under the visible light spectrum.

The fourth chapter systematically analyzes the results and interactions of the fundamental parameters that govern the disinfection process of the visibly active Fe_2TiO_5 heterostructure for cementitious composite. The study primarily assessed the structural suitability of the developed iron-rich cementitious material regarding its durability and strength properties. The effectiveness and novelty of the proposed research were subsequently evaluated through detailed microscopic investigations of the Fe_2TiO_5 heterostructure using different techniques. The antibacterial properties of the Fe2TiO5 heterostructure for cementitious composite were also investigated. Then, the application of Fe_2TiO_5 heterostructure composite in the treatment of bioaerosols in indoor environments was analyzed. The kinetic modeling of the visible light-responsive photocatalytic process in the disinfection of bioaerosols was examined for lab-scale analysis.

The fifth chapter presents the conclusions from the analysis conducted in chapter four. Final comments are provided regarding the overall efficacy of this naturally occurring surface-active Fe_2TiO_5 heterojunction layer on disinfecting bioaerosols indoors.

Chapter 2

Literature Review

2.1 Overview

Air pollution represents a critical global challenge with substantial effects on human health and environmental integrity. Although outdoor air pollution has garnered considerable attention, it presents a similarly crucial issue, given that individuals typically spend most of their time indoors [113]. The indoor air quality is adversely affected by the presence of multiple pollutants, such as carbon monoxide (CO), volatile organic compounds (VOCs), particulate matter (PM), and biological contaminants. These pollutants originate from various sources, including smoking, disinfectants, poor ventilation, and the emission of building materials [114]. Poor indoor air quality poses health risks that are frequently more significant than those associated with outdoor air pollution. Also, exposure to indoor air pollutants can lead to a range of adverse health impacts, including migraines, respiratory issues, skin allergies, and even an increased risk of cancer. Children, older people, and individuals with chronic respiratory or cardiovascular conditions are especially susceptible to the detrimental impacts of indoor air pollution [114].

Recent studies have highlighted the global burden of indoor air pollution, with the World Health Organization estimating that it is responsible for the deaths of 3.8 million people annually [12]. Moreover, indoor air pollution and poor urban air quality are recognized as two of the most significant toxic contamination problems globally [115]. Addressing indoor air pollution presents multifaceted challenges. Conventional air purification techniques, including mechanical filtration and chemical sterilization, demonstrate constraints related to microbial resistance, maintenance requirements, and affordability [116]. To overcome these limitations, researchers have explored the application of photocatalytic disinfection technologies and other advanced techniques to enhance the assessment and control of indoor air quality [117].

Incorporating such innovative techniques into cementitious construction surfaces offers a passive and sustainable solution to indoor air treatment, effectively addressing a significant gap in indoor microbial contamination control. However, the relationship between construction materials and environmental air remediation remains unexplored despite the worldwide

attention on sustainable development practices. Initially, the selection of building materials has focused mainly on structural integrity, affordability, and aesthetic value, with insufficient emphasis on their potential for different environmental remediation. Some internationally recognized building rating organizations, including GRIHA (India) and LEED (USA), have integrated ecological sustainability parameters focusing on reducing energy consumption, low carbon footprints, and preservation of resources. However, incorporating active environmental remediation through building materials is inconsistent and erratically implemented worldwide [118]. This gap is particularly pronounced in developing nations like India, where rapid urbanization and infrastructure development are accompanied by the cost of expanding air contamination, occupational hazards, and adverse environmental impacts [115].

Therefore, the building materials must be reevaluated as active participants in ecological remediation, given the significance of the global air pollution crisis, which is of the utmost urgency. Incorporating functionalized building components, including photocatalytic surfaces, self-cleaning coatings, and antimicrobial composites, can substantially enhance indoor and outdoor air quality [119]. Notably, nano-technological materials, such as TiO_2 thin films integrated into cementitious structures, have effectively degraded airborne contaminants and mitigated microbiological contamination in outdoor and indoor environments [120]. Utilizing such cutting-edge construction materials will guarantee that building materials will function not just as passive structures but also play an active role in pollution mitigation, occupant well-being, and occupational safety.

With these considerations in mind, this chapter discusses the integration of industrial waste materials into sustainable construction practices and their influence on the scope of environmental remediation initiatives. The chapter additionally reviews the TiO_2-assisted photocatalytic techniques, their extensive applications in the construction industry, and their related limitations. The current state of photocatalytic construction materials regarding their commercial applications in air control measurements was also examined. Various alternatives have been explored to overcome the disadvantages of the technologies that have been discussed. This review focuses on using green building techniques and an advanced oxidation process for indoor air purification.

2.2 Role of Industrial Waste Materials in Environmental Remediation: A Sustainable Construction Practice

2.2.1 Generation of solid industrial waste materials

The swift expansion of industrialization and urbanization has resulted in a significant rise in solid industrial waste production, presenting considerable environmental and health issues. Industrial waste materials include various materials such as metals, plastics, hazardous chemicals, FA, FS BS, steel slag, mining tailings, and electronic waste (e-waste), each presenting unique environmental challenges [121].

Inappropriate disposal and mismanagement of industrial waste lead to land degradation and water and air pollution, worsening the critical condition of worldwide environmental degradation [122]. Developed countries have implemented regulatory frameworks and waste management techniques; however, many developing nations like India still encounter challenges in establishing efficient waste management and recycling networks, leading to ungoverned dumping and toxic waste accumulation [123].

The sources of solid industrial waste materials are distinctively industry-specific. The construction industry generates enormous amounts of cement debris, concrete, and glass waste, while the mining and metallurgical sectors yield mine tailings, red mud, and slag residuals [124], [125]. These industries considerably contribute to solid industrial waste materials by producing bottom ash, gypsum, and fly ash. Improper management of these materials results in airborne particulate emissions and leachate contamination [126]. Also, the chemical and manufacturing industries discharge various hazardous by-products, such as dye solvents and heavy metals, which contribute to significant toxicity in the surrounding environment [127]. The growing dependency on modern technology has resulted in a notable increase in e-waste, which comprises hazardous materials including lead (Pb), mercury (Hg), cadmium (Cd), and rare earth elements, thereby posing considerable challenges for disposal and recovery [128].

2.2.2 Environmental Impact of solid industrial waste materials

The environmental impacts of solid industrial waste materials are extensive, impacting several ecosystems and human health. One of the significant concerns is soil pollution, which occurs when heavy metals, including As, Cd, Pb, and Hg, are introduced by toxic industrial waste,

affecting microbial biodiversity and soil fertility [129]. Non-biodegradable waste, including plastics and fly ash, modifies soil structure, diminishes permeability, and impacts vegetation growth [130]. Further, industrial waste disposal contributes to water pollution, worsening environmental issues. Effluents containing heavy metals, micro-plastics, and organic pollutants contaminate surface and groundwater sources [131]. The leaching of hazardous compounds from unsupervised landfill sites into aquatic ecosystems interferes with ecological diversity and the food chain, posing significant risks to human health [132]. Also, air pollution represents an important concern related to industrial waste management, especially regarding burning toxic materials and e-waste. This process emits furans, VOCs, dioxins, and fine particulate matter ($PM_{2.5}$, PM_{10}) [133]. These airborne contaminants are associated with cardiovascular diseases, respiratory disorders, and elevated mortality rates, especially in densely populated urban regions with significant industrial activity [134].

2.2.3 Dominance of iron-rich industrial waste material and related environmental impacts

The extensive generation of IWPs, notably FA, FS, and BS, poses a considerable ecological problem owing to their accumulation and inadequate disposal methods. Thermal power plants, metal casting industries, and iron and steel fabrication processes mainly generate these waste materials. The rising generation of these industrial waste products requires sustainable management practices to address various associated environmental concerns [135].

2.2.3.1 Fly ash

Fly ash (FA), a fine particulate byproduct generated during coal combustion in thermal power plants, represents one of the most considerable industrial wastes globally. All over the globe, coal-fired power stations generate more than 750 million tons of FA each year, with a substantial amount left unutilized, resulting in considerable environmental pollution [136]. The high levels of silica (SiO_2), alumina (Al_2O_3), iron oxides (Fe_2O_3), and trace hazardous components in FA deliver a potential risk to air, soil, and water ecosystems. In areas with unregulated FA disposal, like India, China, and South Africa, massive FA ponds have resulted in airborne particulate matter, groundwater leaching, and soil pollution, posing lifelong health hazards [137]. A notable instance occurred in the Korba industrial region of India, where persistent fly ash

accumulation from power plants resulted in increased $PM_{2.5}$ emissions, contributing to respiratory infections among the local populace [138].

2.2.3.2 Foundry sand

Foundry sand (FS), a significant by-product of metal casting industries, primarily consists of SiO_2, Fe_2O_3, and bentonite clay, with a global production rate of 100 million tons annually [103]. The inappropriate disposal of FS in landfills has resulted in soil contamination because of phenols, heavy metals, and organic binders in waste FS [139]. According to research [], FS disposal sites in the US contain substantial concentrations of heavy metals and polycyclic aromatic hydrocarbons (PAHs), which contaminate groundwater [140], [141]. Similarly, in China's industrial sectors, the buildup of FS in open-air disposal sites has resulted in considerable soil degradation, rendering the land unfit for agricultural applications [142]. However, waste valorization innovations have facilitated FS reutilization in concrete production, asphalt mixtures, and geotechnical applications, dramatically reducing landfill utilization and decreasing its ecological impact [143]–[146].

2.2.3.3 Blast Furnace sand

Blast furnace sand (BS) is another IWP generated during the iron and steel manufacturing process, with an annual global output of approximately 400 million tons [147], [148]. BS consists of calcium, silica, magnesium, and iron oxides. Although specific amounts of BS are employed in construction practices, a considerable amount remains abandoned, raising environmental problems. The BS disposal negatively impacts the environment by forming alkaline leachate, which affects nearby reservoirs and modifies the chemical composition of soil [149]. The Raritan Bay Slag Superfund Site in New Jersey exemplifies the use of BS containing heavy metals from NL Industries' lead smelting operations in constructing a seawall along the coastline. The slag containing lead, arsenic, copper, and antimony has leached into the soil and surface water, offering considerable health risks to residents and wildlife [150], [151]. Similarly, unsupervised BS disposal in coastal areas in Japan has resulted in elevated marine contamination, adversely affecting marine biodiversity [152].

2.2.4 Prevailing solution

The growing generation rate of IWPs represents a significant challenge to environmental sustainability, highlighting the need for expanded waste disposal methods, advanced recycling techniques, and robust regulatory frameworks. In response to these critical problems, numerous viable waste management approaches have been investigated, highlighting principles of the circular economy, material recycling, and technological innovations in solid waste treatment. The implementation of industrial symbiosis, which involves repurposing waste products from one industry as raw materials for another, has demonstrated potential in reducing solid industrial waste generation and enhancing resource efficacy [153], [154]. Furthermore, using industrial waste products like FA, BS, steel slag, and red mud in building materials, geopolymers, and soil-stabilizing methods has proven to be an effective strategy for decreasing landfill dependency while improving material properties and environmental impacts [155]–[157].

Sweden exemplifies a global standard for sustainable industrial waste management, with more than 99% of garbage being reused or repurposed via recycling and energy recovery technologies [158], [159]. The nation's waste-to-energy (WTE) initiatives transform municipal and industrial waste into electrical power and district heating energy, considerably diminishing reliance on landfills [159]. This achievement illustrates that efficient policy execution, technical advancement, and industry-derived initiatives may facilitate substantial waste reduction and promote environmental sustainability. Nonetheless, worldwide inequalities in industrial waste management continue to exist, necessitating enhanced regulatory frameworks, international collaboration, and the extensive implementation of sustainable strategies.

2.2.5 Utilization of Iron-Industrial Waste Materials for Sustainable Construction Practices

The construction industry, a major consumer of natural raw materials/ reservoirs, offers a viable prospect for integrating industrial waste products into building materials. Incorporating FA, BS, and FS in concrete, cementitious, or road-based materials has garnered considerable interest because of its capacity to improve mechanical and durability characteristics and, thus, reduce environmental consequences [160]–[164]. Comprehensive studies have been undertaken to evaluate the influence of different ratios of these IWPs on the strength and durability of construction materials.

2.2.5.1 Fly Ash as a Sustainable Cementitious Material

FA, a by-product of coal combustion in thermal power plants is a pozzolanic substance extensively utilized as a supplementary cementitious material (SCM) in cement mortar and concrete. The inclusion of FA in cement has been thoroughly studied, indicating substantial enhancements in workability, durability, and strength characteristics [165]–[167]. Studies suggest that substituting 5-30% of cement with FA improves the compressive and flexural strength of concrete/cement mortar over time, attributable to the pozzolanic reaction that generates secondary hydration products. Increasing FA replacement levels (more than 40%) results in early-age strength reduction due to the slow pozzolanic reaction; however, long-term strength and durability, comprising sulfate and chloride penetration resistance, increases notably [165], [168]–[174]. Table 2.1 summarizes the impact of FA on various mechanical characteristics as documented by multiple researchers. It presents the optimal range of FA substitution employed to attain superior mechanical properties of the building material within the specified curing time.

Multiple studies [175]–[178] have discovered that FA-based high-performance concrete (HPC) with a 10-50% replacement level demonstrated lesser permeability and improved resistance to harsh environments, rendering it appropriate for marine and sulfate-rich circumstances. Furthermore, FA has been effectively integrated into geopolymer concrete, where it interacts with an alkaline activator to create a polymeric gel structure, improving its mechanical properties and diminishing CO_2 emissions linked to conventional cement manufacturing [179]–[182].

Table 2.1 The impact of FA on different mechanical characteristics and durability parameters is documented by various researchers.

FA substitution range (%)	W/C	Curing period (days)	Optimum compressive strength dosage (%)	Optimum Split tensile strength dosage (%)	Optimum Flexural strength dosage (%)	Ref.
0-20 (varied by 5%)	--	28,60,90	10	--	--	[183]
0-10 (varied by 5%)	0.65	28,100,130	5	--	--	[184]
0-20 (varied by 10%)	0.34	7,28	10	10	10	[185]
0-50 (varied by 10%)	--	7,14,21,28	10	10	--	[186]
0-45 (varied by 15%)	0.55	3,7,14,28	30	30	--	[187]
0-30 (varied by 10%)	0.45	7,28	30	--	--	[188]
0-30 (varied by 10%)	0.45	3,7,28	10	10	10	[189]
0-70 (varied by 20%)	0.30	28,56	30	30	--	[190]
0-15 (varied by 5%)	0.50	7,28,56,90	5	5	--	[191]
0-25 (varied by 5%)	0.50	7,28,90,180	10	10	--	[192]

2.2.5.2 Blast Furnace Sand as a Sustainable Cementitious Material

BS, a by-product of the iron and steel manufacturing sector, has been widely employed as a substitute for cement and fine aggregate materials. BS can substitute 20-50% of Portland cement in cement applications, significantly diminishing CO_2 emissions and improving mechanical characteristics [193]–[198]. Also, research studies indicate that incorporating BS into concrete enhances long-term strength development, sulfate resistance, and durability by forming a compact matrix and reducing permeability [199]–[202].

Various researchers [203], [204] have indicated that substituting 0-50% of cement with BS increases the resistance to alkali-silica reaction (ASR) and freeze-thaw cycles. Furthermore, BS-modified concrete demonstrates improved resistance to chloride ingress, rendering it an optimal material for architecture subjected to marine settings [205]. Mostazid et al. (2022) [206] showed that the BS inclusion diminishes the heat of hydration, hence reducing thermal cracking within massive concrete buildings. Also, the application of BS as a fine aggregate has demonstrated its potential to enhance the mechanical characteristics of self-compacting concrete (SCC) and increase its sustainability profile [207]–[209]. Table 2.2 summarizes the impact of BS on the mechanical characteristics of building materials as documented by multiple researchers. It presents the optimal range of BS substitution employed to attain superior compressive strength properties of the building material within the specified curing time.

Table 2.2 The influence of BS on the compressive strength of construction materials as documented by various studies.

BS substitution range (%)	Optimum compressive strength dosage (%)	Ref.
0-30 (varied by 15%)	15	[210]
0-100 (varied by 25%)	50	[211]
0-60 (varied by 20%)	40	[212]
0-60 (varied by 20%)	60	[213]
0-50 (varied by 25%)	50	[214]
0-30 (varied by 20%)	40	[215]
0-60 (varied by 15%)	45	[216]
0-60 (varied by 10%)	50	[217]
0-75 (varied by 25%)	25	[218]

Cement + Waste glass powder + BS: 50 + 40-30 + 10-30	50+10+40	[219]
FA + BS: 0-100 (varied by 20%) + 0-40 (varied by 10%)	60+40	[220]

2.2.5.3 Foundry Sand as a Sustainable fine aggregate Material

FS, produced by metal casting industries, possesses a high silica concentration and can serve as an excellent partial substitute for fine aggregates in cement mortar/concrete materials. Studies indicate that substituting 10-30% of natural sand with FS enhances compressive and flexural strength owing to its superior packing capability and enhanced interfacial transition zone [221]–[224]. However, at excessive replacement levels (beyond 40%), workability diminishes because of elevated water requirements [225]–[227].

Several studies [103], [227], [228] have demonstrated that the inclusion of 20% FS in concrete enhanced its resistance to abrasion and sulfate attack, rendering it suitable for pavement applications. Furthermore, research conducted by [229], [230] demonstrated that incorporating FS in masonry blocks improves thermal insulation qualities, facilitating energy-efficient architectural designs. The application of chemically stabilized FS in geotechnical environments, including embankments and sub-base layers, has been investigated, yielding favorable results regarding load-bearing capability and long-term durability [231], [232]. Table 2.3 summarizes the impact of FS as fine aggregate substituent on the mechanical characteristics of building materials, as documented by multiple researchers. It presents the optimal range of FS substitution employed to attain superior compressive strength properties of the building material within the specified curing time.

Table 2.3 Studies on WFS as a partial substitute for fine aggregate in building materials.

FS substitution range (%)	Optimum compressive strength dosage (%)	Ref.
0-25 (varied by 5%)	25	[233]
0-30 (varied by 10%)	30	[234]
0-30 (varied by 10%)	30	[235]
0-30 (varied by 10%)	20	[236]

0-50 (varied by 10%)	40	[237]
0-50 (varied by 10%)	30	[238]
0-30 (varied by 10%)	30	[239]
0-40 (varied by 10%)	20	[240]
0-40 (varied by 10%)	10	[241]
0-25 (varied by 5%)	20	[242]
0-50 (varied by 10%)	20	[243]

2.2.5.4 Summary and Future Prospects

Incorporating FA, BS, and FS into building materials has numerous advantages, such as improved mechanical properties, durability, and a sustainable environment. However, the efficacy of these IWPs depends upon their respective replacement levels, particle size distribution, chemical configuration, and curing environment. Table 1 outlines the impact of varying IWP replacement percentages on compressive strength and durability characteristics, as reported in multiple studies.

The growing focus on green building technologies highlights the potential of utilizing FA, BS, and FS to mitigate the construction industry's carbon footprint and tackle the issues associated with industrial waste disposal. Thus, incorporating these materials into construction practices is consistent with circular economy principles, enhancing resource efficacy and fostering urban sustainability.

2.3 Photocatalytic Construction Materials with Antimicrobial Properties for Indoor Air Treatment

2.3.1 General

Airborne biological contaminants, such as bacteria, fungal spores, and viruses, significantly compromise indoor air quality (IAQ) and pose risks to human health. Bioaerosols in enclosed environments, including healthcare facilities, workplaces, and residential buildings, are associated with respiratory problems and allergic reactions [244]. TiO_2-based photocatalysis has drawn much interest in air purification techniques because it can deactivate airborne microbes by generating reactive oxygen species (ROS) when exposed to UV radiation [245]. Recent studies have investigated TiO_2-integrated construction materials, including photocatalytic concrete, tiles,

and paints, for their efficacy in reducing indoor microbial contaminants. This review examines the antibacterial mechanisms of TiO_2, recent developments in TiO_2-modified building materials, and their effectiveness in controlling indoor biological pollutants.

2.3.2 TiO_2 as a potential antimicrobial photocatalyst for air purification

TiO_2 has received considerable interest in recent decades owing to its photocatalytic and antimicrobial characteristics, rendering it a viable material for air purification and environmental remediation. A ROS production process, TiO_2 photocatalysis results in the degradation of organic contaminants, inactivation of microorganisms, and elimination of airborne pollutants under UV irradiations [246]. The distinctive physicochemical characteristics of TiO_2, such as its exceptional stability, robust oxidative capacity, and self-cleaning qualities, have facilitated its extensive application in indoor and outdoor air purification [247]. Comprehensive studies have shown the efficacy of TiO_2-based nanomaterials in mitigating air pollution and microbiological contamination and enhancing air quality across diverse environments.

Titanium dioxide (TiO_2) occurs in three principal polymorphs: anatase, rutile, and brookite. Most research suggests that the photoactivity of TiO_2 anatase is significantly more effective than that of TiO_2 rutile; the differences are likely due to the rate of (e^-/h^+) recombination in the two forms [248]. However, it has been discovered that mixtures of TiO_2 anatase and TiO_2 rutile are significantly more effective in eliminating pollutants and inactivating coliphage MS2 [249]. Degussa P25 is a commercially viable and active form of TiO_2, consisting of approximately 80% anatase and 20% rutile [248]. The improved photo-activity is usually ascribed to interactions between the two forms, reducing bulk (e^-/h^+) recombination. Brookite has been the subject of minimal research; nevertheless, a recent study indicated that a combination of TiO_2 brookite and TiO_2 anatase was significantly more efficient than anatase alone [250].

TiO_2 demonstrates significant antimicrobial efficacy, resulting from ROS-induced degradation of microbiological cell walls, protein molecules, and genetic material [251]. Research indicates that TiO_2-modified air purification systems can efficiently inactivate airborne *Staphylococcus aureus*, Influenza virus, and *Escherichia coli*, thereby inhibiting the transmission of infectious diseases [252]. A research investigation by [253] demonstrated that TiO_2-based antibacterial coatings attained over 99.9% bacterial inactivation within 30 min of contact, indicating potential applicability for the medical and food manufacturing industries. Numerous studies demonstrate

the remarkable antibacterial efficacy of TiO_2 nanoparticles when subjected to UV light irradiation [254]–[257].

Mathew et al. (2023) [258] investigated advanced TiO_2 photocatalysts, examining the synergistic effects of TiO_2 with silver (Ag), copper (Cu), and graphene-based nanoparticles to improve antibacterial activity under the visible light spectrum. Their findings demonstrated that Ag-doped TiO_2 composites show 3.5 times superior antimicrobial activity against multidrug-resistant bacteria compared to simple TiO_2. Similarly, Jia et al. (2021) [259] examined the antiviral capabilities of TiO_2. They revealed that a TiO_2-graphene hybrid composition might inactivate SARS-CoV-2 within 15 min of exposure to UV light, providing an innovative approach for air decontamination in healthcare facilities and outdoor areas. A summary of some research papers examining the application of advanced TiO_2 photocatalysts for bacterial inactivation is presented in Table 2.4.

However, even though all of the above-mentioned reported research studies successfully achieved a satisfactory degree of disinfection efficiency, they all have some drawbacks that fall into one or more categories, restricting their potential for field-scale applications. The following are some of the shortcomings that have been reported: 1) The utilization of artificial ultraviolet (UV) lamps; 2) the separation of catalysts; 3) the high cost of the photocatalyst fabrication process; and 4) difficulties in scaling up operations.

2.3.3 Antibacterial Mechanism

TiO_2 nanoparticles have been widely utilized as photocatalysts for photo-decomposing organic compounds in wastewater treatment. In recent decades, it has also been used as a photocatalyst for disinfecting bacteria and other microorganisms, highlighting its potential applications in disinfection of diverse surfaces and air and water treatment [260], [261]. TiO_2 has been investigated for its disinfection efficacy against various microorganisms, including diverse Gram-negative and Gram-positive bacteria, fungi, and algae [261]. The mechanism of TiO_2 photocatalytic disinfection remains unclear, and considerable dispute persists over the precise mode of action. However, the killing mechanism is the most widely accepted route of antimicrobial activity, wherein the breakdown of the cell wall or membrane primarily occurs because of the interactions of photo-induced ROS on the TiO_2 surface.

Table 2.4 List of selected research papers on applying advanced TiO_2 photocatalysts for inactivation of bacteria.

Pollutant	Reactor	Catalyst	Exposure Condition	Performance	Reference
E. coli	Petri dishes	TiO_2 & Ag-doped TiO_2	UV light	TiO_2: *E. coli* reduction of 1.6 log observed at the end of 180 min. Ag-doped TiO_2: *E. coli* reduction of 99.99% at the end of 90 min.	[262]
P. aeruginosa *E. coli* *S. aureus*	LB agar plates	Ag-doped TiO_2, s.t., TiO_2 calcinated at 300°C & TiO_2 calcined at 500°C and 300°C without Ag	UV light	TiO_2 (calcined 300°C)-Ag: reduction in bacteria growth by 95%. TiO_2 (calcined 500°C) without Ag reduces bacterial growth by 30%. TiO_2 (calcined at 300°C) without Ag reduces bacterial growth by 75%.	[263]
E. coli	Batch reactor	CuO_2- doped TiO_2	Under visible light irradiation (380–720) nm.	Bacterial inactivation efficiency of 98% at the end of 60 min and a 99.7% VOC removal efficiency within 25 min	[264]
P. aeruginosa	Glass fiber tissue	Poroux TiO_2 , TiO_2-PEG and Ag-doped TiO_2	UV light	Ag-doped TiO_2: 100% bacteria inactivation rate after 10 min TiO_2 porous: 57% bacteria inactivation rate after 10 min TiO_2-PEG: 93% bacteria inactivation rate after 10 min	[265]
E. coli K12	Agar matrix surface + blueberry skin + calyx	TiO_2- NP	UV	UV alone: 4.5 log CFU/g and UV-TiO_2: 5.3 log CFU/g in 30 s.	[266]
E. coli	Planar reactor	TiO_2, Ag-doped TiO_2 and Cu-doped TiO_2 deposed on optical fibers	UVA-LEDs (365 nm, UVA-LED intensity = 1.5 W/m^2).	TiO_2/Ag & TiO_2/Cu: bacterial reduction of 3 log.	[267]

The hydroxyl radical ions (•OH) formed on the surface of the TiO_2 generally connect to the bacterial cell wall, resulting in cell wall damage through rapid potassium ion leakage. Various factors influence the generation of radical ions that improve bactericidal photo-activity. The •OH is anticipated to contribute considerably to the sterilization mechanism; however, its precise role is unclear because of its brief half-life. Conversely, peroxide (H_2O_2) radicals exhibit an extended half-life and may possess greater potency than other radicals owing to their negative charge. These radicals significantly impact the cell wall by breaking down the phospholipid membrane. Subsequent to the breakdown of the internal Coenzyme A, the primary disinfection targets for gram-negative and gram-positive bacteria may differ based on their peptidoglycan composition. Moreover, gram-positive bacteria are devoid of an outer membrane. Hence, the sterilization technique is different for these two separate bacterial species. However, both types of bacteria demonstrate rapid ion leakage, nucleic acid destruction, and lipid peroxidation. This aligns with the behavior of all other living organisms, including plants [268]–[270].

2.3.4 Photocatalytic construction material for different indoor applications

Titanium dioxide (TiO_2) stands out as the most prevalent photocatalyst in photocatalytic construction and building materials. This semiconductor compound has been utilized as a white pigment in paints, cosmetics, and food products since ancient times [271]. The widespread application of TiO_2 in photocatalytic construction materials can be linked to several key features: (a) cost-effective, secure, and chemically stable; (b) exhibits superior photocatalytic activity in comparison to other semiconductor metal oxide ; (c) integrates well with conventional building materials like cement, maintaining its original functionality; (d) functions effectively under low solar irradiation in typical environmental conditions. The integration of photocatalysts with construction materials began in the early 1990s. The multifunctional nature of TiO_2, capable of acting as both photocatalytic and structural components, has enabled its use in various applications, including exterior building materials and interior furnishings like cement mortar, paving blocks, PVC fabric, glass, and exterior tiles. Table 2.5 presents the classification of significant TiO_2-based construction and building materials.

Table 2.5 The categorization of notable TiO_2-based construction and building products.

Classifications	Photocatalytic Product	Property
Outdoor building materials	Tiles, glass, tarpaulins, plastic sheeting, panels	Self-cleaning and Air purification
Indoor furnishing materials	Tiles, wallpaper, curtains, blinds, paints, sealing coatings	Self-cleaning and antibacterial
Road construction materials	Soundproof walls, tunnel walls, roadblocks, concrete pavements	Self-cleaning and air purification

Photocatalytic paints, integrated with various binders, including lime, silica sol-gel, organic binders, and polyorganic siloxane, are the most commonly utilized building elements for removing indoor airborne contaminants. Maggos et al. [272] evaluated the depolluting performance of TiO_2-infused paint in an indoor car park using a real-scale setup. The ceiling of the car park was coated with a white acrylic paint containing TiO_2. The designated closed section of the parking lot experienced contamination from vehicle emissions throughout the testing phase. Upon achieving a steady state, the UV lamps were activated for five h. The results indicated a significant photocatalytic oxidation of NO_x gases. The photocatalytic removal efficiencies for NO and NO_2 were 19% and 20%, respectively. Likewise, Guarino et al. [273] selected two identical mechanically ventilated farrowing rooms on a swine farm, where NH_3 was the primary pollutant, to investigate the pollutant removal efficacy of a TiO_2 catalytic paint. Factors like environmental parameters, air circulation rates, and concentrations of gases were continuously monitored in both the catalytic painted room and a reference room. An average NH_3 concentration of 5.41 mg/m^3 was recorded in the reference room without treatment, while the concentration in the experimental room was 3.76 mg/m^3 during a complete farrowing cycle.

In addition, building materials like composite sheets and wallpapers are also modified with photocatalysts to mitigate indoor pollution. Ichiura et al. [274] developed a composite TiO_2–zeolite sheet through papermaking. The pollutant removal efficiency was evaluated using toluene and formaldehyde as target indoor contaminants under UV irradiation. The composite sheet with a Ti/zeolite ratio of 1:4 demonstrated the highest efficacy in toluene removal; however, an optimal composition for formaldehyde was not identified, attributed to the high formaldehyde absorptivity of Y-type zeolite. The study demonstrated that these sheets have the potential to be

applied to walls and ceilings of an indoor room for the removal of multiple indoor contaminants. Taoda et al. [275] designed photocatalytic wallpaper by using a visible light active photocatalyst on the surface. The experimental results demonstrated that toluene and acetaldehyde can be efficiently decomposed under fluorescent lamp irradiation, although UV irradiation yielded superior performance. TiO_2-infused construction materials can also eliminate odors in indoor environments when additional UV sources are not helpful. The odor is detectable by human noses and results from chemical substances present at concentrations of approximately 10 parts per million by volume. A weak UV intensity of 1 mW/cm^2 is enough to decompose these chemicals in the presence of TiO_2 photocatalyst [276]. Table 2.6 provides an array of research publications addressing the incorporation of TiO_2-based nanoparticles as indoor air-decontaminating agents in building materials.

Table 2.6 Overview of TiO_2-based nanoparticles imposing air purification characteristics on building surfaces.

Catalyst	Construction material	Pollutant	Exposure condition	Efficiency attained	Ref.
1 wt.% TiO_2	Cement mixed with recycled glass and/or sand (base)	NO (400 ppb)	UV light	NO removal: 4 mg/(m^2.h)	[277]
1 wt.% TiO_2	Cement mortar (panels located in street canyon)	NO_x	UV light	36.7–82.0% NO removal rate	[278]
3, 5, and 10 wt.% TiO_2	Cement mortar	NO	UV light	36.9% NO removal rate	[279]
5 wt% and 10% TiO_2	Cement paste	NO (1000 ppb)	Solar light	5 wt% TiO_2: NO removal: 170 µmol/(m^2·h), 10 wt% P25: 170 µmol/(m$_2$.h)	[280]
TiO_2	Ceramic roofing tiles	Toluene (17–35 ppb)	UV light	removal rate up to 512 µg/(m$_2$·h);	[281]
(1–10 wt%) TiO_2	Cement mortar	Formaldehyde (20 ppm)	UV light	formaldehyde: removal rate 0–65%	[282]
2 wt.% TiO_2	Building coatings: wall	NO_x (400 ppb)	UV light	Conversion varied from 80% for the 50-day	[283]

	paint and plaster			sample to 30% for the 1-year-old sample.	
5 and 10 wt % TiO_2	Cement mortar	SO_2 (14 ppm)	Simulated sunlight – SO_2	40% removal efficiency at the end of 90 min	[284]
Surfactant-modified TiO_2 (P25)	Portland cement paste	NO (1 ppm)	Visible light	conversion photonic efficiency: 15%	[285]
Mn–TiO_2	Cement coating applied on gypsum, plywood, and glass panels	NO (250 μg/m^3)	UV and visible light	UV: 90% removal rate for gypsum, near 100% removal rate for plywood and glass at the end of 45 min; Visible –40% removal rate for gypsum, plywood, and glass at the end of 45 min.	[286]
Au–TiO_2/SiO_2	Limestone, granite	NO (20 ppm)	UV and visible light	limestone: with Au NPs: NO removal rate: 63%, granite: with Au NPs : NO removal rate: 79% and limestone: without Au NPs: NO removal rate: 33%, granite: with Au NPs:NO removal rate:42	[287]
Au/N–TiO_2/SiO_2	Limestone, granite, concrete	NO (1000 ppb)	UV and visible light	NO removal: 344 μmol/(m^2h). Efficiency was twice that of TiO_2.	[288]

2.3.5 Advancement to photocatalytic construction material as antimicrobial coating

Numerous modifications have expanded the ability of TiO_2 nanoparticles to the visible light spectrum for real and valuable applications in indoor and outdoor environments, including healthcare facilities. TiO_2 nanomaterial-based coatings offer an efficient antibacterial surface for medical instruments, hence diminishing the risk of hospital-acquired infections (HAIs), and have been investigated for use in sterilizing medical equipment and hospital surfaces [289]–[291]. Reid et al. (2018) [292] highlighted the impact of TiO_2 photocatalytic antibacterial coating close to patients at high-contact locations within hospital wards. The study revealed that TiO_2-coated surfaces exhibited a reduced microbial load compared to uncoated areas, concluding that photocatalytic TiO_2 coatings can diminish microbial burden on high-risk surfaces within healthcare facilities.

As discussed before, the antibacterial efficiency of TiO_2 is enhanced when doped with other potent antimicrobial agents such as Cu, Fe, Au, and Ag [261], [268], [293]–[296]. For instance, Leyland et al. [297] revealed that visible light-active doped-TiO_2 photocatalytic and antimicrobial coatings could effectively address hospital-acquired infections (HAIs) in visible light and dark conditions. The researchers investigated F-doped and F/Cu-co-doped TiO_2 for antibacterial efficacy under dark and visible light conditions. The TiO_2 co-doped with Cu demonstrated notably enhanced antibacterial activity compared to doping with F alone, in both visible light and dark conditions, due to the established sensitivity of Cu to microorganisms in the absence of light. The codoped-TiO_2 demonstrated increased antimicrobial performance when exposed to visible light compared to dark conditions, highlighting the contribution of Cu in boosting photocatalytic-induced antimicrobial properties. The findings indicate that Cu can enhance the production of ROS for photocatalytic processes. The codoped-TiO_2 coating demonstrated activity under visible light and in the dark, engaging both photocatalytic processes and a metal ion release mechanism [297]. Similarly, Ag-doped TiO_2 photocatalytic coating has been studied for its antimicrobial properties, demonstrating adequate bacterial disinfection capacity under visible light and dark conditions. This efficacy is attributed to Ag's surface-plasma characteristics and Ag ions' anti-microbial action, respectively [294], [298]. Weng et al. [299] synthesized the Ag-doped TiO_2 photocatalytic coating with an increased surface area, demonstrating superior antibacterial abilities against microbes and MC3T3-E1 cells. This photocatalytic system was proposed to exhibit effective antibacterial properties even without light.

Similarly, due to the surface plasmon characteristics of Au nanoparticles deposited on the TiO_2 surface, Li et al. (2014) [295] suggested that Au–TiO_2 photocatalytic systems would effectively inactivate bacteria like *E. coli* in the dark. In addition to having superior antimicrobial efficacy against microbes, these metal-doped TiO_2 photocatalytic composite-based nano-coatings also exhibit encouraging self-cleaning and recyclable properties both in the presence of light (UV and visible) and in the absence of light [298], [300], [301].

Wasa et al. [302] recently proposed the usage of TiO_2 nanostructured materials as a coating for door handles and comparable surfaces to diminish the growth and expansion of microorganisms, thereby preventing their spread. The study examined the antimicrobial and antibiofilm properties

of TiO_2 nanostructured anatase, rutile, and carbon (NsARC) coatings on *P. aeruginosa, S. cerevisiae, E. coli, and S. aureus* microorganisms. The results were compared with antimicrobial activity on other surfaces, like stainless steel and copper, under different circumstances, namely UV, visible, solar, and no-light conditions. The nanostructured TiO_2 coating on the NsARC surface demonstrated superior performance, exhibiting the lowest microbial survival rates compared to other uncoated surfaces across all examined conditions. The nanostructure TiO_2 coating (NsARC) demonstrated significant antimicrobial and antibiofilm properties, even without light. This photo-inactivation was linked to the antibacterial property of the carbon element present in the NsARC. Reports indicate that carbon functions as an antimicrobial and an effective antiviral agent in the fight against SARS-CoV-2, suggesting it could be an ideal candidate when combined with TiO_2-based nanostructures [302], [303]. New studies indicate that antibacterial nano-coatings exhibiting notable antiviral properties may effectively address viral infections, including the SARS-CoV-2 virus [303]–[308].

2.3.6 Application status and key influencing factors of photocatalytic building materials

Following positive outcomes from laboratory-scale studies, photocatalytic construction materials have been used in real-world applications, such as commercial buildings, galleries, and transportation facilities. Table 2.7 enumerates several examples of projects utilizing photocatalytic construction materials. These materials have been used in several nations, including China, Berlin, and the Netherlands, demonstrating durability and efficiency through extensive testing on the ground. For example, the Toledo Specialist Hospital in Mexico City has utilized TiO_2-coated tiles manufactured by Elegant Decoration, a Berlin-based construction firm. The photocatalytic façade demonstrated efficacy in reducing contaminant levels in the ambient air, as validated by extensive field trials.

Table 2.7 The practical utilization of TiO_2 in a building's façade or roofing system.

Project Name	Construction Material	Location	Advantages	Limitation	Ref.
Palazzo Italia	Facade coated with TiO_2	Milan, Italy	Enhances air quality, mitigates carbon emissions, features an energy-efficient design, and utilizes renewable energy sources.	Installation and Maintenance expenses. Restricted efficiency in	[309]

Palazzo Lombardia	Facade coated with TiO_2	Milan, Italy	Consumption is mitigated by absorbing sunlight and decreases the demand for air conditioning.	areas with high contamination levels	[310]
Edificio Malecon	Facade coated with TiO_2	Mexico City, Mexico	air purity, self-cleaning attributes, lower energy consumption		[310]
Lafarge Holcim Headquarters	Facade coated with TiO_2	Switzerland	Mitigates air contaminants, possesses self-cleaning attributes and enhances energy efficiency.		[311]
Bullitt Center	Roof coated with TiO_2	Seattle, USA	Air purification diminishes air contamination by decomposing detrimental contaminants.		[312]
Jubilee Church	Facade coated with TiO_2	Rome, Italy	Mitigates airborne pollutants and enhances air quality by decomposing toxic contaminants.		[313]
Nanjing Green Lighthouse	Facade coated with TiO_2	Nanjing, China	Enhances air purity, lowers energy usage, elevates air quality, possesses self-cleaning attributes		[314]
Haze-Free Tower	Facade coated with TiO_2	Beijing, China	Mitigates air pollution, promotes air quality, improves aesthetics, possesses self-cleaning properties		[310]
Denby Dale Passivhaus	Facade coated with TiO_2	Yorkshire, UK	Enhances air quality, mitigates air pollution, and decreases energy consumption for heating and cooling.		[315]
Queen's Building	Facade coated with TiO_2	Bristol, UK	Enhances air quality, diminishes air contamination, possesses self-cleaning attributes		[316]

Likewise, the Jubilee Church in Rome, Italy, has been painted with a TiO_2 coating on its façade. It effectively decomposes detrimental contaminants such as VOCs, SOx, and NOx into nontoxic

compounds while preserving the church's white aesthetic and inhibiting vegetation growth. A section of the northern toll station of the Nanjing Yangtze River Bridge in China, covering roughly 6000 m^2 and in highly polluted regions, utilized doped nano-TiO_2 photocatalytic material. Researchers assessed pollutant concentrations in buildings over several months and concluded that the removal efficiency of NOx surpassed 80%.

2.3.7 Limitations and recommendations

Although the above-mentioned demonstration studies (Table 2.7) have shown promising treatment results, some significant problems still need to be resolved before using photocatalytic construction materials in real-world applications. The primary concern pertains to the stability of the building's photocatalytic functionality. The structural integrity of photocatalytic construction materials is inadequate, resulting in their deactivation. Furthermore, during the decomposition of air contaminants, a considerable quantity of intermediate products, including VOC by-products and airborne particulates, accumulates on the surfaces of photocatalytic construction materials, leading to catalyst contamination and adversely affecting the building's photocatalytic efficacy. Moreover, the impacts and assessment of intermediate by-products have been minimally reported. The ecological consequences of the intermediate by-products generated during contaminant degradation in photocatalytic structures are still unclear, necessitating additional research to enhance understanding of the environmental impacts of photocatalytic buildings.

To ensure that the photocatalytic construction can function reliably and effectively, their execution procedure must consider several factors, including the catalyst, the installation environment, and the building structure. Consequently, choosing photocatalytic construction components derived from catalysts exhibiting high activity and durability is essential. Optimizing their structures and morphologies is crucial for enhancing these photocatalytic materials' degradation efficacy and stability. Exploring multifunctional catalysts, like TiO_2 nano-composites combined with other catalysts, is recommended to improve catalytic efficiency and selectivity to prevent the buildup of intermediates by-products. Secondly, installing photocatalytic structures in an appropriate environment is essential for installation location efficiency, light absorption, and air exposure. The installation location within the building, like vents and walls, can significantly influence the efficacy of photocatalytic materials. Also, the catalyst's reaction rate and activating light intensity must be considered when installing

photocatalytic construction materials to ensure that the optimum degradation of the pollutant is achieved under specified conditions.

Ultimately, photocatalytic construction materials must be compatible with the building's structure to ensure effective utilization. The characteristics of photocatalytic construction materials, including light absorption, mechanical strength, and durability, must be considered throughout the architectural design phase. The building's paint and façade materials must be harmonized with the photocatalytic materials to guarantee the contaminant degradation and their aesthetic value.

2.4 Lacunae

10

Based on the literature review, the following gaps have been identified:

1. The idea of obtaining naturally occurring iron from industrial waste materials to serve as a catalyst for the outer-coated TiO_2 photocatalyst in the production of visibly active Fe_2TiO_5 heterostructure material has not been extensively investigated in the literature.
2. The innovative idea of inherent heterojunction formation utilizing catalysts, specifically Fe_2O_3 and TiO_2, in sustainable cementitious composites to treat indoor biological contaminants remains unexamined to date.
3. No literature has documented the application of Fe_2TiO_5 heterostructure on cementitious composites for indoor microbial disinfection treatment applications.
4. The stability of catalysts and the integrity of films in sustainable building materials for indoor air treatment require investigation.
5. The study seeks to implement the circular economy principle in processing industrial waste materials to conserve natural resources, minimize the environmental impact of metal casting waste, achieve a zero-waste objective, and investigate the novel formation of inherent heterojunctions. Thus, the study examines multiple ecological issues within a single antimicrobial framework.

6. The literature has underexplored the design and manufacturing of a sustainable, real-time building material that is economical and efficient in reducing microbial load in indoor urban environments.

2.5 Objective of the Study

Keeping the mentioned lacunae in view, the present study aims at achieving the following objectives:

1. Preparation of sustainable construction material(s) by incorporating industrial by-products and to investigate its hardened properties.

2. Study the synergistic effect of industrial waste product as a natural dopant with selected immobilized photocatalyst(s).

3. Process optimization and the photocatalytic efficiency comparison of prepared composite in the treatment of bio-aerosols.

Chapter 3

Material and Methods

I. General

This chapter is divided into three sections: A, B, and C. Each section is structured to align with specific objectives, reflecting distinct aims. Section A discusses the formulation and preparation of cement-based mortars and the evaluation of their strength and durability through various testing methods. Section B evaluates the novelty and fabrication of the proposed Fe_2TiO_5 heterostructure for cementitious composite, which went through comprehensive microscopic and antibacterial property check assessments. Section C evaluated the antimicrobial efficiency of the Fe_2TiO_5 heterostructure in neutralizing bioaerosols under visible light irradiation via a series of disinfection experiments. Figure 3.1 depicts the organization of each section along with the proposed workflow.

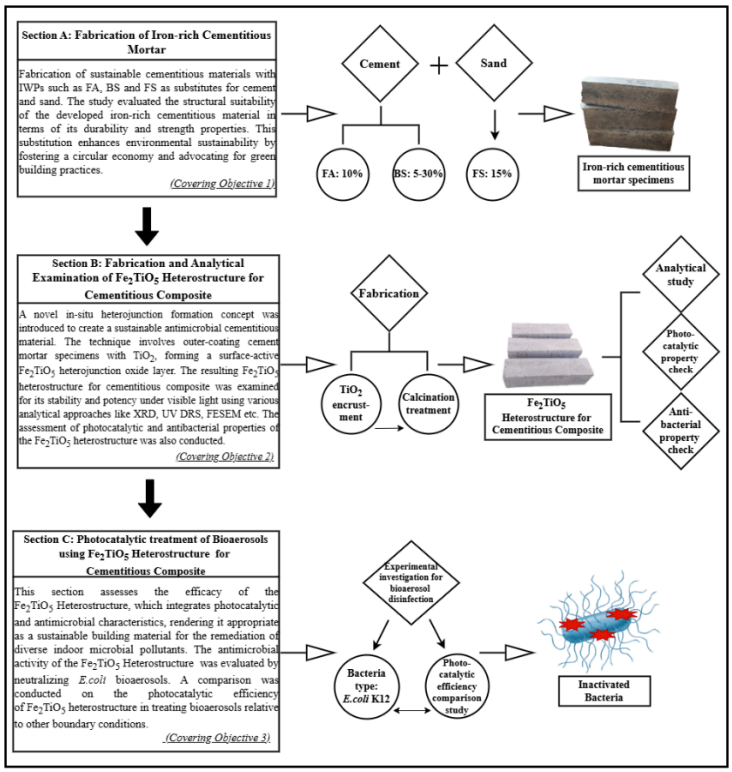

Figure 3.1 Chapter workflow followed by brief descriptions of each section

3.1 Section A: Fabrication of Iron-Rich Cementitious Mortar

3.1.1 Materials

3.1.1.1 Cement

The ordinary Portland cement (OPC) of grade 43, in accordance with IS 8112 [317] produced by Ultra Tech, was utilized to prepare iron-rich cementitious mortar. The cement's chemical composition and physical properties are detailed in Table 3.1 and 3.2, respectively. The field emission scanning electron microscopy (FESEM) analysis was conducted to examine the morphological properties of cement, as shown in Figure 3.2.

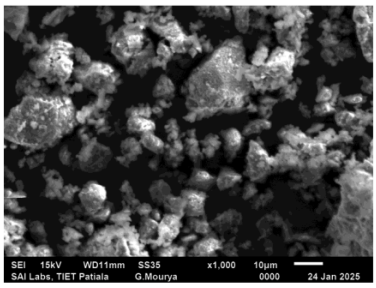

Figure 3.2 The FESEM impression of OPC grade 43

Table 3.1 Chemical composition of OPC grade 43 (using EDS)

Element Oxides		OPC 43 (%)
Calcium Oxide	CaO	63.24
Silica Oxide	SiO_2	21.07
Aluminum oxide	Al_2O_3	5.65
Iron oxide	Fe_2O_3	4.05
Magnesium oxide	MgO	1.16
Sodium oxide	Na_2O	0.20
Potassium oxide	K_2O	0.45

Table 3.2 Physical properties of OPC grade 43

Property	Test results	Standard results as per IS 8112:2013
Specific Gravity	3.10	---
Normal Consistency (%)	26	---
Fineness (m^2/kg)	270	$\geq$ 225
Settling time (min)		
Initial	30	$\geq$ 30
Final	230	$\leq$ 600
Compressive strength (MPa)		
3 days	23.3	$\geq$ 23
7 days	34.65	$\geq$ 33
28 days	47	$\geq$ 43

3.1.1.2 Pozzolanic Materials

Fly ash (FA) is often used as an adequate partial substitute for cement in cementitious materials. Its pozzolanic reactions enhance the long-term strength of materials like mortars and concrete while improving cementitious structures' durability. The current investigation utilized FA sourced from a metal forging industry in Noida, UP (India), characterized by its light brownish color (Figure 3.3a). In addition to FA, blast furnace slag (BS) was employed as another iron-rich industrial waste product (IWP) sourced from the same industry mentioned above. The chemical composition of FA and BS (detected using EDS) are shown in Table 3.3. The specific gravity of FA and BS was assessed following BIS: 4031 (Part 11)-1988 [318], yielding values of 2.20 and 2.83, respectively. The additional physical properties of FA and BS are stated in Table 3.4. FA and BS's microstructure and chemical configuration were examined using scanning electron microscopy (SEM), EDS, and X-ray diffraction (XRD) analysis, with results presented in Figures 3.4 and 3.5, respectively. The comprehensive methodologies for executing these microstructure tests are elaborated upon in section 3.1.2.5

The SEM analysis revealed that most of the FA particles exhibited a spherical morphology, while the BS particles displayed a sub-angular shape. The SEM impressions of FA and BS contribute to the preliminary analysis of their particle grain size, with the results presented in Table 3.4. The EDS analysis revealed that the FA and BS contain significant quantities of silica (Si), aluminum (Al), and iron (Fe), categorizing them as pozzolanic materials. Therefore, FA and BS have been employed as substitutes for cement in the present study. Figure 3.5 displays the

XRD findings for the FA and BS particles, indicating that quartz (SiO_2) and hematite (Fe_2O_3) were the predominant crystalline phases detected in both IWPs. Furthermore, the XRD pattern of FA and BS revealed the existence of Wuestite (FeO), Magnetite (Fe_3O_4), and Corundum (Al_2O_3) as additional crystalline phases.

The analysis of the chemical composition (Table 3.4) and the XRD (Figure 3.4) crystalline phase observed in FA and BS reveals that the selected industrial waste materials are rich in iron, thus rendering them suitable for producing iron-rich cementitious composites.

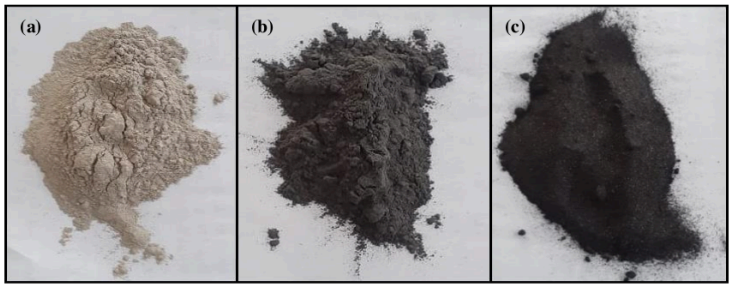

Figure 3.3 Classic images of IWPs utilized (a) FA, (b) BS, and (c) FS.

Table 3.3 Chemical composition of FA and BS (detected using EDS)

Element Oxides		FA (%)	BS (%)
Calcium Oxide	**CaO**	1.19	4.38
Silica Oxide	**SiO_2**	21.10	16.30
Aluminum oxide	**Al_2O_3**	12.90	1.95
Iron oxide	**Fe_2O_3**	11.76	47.25
Magnesium oxide	**MgO**	0.50	2.07
Sodium oxide	**Na_2O**	2.63	0.93
Potassium oxide	**K_2O**	1.05	0.36

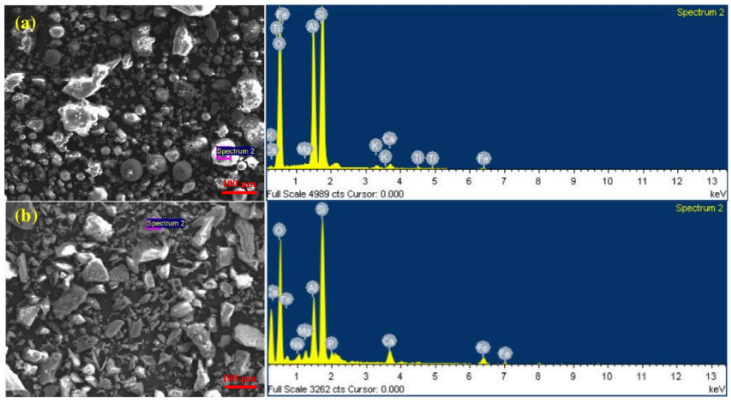

Figure 3.4 SEM-EDS impression of pozzolanic materials: (a) FA and (b) BS

Table 3.4 Physical properties of FA and BS

Property	FA	BS
Specific Gravity	2.20	2.28
Color	Light brownish	Grey
Particle shape	Round	Sub-angular
Particle size (μm)	6.8	8.5

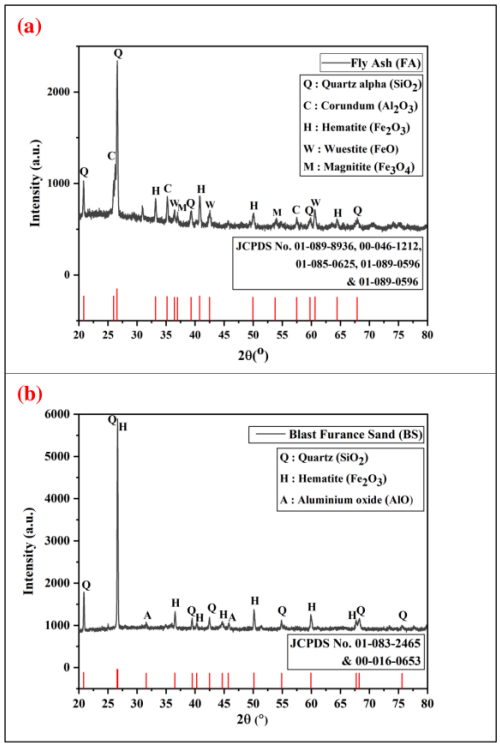

Figure 3.5 XRD pattern of Pozzolanic materials: (a) FA and (b) BS

3.1.1.3 Fine Aggregate

River sand acquired from local sources screened via a 4.75mm sieve and confirmed by IS: 383-1970 [319] was employed as fine aggregates in the current investigation. The river sand was partially replaced with another IWP, Foundry Sand (FS). It was also provided by the metal forging industry situated in Noida, UP (India). The chemical composition of FS, assessed through EDS, is presented in Table 3.5. The physical tests, including specific gravity, water

absorption, fineness modulus, and particle size distribution, were conducted on river sand and FS following the guidelines outlined in BIS: 2386 (Part 1)-1963 [320]. The outcomes of the physical tests and sieve analysis conducted on fine aggregates, as presented in Tables 3.6, 3.7, and 3.8, were considered satisfactory in compliance with BIS: 383-1970 [319]. Also, FS and river sand were sieved in accordance with EN1015-1:1999 (CEN 1999) [321] to achieve the optimal size distribution. Figure 3.6 depicts the trajectory of the particle size distribution for the sand and FS utilized in this study.

SEM, EDS, and XRD were conducted to analyze the microstructure and chemical composition, particularly the iron content of the FS used in this study. Figure 3.7 illustrates the FS's morphology and chemical composition as analyzed by SEM and EDS. The SEM image demonstrates that the FS particles exhibit irregular and angular characteristics. The EDS image of FS demonstrates a significant concentration of iron and silica, indicated by the pronounced peaks of iron (Fe), oxygen (O), and silicon (Si). Additionally, FS exhibited carbon black coloration (Figure 3.3c). Figure 3.8 illustrates the XRD pattern of the FS, indicating the presence of quartz (SiO_2) and hematite (Fe_2O_3) crystalline phases in the FS particles.

Since, the chemical composition and XRD analysis of FS indicate that the utilized river sand substituent, i.e., FS, is rich in iron, making it suitable for use along with other IWPs, i.e., FA and BS, in producing iron-rich cementitious composites.

Table 3.5 Chemical composition of FS (detected using EDS)

Element Oxides		**FS (%)**
Calcium Oxide	**CaO**	1.91
Silica Oxide	**SiO_2**	20.52
Aluminum oxide	**Al_2O_3**	6.10
Iron oxide	**Fe_2O_3**	21.68
Magnesium oxide	**MgO**	1.59
Sodium oxide	**Na_2O**	1.47
Potassium oxide	**K_2O**	0.29

Table 3.6 Physical properties of river sand.

Property	**Test value**

Specific Gravity	2.66
Bulk Density (kg/m^3)	1570
Water absorption (%)	3
Fineness modulus	2.64
Grading zone	II

Table 3.7 Physical properties of FS.

Property	**Test value**
Specific Gravity	2.27
Water absorption (%)	5.4
Fineness modulus	1.12
Particle size (μm)	247.8
Particle shape	Angular
Color	Carbon black

Table 3.8 Sieve analysis results of fine aggregates (River sand and FS)

Sieve Size	**Cumulative Mass Passing (%)**	
	River sand	**FS**
10 mm	100	100
4.75 mm	100	99.35
2.36 mm	91	98.95
1.18 mm	75.2	98
600 μm	60.2	97
300 μm	38	75.45
150 μm	9	18.3
Pan	0	0
Fine aggregates: confirmed zone II: (IS:383:1970) Weight of the sample = 1000 g		

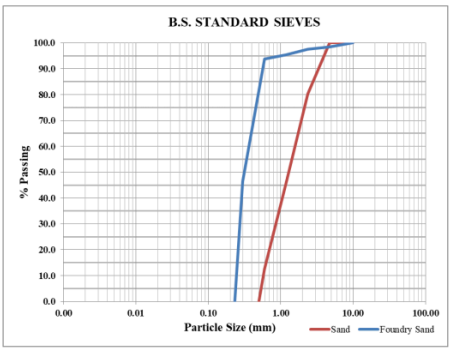

Figure 3.6 Particle size distribution curve of fine aggregates: River sand and FS.

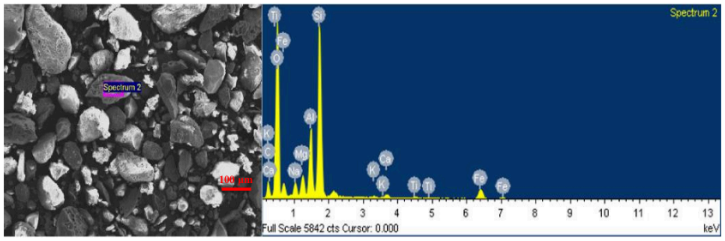

Figure 3.7 SEM-EDS impression of fine aggregate substituent: FS

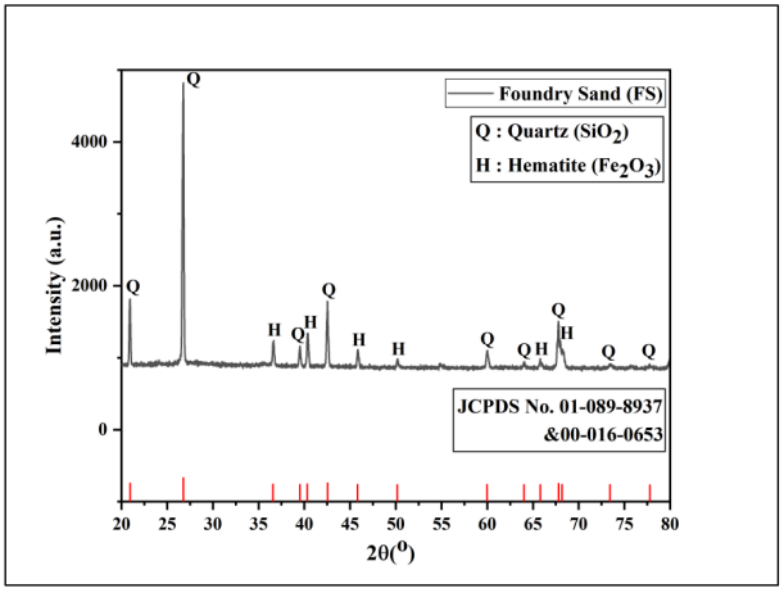

Figure 3.8 XRD pattern of fine aggregate substituent: FS

3.1.1.4 Super Plasticizer

Superplasticizers enhance the flow properties of fresh mixtures, facilitating easier placement and pourability. The current investigation utilized the Complact SP430 QCDA 443 super plasticizer manufactured by Fosroc Chemicals (India) Pvt. Ltd. at a dosage of 0.5% by weight of the binding material to obtain the flow characteristics of the mixture.

3.1.1.5 Water

According to IS 456: 2000 [322], the water utilized for curing cementitious mortar must be devoid of oil, organic salts, chemical materials, and other detrimental substances. This study recommends using potable water for iron-rich cementitious mortar production. The potable water in the institute's laboratory was utilized to prepare and cure cementitious specimens.

3.1.2 Mix Proportion and Testing Methods

3.1.2.1 Mix Design

The volume estimations of designed mortar mixtures were done by considering the number of specimens to be cast. A control mix was prepared to have a proportion of 1:3 (cement: sand by weight) with a w/b (water/binder) ratio of 0.5, agreeing to EN 196–1 [323]. Thus, the control

mixture ($C_{100}S_{100}$) incorporates 527 kg/m^3 Portland cement, 1581 kg/m^3 river sand, and 263.5 kg/m^3 water. The literature reports that cementitious material incorporating typically 30–50% of supplementary cementitious materials - SCMs (FA and BS) as cement replacements showed better strength and durability than the control samples [324]–[331]. Therefore, FA and BS were replaced at 10% (constant) and 5–30% (varying by 5%) by weight of cement while designing different mortar mixtures, respectively. The literature also registers that the building material having sand substituted with FS up to 15% attains maximum beneficial strength properties [243], [332], [333]. Therefore, the FS replaced sand at a constant rate of 15% by the weight of sand during different mortar mixtures. In total, seven mortar mixtures (including the control mixture) were prepared with a constant 0.5 w/b ratio. Different mortar configurations (C_XS_Y) and designs are listed in Table 3.9.

Table 3.9 The present study design mixtures prepared using different proportions of IWPs

S.No.	Mix Design	Cement (C) (kg/m^3)	Sand (S) (kg/m^3)	FA (kg/m^3)	BS (kg/m^3)	FS (kg/m^3)	Water (kg/m^3)
1.	$C_{100}S_{100}$	527	1581	0	0	0	263.5
2.	$C_{85}S_{85}$	447.9	1343.85	52.7	26.4	237.15	263.5
3.	$C_{80}S_{85}$	421.6	1343.85	52.7	52.7	237.15	263.5
4.	$C_{75}S_{85}$	395.2	1343.85	52.7	79.1	237.15	263.5
5.	$C_{70}S_{85}$	368.9	1343.85	52.7	105.4	237.15	263.5
6.	$C_{65}S_{85}$	342.55	1343.85	52.7	131.75	237.15	263.5
7.	$C_{60}S_{85}$	316.2	1343.85	52.7	158.1	237.15	263.5

*Note: In the terminology CxSy, X represents the percentage of cement, while Y denotes the percentage of sand in the specified design mix.

3.1.2.2 Specimen Casting And Preparation

The physical and chemical properties of different components were assessed before the casting procedure. Also, all instruments were cleaned and thoroughly inspected for openings or gaps. Every ingredient was quantified with a weighing balance and mixed in the mortar mixer. Initially, the dry components, including OPC, IWPs, and river sand, were blended in the mortar mixer for approx. 15 min until dry homogenized mixture exhibiting a consistent color

throughout was achieved. Subsequently, 60% of water was added, and the mortar mixture was agitated for approx. 2 min until proper uniformity was attained. The remaining 40% water was added with the superplasticizer dosage and mixed for a furthur 2 min. After preparing C_XS_Y mixes in the mixer, the fresh properties were assessed and verified against the specified requirements [322] for all C_XS_Y mixes. Upon satisfying the criterion for the fresh property, the specimens were cast to test the hardened properties.

The cubical, prismatic, and cylindrical molds went through complete cleaning, tightening, and proper oiling before casting. During the casting of specimens, each fresh mortar mixture underwent compaction for a minimal duration of 15 sec utilizing a vibration machine. After 24h of casting, all prepared specimens were de-molded, labeled, and subsequently cured in a water container for 7, 28, and 56 days in an ambient or controlled environment, as outlined in EN 196–1 [323] and shown in Figure 3.9.

The strength properties of different mortar mixtures were evaluated by assessing compressive strength, flexural strength, and split tensile strength at a curing age of 7 and 28 days, respectively. For assessing the compressive and flexural strength of different mixtures, prismatic specimens with dimensions of 40*40*160 mm were cast. Whereas, split tensile strength was determined using cylindrical specimens with a length of 200 mm and a diameter of 100 mm. To examine the longevity, durability, and pozzolanic properties of the utilized IWPs in different design mixtures, extra prism specimens were cast to evaluate the compressive strength at curing ages of 56 days, respectively.

Also, extra 40*40*160 mm prismatic and 70.6mm cube specimens were cast to examine physical and durability properties like porosity, real, bulk, and dry density, and water absorption by immersion and capillary action. The microstructure of different mixture designs was analyzed utilizing FESEM, XRD, and EDS techniques. For this purpose, the testing fragments were collected from the innermost part of the ruptured cube samples and subjected to compressive strength testing. Table 3.14 details the different material testing standards employed during preparing and casting C_XS_Y design mixtures and their respective hardened properties.

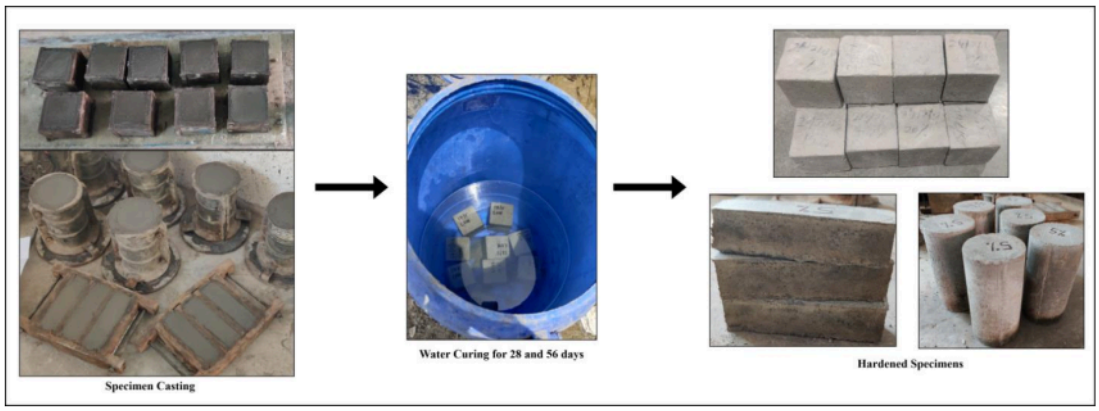

Figure 3.9 Various stages while casting different design mixture (C_XS_Y) hardened specimens.

3.1.2.3 Material Testing Standards

Table 3.10 summarizes the standard protocols for preparing and casting the C_XS_Y mixtures and the testing methods utilized to evaluate the fresh and hardened properties of these developed iron-rich cementitious mortar specimens.

Table 3.10 Different material testing standards followed during the preparation and casting of C_XS_Y design mixtures and specimens.

Fresh State Properties			
Property	**Reference Code**	**Sample**	
Slump test (mm)	**IS 1199: Part 2: 2018**	Prior to sample casting	
Fresh Density ($kg/m^{3)}$	**ASTM C138**	Prior to sample casting	
Strength Properties			
Property	**Reference Code**	**Testing age (days)**	**Sample Size**
Compressive Strength (N/mm^2)	EN 1015-11	7, 28 and 56	Prism: 40x40x160 mm
Flexural Strength (N/mm^2)	EN 1015-11	28	Prism: 40x40x160 mm
Split Tensile Strength (N/mm^2)	IS 5816–1999	28	Cylinder: 100x200 mm
Microstructure studies			
Analysis	**Instrument**	**Testing age (days)**	**Sample**
SEM	JSM6510LV scanning electron microscope	28 and 56	Broken cementitious pieces obtained during compressive strength
EDS	model INCA51-	28 and 56	

	ADD0076		testing.
XRD	PANalytical Xpert Pro utilizing Cu Kα wavelength (1.5405)	28 and 56	
TGA	NETZSCH model STA 449 F3 Jupiter	28 and 56	
Physical Properties			
Property	**Reference Code**	**Testing age (days)**	**Sample Size**
Porosity (%)	RILEM 1980	28	Prism: 40x40x160 mm
Density (real, bulk and dry) (kg/m^3)	RILEM 1980	28	Prism: 40x40x160 mm Cube: 70.6 mm
Durability Properties			
Property	**Reference Code**	**Testing age (days)**	**Sample Size**
Water absorption by immersion (%)	RILEM 1980	28	Prism: 40x40x160 mm

3.1.3 Fresh State Characteristics of Different Mixture Designs

Fresh properties are related to the workability of cement mortar, indicating the ease of mortar placement. The workability of sustainable cementitious mixtures was assessed through slump and fresh density testing.

3.1.3.1 Slump Test

The slump test is a widely utilized test method for assessing the workability of fresh cement mortar. It is a cost-effective test and is extensively utilized in field applications worldwide. The apparatus comprises a mould in the form of a conical frustum, including a top diameter of 60 mm, a base diameter of 70 mm, and a height of 35 mm, as illustrated in Figure 3.10. To estimate the slump, the mortar was introduced into the mould in three layers, with each layer being compacted by 25 strokes using a tamping rod.

Once the slump cone mould was filled with compacted mortar, it was elevated vertically, and the alteration in the height of the fresh mortar was noted. Four categories of variations in height are generally observed, as illustrated in Figure 3.11. The most suitable shape for diverse applications is the real slump, while zero and collapsed slumps are undesirable and fall outside the parameters of this testing procedure.

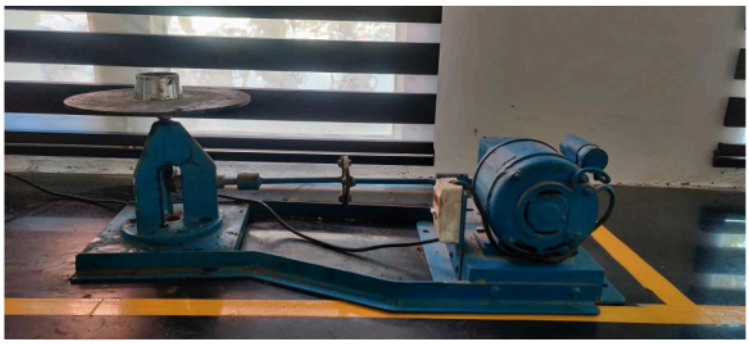

Figure 3.10 Apparatus for determination the workability using slump flow test.

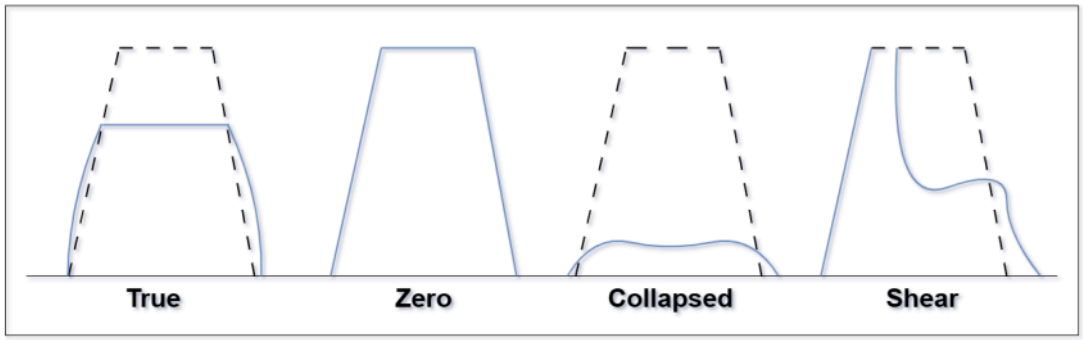

Figure 3.11 General categories of slump.

3.1.3.2 Fresh Density

The fresh density of cement mortar is defined as the mass per unit volume of the mortar in its fresh state. This property plays a vital role in construction, directly influencing the workability, durability, and structural properties of the mortar. Determining the fresh density assures the mix's uniformity, compatibility with design standards, and facilitates the quality control throughout construction.

The procedure starts with preparing the mortar mix, utilizing precise proportions of cement, sand, and water (mentioned in section 3.1.2.1), mixed thoroughly to ensure uniformity. The cubical (or any other shape) container's internal dimensions are measured to determine its volume, denoted as V in m^3. The container is then positioned on a flat surface and filled with mortar in three compacted layers, each roughly one-third of the container's volume, with any extra mortar leveled out. The weights of the filled container, W_a, in kg, and the empty container,

W_b, in kg, are measured using the weighing scale. The fresh density of the cement mortar is calculated using the formula as given below (equation 3.1):

$$\textbf{\textit{Fresh Density}}\ (D_f)(kg/m^3) = \left(\frac{W_a - W_b}{V}\right) \qquad 3.1$$

3.1.4 Strength Characteristics of Different Mixture Designs

The hardened mortar's strength is a critical factor in evaluating the structural performance of a cementitious material, such that, each strength property is essential in determining the mortar's overall performance in building applications and is directly linked to its durability.

3.1.4.1 Compressive Strength

This is an important test to assess the strength of cementitious mortar in its hardened form. Cubes serve as samples, and their testing occurs at different curing periods. The evaluation is conducted using a Universal Testing Machine (UTM) or a Compressive Strength Testing Machine (CTM). The machine was operated at a consistent loading rate of 2.85 kN/sec, as specified by the test requirements. Cured cube samples are positioned between the plates of the testing apparatus, after which a load is applied at a specified pace (as shown in Figure 3.12). The sample is positioned centrally on the plates to guarantee even load distribution. The specific load at which the sample shows cracking or fracturing is recorded. For every mixture, three samples were evaluated, and the results were documented as their average at the curing period of 7, 28, and 56 days, respectively. The compressive strength of the specimens was calculated using the following formula (equation 3.2), i.e.,

$$\textbf{Compressive strength } (F_{ck})\ (N/mm^2) = \frac{\textbf{maximum load applied (P)}}{\textit{Cross-sectional area}\ (A)} \qquad \textbf{3.2}$$

Figure 3.12 Experimental setup employed for determining the compressive strength of mortars.

3.1.4.2 Flexural Strength

Prismatic samples were used to assess the flexural strength, and the testing was conducted after a 28-day curing period. The assessment was performed with UTM or CTM. The loading rate for testing the samples in the UTM was 16.48 kN/sec, in accordance with test specifications. The center-to-center distance of the support, i.e., 120mm, was utilized as the effective length for the computation of flexural strength. The dial gauge is positioned at the beam's base to evaluate the deflection at the midpoint. The configuration and placement of the dial gauge are illustrated in Figure 3.13. The flexural strength for central point loading has been estimated using equation 3.3. The average of the three tested specimens' findings was given.

$$\textbf{Flexural strength } (F_f)\left(\frac{N}{mm^2}\right) = 1.5 \times \frac{Pl}{bd^2} \qquad 3.3$$

Where P = maximum load applied to the specimen (N) and l, b & d = mold internal dimensions, i.e., length, width and height (mm).

Figure 3.13 : Experimental setup employed for determining the flexural strength of the prism specimens.

3.1.4.3 Split Tensile Strength

Cylindrical specimens were prepared to evaluate the split tensile strength at a curing period of 28 days. The cylindrical specimen was set up in the CTM with its central axis oriented perpendicular to the loading axis, as illustrated in Figure 3.14. The loading rate for the test was 44.94 kN/sec, in keeping with the specified test parameters. The load was applied steadily and smoothly until the specimen was broken into two pieces. The test findings were presented as the average of three cylindrical specimens. The specimen's maximum load was noted, and the split tensile strength was computed as follows (equation 3.4):

$$\textbf{Split Tensile Strength, } f_{ct}\ (\text{N/mm}^2) = \frac{2P}{\pi dl} \qquad \textbf{3.4}$$

where P = maximum load applied to the specimen (N) and d,l = cross-sectional dimension and length of the specimen (mm).

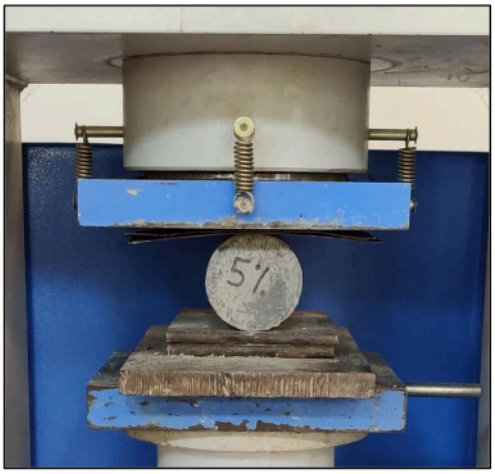

Figure 3.14 Experimental setup employed for determining the split tensile strength of the cylindrical specimens.

3.1.5 Physical Characteristics of Different Mixture Designs

The physical characteristics of hardened cementitious specimens serve as vital indicators of their suitability, durability, and performance in several construction applications. Each physical property is crucial in assessing the material's long-term durability and resistance against external stresses.

3.1.5.1 Open Porosity, and Density (Real, Bulk & Dry)

The porosity is characterized by the amount of void spaces existing in the cementitious mortar matrix. The transport of fluids within the mortar matrix occurs via porous media and through mechanisms of diffusion and absorption. The effective porosity of a hardened mortar is usually quantified through its water absorption measurement.

The real density can be described as the mass ratio to the impermeable volume of hardened mortar. In contrast, the bulk density can be described as the mass ratio to the hardened mortar's bulk volume. Calculating the real, bulk and dry density of mortar is essential for quality control, ensuring that the mortar possesses the requisite properties to deliver strength and durability to a cementitious structure. Therefore, these properties constitute the critical elements in the mortar matrix microstructure.

The tests were performed on prismatic specimens that had been cured for a duration of 28 days. Following a 28-day curing period, the samples were dried until a consistent M_1 mass was achieved. The dried samples were subsequently placed in a desiccator under low pressure, specifically 20 mm Hg (2667 Pa), for 24h to remove the air trapped within the sample's pores. After 24h, the desiccator was gradually filled with tap water while containing samples, ensuring that vacuum conditions were preserved during the water introduction process (Figure 3.15). The samples were immersed in water for an additional 24h at atmospheric pressure, after which they were weighed under vacuum in two conditions: M_2, weight immersed, and M_3, weight in air or at atmospheric pressure. The recorded values were utilized to calculate open porosity, real and bulk density using equations 3.5 to 3.7.

$$\textbf{Porosity}\ (\%) = \frac{(M_3 - M_1)}{(M_3 - M_2)} \times 100 \qquad 3.5$$

$$\textbf{Real Density}\ (\%) = \frac{(M_1)}{(M_3 - M_2)} \times 1000 \qquad 3.6$$

$$\textbf{Bulk Density}\ (\%) = \frac{(M_1)}{(M_1 - M_2)} \times 1000 \qquad 3.7$$

Figure 3.15 Samples placed in a desiccator containing water under atmospheric pressure.

3.1.6 Durability Characteristics of Different Mixture Designs

To evaluate the structural integrity of cementitious mortar, durability is a crucial factor in addition to strength and reliability. It provides an indication of the duration for which the cementitious structure remains functional and the maintenance necessary to sustain its serviceability.

3.1.6.1 Water Absorption By Immersion

The water absorption by immersion of cementitious mortar refers to its capacity to take in external fluids and occupy the pore spaces within the mortar matrix. The effective porosity of a hardened mortar is usually quantified through its water absorption measurement. Furthermore, it is a critical parameter that affects the long-term performance of mortar in diverse environmental conditions.

The tests were performed on prismatic specimens that had been cured for a duration of 28 days. Following a 28-day curing period, the samples were dried until a consistent M_1 mass was achieved. The dried samples were subsequently placed in a desiccator under low pressure, specifically 20 mm Hg (2667 Pa), for 24h to remove the air trapped within the sample's pores. After 24h, the desiccator was gradually filled with tap water while containing samples, ensuring that vacuum conditions were preserved during the water introduction process (Figure 3.15). The samples were immersed in water for an additional 24h at atmospheric pressure, after which they were weighed under vacuum in two conditions: M_2, weight immersed, and M_3, weight in air or at atmospheric pressure. The recorded values were utilized to calculate water absorption by immersion of different cementitious mortar specimens, as indicated in equations 3.8.

$$\textbf{Water absorption by immersion } (\%) = \frac{(M_3 - M_1)}{(M_3)} \times 100 \qquad 3.8$$

3.1.7 Microscopic Studies of Different Mixture Designs

The residual specimens underwent microstructure analysis following the destructive tests of hardened mortar. SEM and EDS analyses were conducted to examine the microstructure and chemical composition. Additionally, XRD testing was performed for phase identification. Thermo-gravimetric analysis (TGA) was utilized to evaluate the thermal properties of different mixture designs.

3.1.7.1 SEM and EDS

The microscopic structure of hardened mortar, particularly the degree and type of the binding at the cement-IWPs-sand interface, was examined using a JSM 6510LV model from JEOL (Japan). This was accomplished by preparing the samples in a manner that enabled the fiber matrix interaction to be captured in SEM. The elemental analysis was performed using EDS employing model INCA51-ADD0076 from Oxford Instruments, Abingdon, United Kingdom.

3.1.7.2 XRD

The PANalytical Xpert Pro utilizing Cu Kα wavelength (1.5405) was employed to examine the crystalline structure of different mixture designs. The scan was obtained at 2θ angle ranging from 10° to 80°.

3.1.7.3 TGA/DTA

The SDT Q600 TGA/DTA (TA Company, USA) was utilized to assess thermal properties. Thermo-gravimetric (TG) study of different mixture designs was performed to determine the mass loss and chemical degradation. A 5°C/min heating rate was employed from 25°C to 1000°C in a nitrogen environment. A 10 mg sample was utilized to acquire the TG curve of the specimens.

3.2 Section B: Fabrication and Analytical Examination of Fe_2TiO_5 Heterostructure For Cementitious Composite

3.2.1 Fabrication of Fe_2TiO_5 Heterostructure For Cementitious Composite

3.2.1.1 Photocatalyst

The photocatalyst P25-TiO_2, a 70:30 blend of anatase and rutile phase of Titanium Dioxide, was obtained from Sigma Aldrich Chemicals Pvt. Ltd, Delhi (India). It possesses an average particle size of 30nm and a BET surface area of 5 x $10^3 cm^2/g$. It has been utilized as a photocatalyst in this research.

3.2.1.2. Encrustment of TiO_2

The best mix design which performed better than the control mix (C100S100) in terms of strength and durability properties was selected for the further testing, specifically, the mortar specimens of $C_{85}S_{85}$ mix design (the best-optimized mix) have been utilized for preparing the

Fe_2TiO_5 heterostructure for cementitious composite. Under this, the photocatalyst coating was applied using the dip coating approach []. A 1% (w/v) TiO_2 solution, i.e., 1 g of TiO_2 in 100 mL of distilled water, was sonicated for at least 30min to attain the uniform dispersion of TiO_2 nanoparticles. Following that, mortar specimens were dipped/submerged for 24h or more in the container having TiO_2 solution, as shown in Figure 3.16. A sufficient time and periodic shaking were arranged for adequate coating of TiO_2 on the mortar specimens. For decent coverage on the outer surface of the specimens, a minimum of 2 layers of TiO_2 were implemented.

Figure 3.16 TiO_2 encrustment process to synthesize Fe_2TiO_5 Heterostructure Composite.

3.2.1.2 Calcination Treatment

Following the effective deposition of TiO_2 onto the external surface of the cementitious specimens, the resultant material underwent a standardized temperature-time experimental procedure. The coated cementitious specimens were continuously muffled at a rate of 5°C/min from 25°C to 350°C and then kept at 350°C for 2h. The muffled specimens were cooled down at room temperature. After that, the coated specimens were washed using distilled water to eliminate the loosely bonded TiO_2 particles and oven-dried at 100^0C. After each course of layering, this procedure was replicated to ensure the complete coverage of the cementitious specimens with photocatalyst TiO_2. This treatment facilitates the natural incorporation of iron (Fe^{3+} from IWPs) into the TiO_2 lattice, resulting in the formation of a surface-active Fe_2TiO_5

heterojunction oxide layer, which is encrusted on the fabricated cementitious samples (further discussed in chapter 4). Using scanning electron microscopy (SEM), the thickness of the surface-active Fe_2TiO_5 heterojunction oxide layer over the substrate was determined, and it turned out to be 13.267µm (average), as shown in Figure 3.17. Accordingly, after the calcination treatment, the substrate has been designated as a 'Fe_2TiO_5 heterostructure for cementitious composite' to indicate the formation of an organic heterojunction featuring two distinct catalysts, specifically, Fe^{3+} (derived from IWPs) and TiO_2.

For controlled experiments (boundary conditions), the uncoated-$C_{100}S_{100}$, uncoated-$C_{85}S_{85}$, and simple-TiO_2 coated samples were prepared following the method discussed in the preceding section 3.2.1.2. The "uncoated- $C_{100}S_{100}$ cementitious samples" refers to uncoated-control cementitious mortar samples, whereas "uncoated- $C_{85}S_{85}$ cementitious samples" refers to uncoated cementitious mortar specimens cast using IWPs substitution. On the other hand, "simple-TiO_2 coated cementitious samples" refer to control ($C_{100}S_{100}$) cementitious mortar samples that were coated with simple P25-TiO_2.

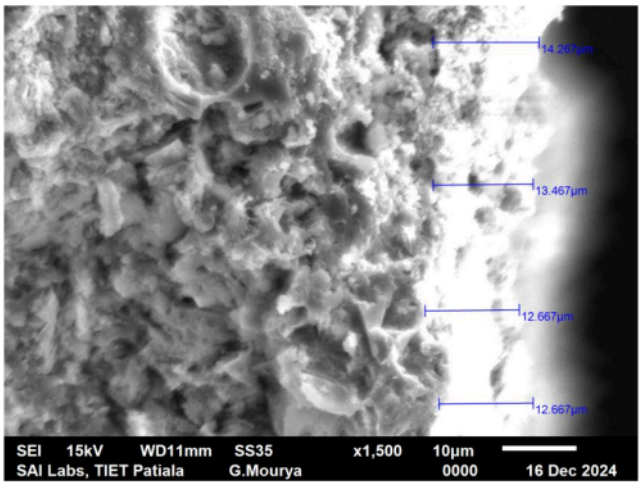

Figure 3.17 SEM image depicting the thickness of the TiO_2 coating (average thickness 13.267 µm) on a cementitious composite.

3.2.2 Analytical Examination of Fe_2TiO_5 Heterostructure For Cementitious Composite

To confirm the presence of Fe and TiO_2 in the synthesized Fe_2TiO_5 heterostructure and its formation, the heterostructure composite was examined using various approaches such as SEM, FESEM, EDS, XPS, XRD, FTIR, Raman Spectra, HRTEM, UV-DRS, TEM-SAED, BET and elemental mapping (EDX). The morphological investigation with elemental characteristic check was performed utilizing scanning electron microscopy (SEM) using the JSM 6510LV model from JEOL (Japan), which is equipped with energy-dispersive X-ray (EDS) and Energy-Dispersive X-ray Analysis (EDX). A JEC-3000FC auto fine coater was utilized to apply a platinum coating on the samples. X-ray diffraction (XRD) using PANalytical Xpert Pro was employed to explore the crystallography of the Fe_2TiO_5 heterostructure composite with phases detected within 20^0 to 80^0C scanning field using copper-K radiation with a wavelength of 1.5418 Å. The compound correlation and connectivity were analyzed using the Fourier Transform Infra-Red Spectrophotometer (FTIR) model RZX (PerkinElmer) within a 4000 to 200 cm^{-1} scanning field. The sample for FTIR spectra was pre-prepared, such that it was a mixture of 0.5 mg heterocomposite with 20mg (KBr) potassium bromide. To study the surface-chemical morphology of the Fe_2TiO_5 heterostructure composite, X-ray photoelectron spectroscopy (XPS) was employed using XPS, Omicron Nanotechnology, and Oxford Instruments. High-resolution transmission electron microscopy (HRTEM) was utilized to examine the lattice spacing of the working catalyst in the heterostructure composite. The energy band gap of the photocatalyst and heterostructure composite was measured using a UV-vis diffuse reflectance spectrometer (DRS), UV-2600, Shimadzu (Asia Pacific) within 200 to 800 nm wavelength range. The instrument utilized $BaSO_4$ as a standard reference material. The Raman spectroscopy was conducted using a confocal micro Raman spectrometer (STR 500, Airix Corporation, Japan) paired with a diode green laser operating at 532 nm. Thermo-gravimetric analysis (TGA) was conducted using the SDT Q600 TGA/DTA from TA Company, USA. A sample weighing approximately 30 mg was employed for the study, and the scanning process occurred within a temperature range of 25 °C to 1000 °C in a nitrogen environment. Transmission electron microscopy (TEM) with Selected Area Electron Diffraction (SAED) analysis was conducted using an FEI Morgagni 268 operating at 80 kV to better understand the presence of TiO_2 and Fe in the synthesized composite and also, to validate the XRD findings. The heterostructure composite's specific surface area, pore size, and pore volume were determined using the Brunauer-Emmett-Teller (BET) adsorption

technique (Quantachrome Ins, Auto-sorb-iQA3200-4). To conduct different examinations, the catalyst powder was carefully extracted by gently scraping from the surface of the composite, excluding SEM/EDS. The fragmented and miniature portions of the heterostructure composite were employed directly for analysis using SEM/EDS.

3.2.3 Photocatalytic and Antibacterial Property Check for the Fe_2TiO_5 Heterostructure For Cementitious Composite

3.2.3.1 Evaluation of the Photocatalytic Properties of the Fe_2TiO_5 Heterostructure

Chemicals and Reagents

Methylene blue (MB, $C_6H_{18}N_3SCl \cdot 3H_2O$, ≥ 98.5%) and distilled water.

Experimental Program

The photocatalytic efficiency of the Fe_2TiO_5 heterostructure was evaluated using methylene blue (MB), an organic dye recognized as a model for water contamination, as illustrated in the Figure 3.18. The experiments were performed in a glass batch reactor with an inverted conical frustum design, measuring 20.1 x 5.6 cm and possessing a capacity of 1000 ml. The baseline concentration of the MB solution was established at 20 mg/L, with a volume of 250 mL for the testing solution. The photocatalytic study was conducted under solar irradiation, with average solar radiation measured between 590 and 600 W/m² during the trials. The Fe_2TiO_5 heterostructure samples were uniformly distributed around the reactor's surface. Before the photocatalytic reaction, the heterostructure samples were immersed in methylene blue solution and agitated in the dark for 45 min to attain adsorption equilibrium. Following that, the solution underwent solar irradiation, and liquid samples were collected before and during the irradiation at consistent time intervals with a syringe. To ensure uniformity, the reaction was aerated at a rate of 3 L/min utilizing a sparger strategically located at the reactor's midpoint. The concentration of MB was quantified with UV–Vis absorption spectroscopy.

Figure 3.18: Batch experimental setup for evaluating the photocatalytic performance of the Fe_2TiO_5 heterostructure for cementitious composite.

3.2.3.2 Evaluation of Photocatalytic-Induced Antibacterial Properties of the Fe_2TiO_5 Heterostructure

Chemicals and Reagents

Miller Luria Bertani (LB) (10g BactoTM Tryptone, 10g NaCl, and 5g Yeast extract) and Agar-Agar, Type 1, were received from HiMedia Laboratories located in Mumbai (India). The bacteria washing and re-suspension were carried out in sterilized isotonic sodium chloride (NaCl - 99.5%) saline solution. NaCl was purchased from SD Fines Chemicals Ltd, India.

Bacteria

The standard type of *Escherichia coli (E. coli)* K12 strain has been utilized in the present study to investigate the bactericidal/antibacterial efficiency of the Fe_2TiO_5 heterostructure composite. It was initially received from the Microbial Type Culture Collection (MTCC) and Gene Bank in Chandigarh (India) and was immediately stored at a temperature of -20^0C in a liquid solution containing 20% glycerol.

Bacterial Maturation

E. coli is a non-pathogenic bacterium and serves as an indication of the microbes associated with gastrointestinal disorders. Its strains were cultivated using a 20% glycerol solution and stored at -20°C in cryoscopic containers. The colony derived from the sample strain was streaked onto the

agar plate to establish the pre-cultures for each experimental run. The plates were then placed in an incubator set at 37°C for 24h. Next, the developed colony was re-plated on a fresh agar plate and incubated at 37°C for 24h. To conduct testing, the cell pellet was derived by carefully selecting the colony from the pre-cultures using a loop and then introducing it into a 50 mL sterile borosil Erlenmeyer flask containing 5 mL of LB broth solution.

Next, the flask was placed in an incubating shaker elevated to 37°C and rotated at 180 rpm. After 8h, a 1% dilution of bacterial cells was prepared in a sterilized 250 mL Erlenmeyer flask containing 50 mL of LB broth solution that had been previously autoclaved. The cells were cultured under aerobic conditions at 37°C until they reached a physiological stationary phase. The optical density (OD) at 600 nm was used to quantify bacteria's stationary and growing phases. The extracted *E. coli* culture was centrifuged at 5000 rpm at 4°C for 15min to dissociate its medium from the bacterial cells. After this, three isotonic (0.85% NaCl) solution washes were performed on the resultant bacterial pallet. After obtaining the final bacterial pellet, it was again suspended in the 50 mL saline solution. The outcome of this approach was a cell density of nearly 10^9 colony-forming units per milliliter (CFU/mL). This cellular density was then utilized in all the investigations conducted in this work.

The *E. coli* concentration in the test sample (CFU/mL) was determined by plating on LB-agar plates. In the studies, a 1mL sample was extracted, preserved at 4°C, and promptly inoculated onto the agar plate with the usual plate count technique. Furthermore, the plating was executed by distributing 0.1mL of the *E. coli* test sample onto petri plates. Serial dilutions were performed on each test sample to get the requisite concentration of *E. coli*. The plates were incubated overnight at 37°C after plating, and colony counts were performed manually.

Experimental Program

The antibacterial properties of the Fe_2TiO_5 heterostructure were evaluated utilizing a bacterial water suspension. A batch experiment was conducted in a 20.1 x 5.6 cm inverted conical frustum glass reactor of 1000 ml capacity exposed to solar irradiation to examine the *E.coli* inactivation capability of the Fe_2TiO_5 heterostructure composite (Figure 3.19). To acculturate the bacteria, 250 ml solution with 10^6 CFU/ml bacterial counts was added to the glass reactor and agitated for 30min. The disinfection setup was conducted at the Thapar University between 12:00 pm to 2:30

pm from September to November. From the commencement to the conclusion of the investigations, the mean solar irradiance was noticed to be between 590 & 600 W/m^2. The Fe_2TiO_5 heterostructure composite pieces were uniformly distributed on the reactor's surface. To maintain homogeneity, the reaction was aerated at a rate of 3 L/min using 2 spargers positioned precisely at the midpoint of the reactor. For the time-dependent study, an adequate quantity of samples was withdrawn from the batch reactor at consistent time gaps utilizing a syringe. Subsequently, these samples were inoculated onto an agar plate to determine the bacterial cell count. The bacterial cell count was determined in the form of CFU/mL utilizing the standard Petri plate technique. The bacterial inactivation efficiency comparison of the Fe_2TiO_5 heterostructure composite with simple TiO_2 cementitious samples has been examined in the proposed study. The inactivation efficiency of the composite was detected using unit log reduction of *E. coli* (L_e), as given in equation 3.9 below:

$$L_e = Log \frac{A_f}{A_i} \qquad 3.9$$

Where A_i and A_f indicate the initial concentration and concentration at a particular treatment time (measured at a specific moment during the experiment), respectively.

Figure 3.19 Batch experimental setup for evaluating the antibacterial property check of the Fe_2TiO_5 heterostructure composite.

K^+ Ion Leakage Test and FESEM For E.Coli Morphology

The Carl Zeiss Sigma 500 FEG-SEM instrument was employed for FESEM analysis for assessing the morphological alterations in bacterial cells following treatment with the Fe_2TiO_5 heterostructure in deionized water.

Potassium ions (K^+) are common in all bacterial species [] and are essential for accurately controlling protein synthesis and polysome composition. Therefore, the present study utilizes Flame photometry following test method 3120B as outlined in the APHA 23rd edition to determine K^+ ion leakage from *E. coli* to help investigate bacterial cell wall permeability. A comparative analysis of treated and untreated water utilizing the Fe_2TiO_5 heterostructure was performed through K^+ ion leakage tests on both initial (untreated) and final (treated) samples.

Trapping Study

Previous studies indicate that bacteria are inactivated mainly by generating reactive oxygen species (ROS) by photocatalysts, which occurs via separating electrons (e^-) and holes (h^+). Three principal ROS have been identified in the photocatalytic disinfection of microbes: hydroxyl radical (OH^o), hole (h^+), and superoxide radical ($O_2^{\bullet-}$). Scavengers are an efficient method for evaluating the role of each reactive species in photocatalytic disinfection and understanding its process. To identify the primary oxidative species or radicals (i.e., OH^o, $O_2^{\bullet-}$, and h^+) responsible for the photocatalytic inactivation of *E.coli* using Fe_2TiO_5 heterostructure composite, experiments were conducted under optimal conditions over a 60 min reaction period, utilizing various quenching agents such as tert-butyl alcohol (TBA) for OH^o, disodium ethylene diamine tetraacetic acid (EDTA) for h^+, and p-benzoquinone (BQ) for $O_2^{\bullet-}$ at a concentration of 0.01 M. Double-distilled water was employed in the preparation of each solution.

Photoluminescence (Pl) Study

The hydroxyl radicals (OH^o) generated during the photocatalytic process of the Fe_2TiO_5 heterostructure composite were identified using a fluorescence spectrophotometer at a wavelength of 460 nm, with the PL spectra recorded on a Shimadzu RF-5301 Spectro-fluoro-photometer. This method entails the reaction between OH^o and Na (sodium) salts of terephthalic acid (TPA) (with a purity > 98% of Analytical Reagent (AR) grade), yielding 2-hydroxy

terephthalic acid, a luminescent compound. The existence of OH^o was validated by assessing the fluorescence of the 2-hydroxy terephthalic acid molecule with a fluorescence spectrophotometer.

3.3 Section C: Photocatalytic Treatment of Bioaerosols Using Fe_2TiO_5 Heterostructure Composite

3.3.1 Bacteria and Its Maturation

As previously mentioned, the bacterial strain employed in this study is *Escherichia coli (E. coli)* wild-type K12, sourced from the Microbial Type Culture Collection (MTCC) and Gene Bank in Chandigarh, India. This organism is non-pathogenic and acts as an indicator for the microbes linked to gastrointestinal disorders. The methodology employed for bacterial growth has been described in the preceding section 3.2.3.2.

3.3.2 Experimental Investigation: Setup and Sampling

A 41 x 21 x 32 cm^3 reaction glass chamber was installed to evaluate the antibacterial efficiency of the Fe_2TiO_5 heterostructure against *E.coli* bioaerosols. To ensure a consistent atmosphere for the disinfection experiments, a fan was installed on the central ceiling of the glass chamber. The cotton ssaturated with bacteria was kept in the middle of the chamber base to be used as a bacterial source for disinfection tests. To generate visible light for the photocatalytic disinfection experiments, a total of 20W visible light source was installed at the upper part of the reaction chamber. Further specifics of the chamber are depicted in Figure 3.20. The antibacterial experiment was conducted for different time intervals, during which the temperature and humidity inside the glass chamber were maintained at 30°C and 65 ± 5 %, respectively. After each time interval experiment, the Fe_2TiO_5 heterostructure composite specimens initially placed inside the chamber were moved to a test solution with 2.5 % Luria Bertani (LB), i.e., 2.5 g of LB in 100 ml of double distilled water. The purpose of this transfer was to isolate bacteria from the specimens. The solution was incubated for 8 to 12h and then diluted accordingly before spreading onto an agar plate. The preliminary bacterial count after each experiment was determined by quantifying the number of bacteria on the uncoated-$C_{100}S_{100}$ cementitious specimen placed next to the specific specimen being studied. The potency of Fe_2TiO_5 heterostructure composite in inhibiting bacterial growth was measured using the logarithmic reduction in *E.coli* (Le) as expressed in equation 3.10:

$$L_e = Log \frac{A_f}{A_i} \quad 3.10$$

Where A_f and A_i indicates initial and particular treatment time (measured at a specific moment during the experiment) concentration, respectively.

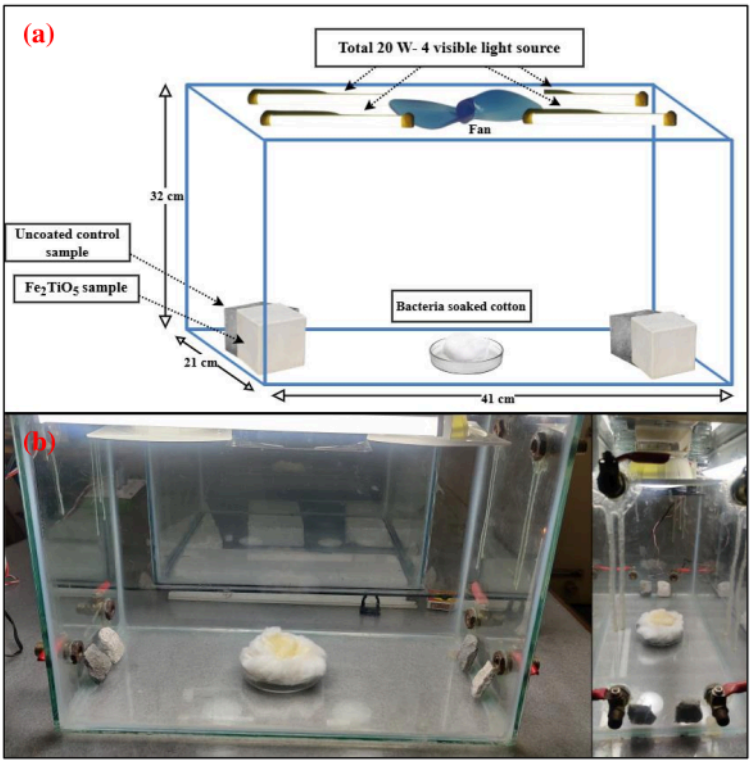

Figure 3.20 (a) Schematic line diagram and (b) Actual front and side views of the glass reactor chamber utilized for the disinfection procedure of *E. coli* bioaerosols.

3.3.3 Photocatalytic-Induced Antibacterial Efficiency Comparison

The same methodology (discussed in section 3.3.2.) was used to assess the pre-determined boundary conditions for the present antibacterial investigation. The study's boundary condition was evaluated by conducting trials in both dark and visible light conditions, using uncoated-$C_{100}S_{100}$, uncoated-$C_{85}S_{85}$, and simple-TiO_2 cementitious samples (detailed description in section 3.2.1.3.). The uncoated-$C_{100}S_{100}$ and uncoated-$C_{85}S_{85}$ cementitious specimens were used to study the impact of adsorption and Fe on bacterial inactivation, respectively. On the other hand, simple

TiO_2 cementitious samples were utilized to detect the effect of pure TiO_2 on the inactivation of bacteria. The initial bacterial count following each experiment was estimated by measuring the bacteria count on the uncoated-$C_{100}S_{100}$ cementitious specimen positioned adjacent to the targeted specimen. Table 3.11 summarizes various boundary conditions, along with remarks on their assessment.

Table 3.11 Various boundary conditions along with the objective remarks on their assessment.

S.No.	Boundary Condition	Luminous Condition	Remark
1.	Control + Uncoated * *Control = cement + sand*	Dark	Effect of light and adsorption
2.		Light	
3.	Substitution + Uncoated **Substitution = cement + sand + Fe rich waste*	Dark	Effect of Fe^{3+}
4.		Light	
5.	Control: TiO_2 coated vs Control + Uncoated * *Control: TiO_2 coated = TiO_2 + cement + sand*	Dark	TiO_2 effect
6.		Light	
7.	Substitution: TiO_2 coated vs Control +Uncoated * *Substitution: TiO_2 coated = Fe + TiO_2 + cement + sand*.	Dark	Surface-active Fe_2TiO_5 heterojunction effect
8.		Light	

3.3.4 Photo-Disinfection Kinetics

An empirical first-order kinetics model was employed to analyze the photocatalysis process of the Fe_2TiO_5 heterostructure composite, as depicted in equation 3.11. The slope of the natural logarithm (A_x/A_0) vs time for bacterial inactivation yields the rate constant k, where "k" is the pseudo-first-order rate constant (min^{-1}). The initial cell count of the bacteria is denoted as A_0 at time t=0, and A_x represents the bacterial cell count at any given time "x". The terms used for initial and final concentration may vary from $A_0 \approx A_i$ and $A_t \approx A_f$, although the concept remains unchanged, such that,

$$\ln \frac{A_x}{A_1} = kx \qquad 3.11$$

3.3.5 Statistical Analysis and Mathematical Models

The efficiency of different boundary conditions was assessed using Origin 2016. All experiments were conducted in triplicate, and the results are presented as the average of the three tests, with error bars indicating the standard deviation.

3.3.5.1 Mathematical Inactivation Models

The present study employed several mathematical inactivation models, including log-linear, Weibull, double Weibull, and biphasic models. These models' kinetic coefficients were derived by using non-linear regression methods, wherein the experimental findings were adjusted to the respective equations. This intricate procedure, which is based on the least squares technique, is made significantly more straightforward by using the Microsoft Excel program: Solver and GInaFiT (Geeraerd and Van Impe Inactivation Fitting Tool []), which was initially developed by Geeraerd et al. at the Catholic University of Leuven (Belgium). The fitting adequacy of the inactivation outcomes was evaluated using two fitting metrics: the coefficient of determination (R^2) and root mean square deviation (RMSD). Furthermore, including a graphical representation that compares the experimentally acquired findings with those anticipated by mathematical models offers valuable insights into the accuracy and suitability of the employed model. Also, the statistical software GInaFiT was utilized to compute the standard errors associated with various kinetic parameters. Only fits that exhibited $R^2 > 0.90$ and a low standard error were considered in this research study.

Log-Linear Model

The log-linear model, often known as the Chick-Watson model, is an improved version of the previously established Chick model. The model mentioned above regulates the stoichiometric correlation between the number of inactivated microbes and the number of disinfectant molecules [334], [335]. The log-linear model is defined by equation 3.12:

$$\mathbf{Log}\frac{\mathbf{A_t}}{\mathbf{A_o}} = -\mathbf{K.C.t} \rightarrow \mathbf{Log}\frac{\mathbf{A_t}}{\mathbf{A_o}} = -\mathbf{k_{ap}.t} \qquad \mathbf{3.12}$$

Here, A_0 and A_t represent the initial and final microbial concentrations. The variable "k" represents the first-order rate constant (min^{-1}), "C" denotes the concentration of the disinfectant,

and "t" serves as the reaction time. According to reference [39], the integration of disinfectant concentration may be achieved by using an apparent rate constant, hence simplifying the model.

Weibull Model

The Weibull inactivation model has its foundation on a continuous probability distribution [336]. This model defines the extent of variability in a system's behavior. In first-order models, microbial populations are presumed to be uniform in their resistance to external circumstances. The Weibull model characterizes the microbial population as diverse. The mortality of cells is contingent upon the duration of exposure to external stresses, with each cell requiring a distinct exposure time to collapse. Also, a Weibull distribution governs the resistance to dispersal under varying conditions. The Weibull model for bacterial deactivation is a cumulative representation of an asymmetric probability density function concerning the thermal resistance of individual bacterial cells. The Weibull model is expressed by equation 3.13.

$$Log\ \frac{A_t}{A_o} = -\left(\frac{t}{\delta}\right)^p \qquad \textbf{3.13}$$

The initial decimal reduction time, defined as the duration necessary to achieve the first decimal logarithmic reduction in the bacterial population (e.g., from A_0 to $A_0/10$), is represented by δ. The equation's shape is defined by p. When $p>1$, the shape is convex; when $p<1$, its shape is concave. At $p = 1$, the equation represents a linear first-order model.

Double Weibull Model

The double Weibull model is a computational model that has been derived from the Weibull model originally proposed by Coroller et. al. (2006) [337]. The fundamental theory of this model suggests that the microbial population could be divided into two distinct sub-population categories, each exhibiting varying degrees of resilience to external stresses. It is postulated that the resistance shown by each subpopulation category corresponds to the Weibull distribution. The provided expression is denoted as equation 3.14.

$$\mathbf{A} = \frac{\mathbf{A_0}}{(\mathbf{1+10^{\alpha}})}\left(\mathbf{10}^{-\left(\frac{t}{\delta_1}\right)^{p_1+\alpha}} + \mathbf{10}^{-\left(\frac{t}{\delta_2}\right)^{p_2}}\right) \qquad \textbf{3.14}$$

Here, the variable α represents the subpopulation fraction inside the population, whereas subscripts 1 and 2 denote distinct subpopulations. Furthermore, the variable p represents the shape parameter, t represents time, and δ represents the first decimal reduction in the treatment time. Subpopulation 1 has a higher degree of sensitivity to stress than Subpopulation 2 ($\delta_1 < \delta_2$).

Biphasic Model

Cerf (1977) [338] introduced a kinetic model referred to as the biphasic model, which focuses on the theory of two fractions. The underlying assumption of this model is that the microbial population can be divided into two distinct sub-population categories, each exhibiting a different degree of sensitivity to the treatment. The biphasic model is represented by equation 3.15.

$$\boldsymbol{Log\frac{A_t}{A_o} = log\left[f.e^{-k_1.t} + (1-f).e^{-k_2.t}\right]} \qquad \textbf{3.15}$$

In this context, f represents the proportion of microorganisms that have explicitly survived within sub-population group 1, whereas (1 – f) denotes the proportion of microorganisms that have survived within sub-population group 2. The kinetic constant of the sensitive microbial population is denoted as k_1, whereas the kinetic constant of the more resistant microbial population is represented as k_2.

3.3.6 Durability Study and Cost Analysis

The durability and recyclability of the Fe_2TiO_5 heterostructure composite are vital factors for the scalability of the current technology. The present research provided a considerably more challenging set of circumstances due to integrating two techniques, namely photocatalysis and sustainable construction, into a single system. The primary challenge was sustaining the reuse and recyclability of the catalyst, even in adverse environments. Because the coating on the cementitious material may fail to stabilize under adverse environmental conditions. In the photo-disinfection process, the cementitious composite must support the TiO_2 layer applied to its outer surface while preserving the durability of the cementitious construction material. Analytical investigation such as SEM-EDS, XRD, UV-DRS and FTIR were used to evaluate the Fe_2TiO_5 heterostructure composite that has been recycled more than 45 times to test the support material's durability and ability to execute the in-situ heterojunction production concept. The efficiency of

the Fe_2TiO_5 heterostructure in disinfecting *E. coli* bioaerosols over these cycles was also assessed.

The cost of raw materials like cement, sand, and photocatalysts must be considered while determining the Fe_2TiO_5 heterostructure composite's economic viability. Evaluating costs at the lab scale provides a preliminary assessment of the feasibility of the heterostructure composite for potential larger-scale implementations. The overall expense of the system was assessed for 45 recycling figures, such that basic arithmetic principles were utilized for the calculations involved.

3.4 Nomenclature for the Different Catalyst Support

Table 3.12 presents a comprehensive list of various supports and their corresponding names utilized in different sections of the study.

Table 3.12 Terminology defined for various catalyst support throughout the study.

Terminology	**Description**
FA	Fly Ash
FS	Foundry Sand
BS	Blast Furnace Sand
IWPs (Iron-rich Industrial waste products)	FA + FS + BS
OPC	Ordinary Portland cement
TiO_2	Titanium Dioxide
Fe	Iron
Fe_2O_3	Ferric Oxide
Fe_2TiO_5 (Iron-titanium heterojunction oxide)	Fe_2O_3 + TiO_2
Fe_2TiO_5 heterostructure for cementitious composite	OPC + IWPs + River sand + TiO_2
Uncoated $C_{100}S_{100}$ cementitious sample	OPC + River sand
Uncoated $C_{85}S_{85}$ cementitious sample	OPC + IWPs + River sand
Simple TiO_2 cementitious sample	OPC + River sand + TiO_2

Chapter 4

Results and Discussion

General

This chapter has three objective-oriented sections: A, B, and C. Section A examines the strength and durability of iron-rich cementitious mortar through various testing methods. Section B evaluates the novelty of the developed Fe_2TiO_5 heterostructure for cementitious composites, focusing on analytical, photocatalytic, and antibacterial properties evaluation. Section C evaluates the antimicrobial efficacy of the Fe_2TiO_5 heterostructure in neutralizing *E.coli* bioaerosols under visible light irradiation through a series of disinfection experiments. The proposed process and section organization are shown in Figure 3.1.

4.1 Section A: Fabrication of Iron-Rich Cementitious Mortar

4.1.1 Fresh State Properties

Fresh properties are related to the workability of cement mortar, indicating the ease of mortar placement. The workability of sustainable cementitious mixtures was assessed through slump and fresh density testing.

4.1.1.1 Slump Test

The slump test was conducted on fresh cementitious mortar mixtures with different amounts of IWP replacement, and the findings are illustrated in Figure 4.1. The results demonstrate that the slump value of the IWPs-modified mortar mixes increased with increasing BS replacement levels, indicating enhanced workability and cohesiveness attributed to reduce water demand. This improvement corresponds with prior research indicating improved workability in BS-based mortar mixtures [339]. The observed result can be ascribed to the smooth and dense surface texture of BS particles, which exhibit lower water absorption relative to PC [340].

Despite the increasing trend in slump values for IWPs-modified mixes, these values remained lower than the control mix $C_{100}S_{100}$, which achieved a slump value of 120 mm. The slump values for design mixes from $C_{85}S_{85}$ to $C_{60}S_{85}$ varied from 100 to 107 mm, representing approx. 80–87% of the reference $C_{100}S_{100}$ mix. This decrement in workability is mainly associated with the

inclusion of FA in the IWPs-modified mixtures. Although numerous studies indicate that FA enhances mortar workability owing to its spherical morphology and ball-bearing effect [341], this study proposes a slight reduction in workability, potentially attributed to the irregular shape and porous characteristics of certain FA particles. Seifan et al. (2021) [342] and Gholampour et al. (2021) [343] reported analogous findings, noting a decrease in workability in FA-based mortar mixes relative to control mixes.

The observed slump behavior of IWPs-modified cementitious mortar results from the synergistic influence of FA and BS particles. Previous research have documented similar patterns, indicating that slump values diminished with a higher proportion of limestone and sugarcane bagasse ash [344], as well as corn cob ash and glass powder [345], utilized as binary cementitious materials in concrete.

4.1.1.2 Fresh Density

Figure 4.1 presents the fresh density results for different IWPs-modified cementitious mortar mixes. The results indicate that the fresh density of the different IWPs-modified mortar mixes decreases with increasing BS content. The reference mix $C_{100}S_{100}$ achieved a fresh density of 2275 kg/m^3, while the IWPs-modified mix design reached 99% ($C_{85}S_{85}$), 97% ($C_{80}S_{85}$), 89% ($C_{75}S_{85}$), 76% ($C_{70}S_{85}$), 61% ($C_{65}S_{85}$), and 49% ($C_{60}S_{85}$) of the fresh density of the reference $C_{100}S_{100}$ mix. The mix $C_{85}S_{85}$ demonstrated a fresh density of 2274 kg/m^3, which is nearly identical to the reference $C_{100}S_{100}$ mix. The observed reduction in the fresh density of other IWPs-modified mortar can be attributed to the inherent lower density of the SCMs (FA and BS) and the pores and interfaces introduced by the SCMs within the mortar's structure. This is subsequently demonstrated through SEM analysis (section 4.1.5.1). Gholampour et al. (2021) [343] reported similar findings, stating that concretes containing FA, BS, and FS displayed densities almost identical to those of the control mixes. The mixes $FS_{50}BS_{35}$ (having 50% FS and 35% BS), $FS_{50}BS_{70}$ (having 50% FS and 70% BS), $FS_{50}FA_{23}G_{47}$ (having 50% FS, 23% FA and 47% BS), and $FS_{50}FA_{35}$ (having 50% FS and 35% FA) achieved fresh density values of 2378 kg/m^3, 2350 kg/m^3, 2390 kg/m^3, and 2381 kg/m^3, respectively, when compared to the control mix, which had a density of 2386 kg/m^3.

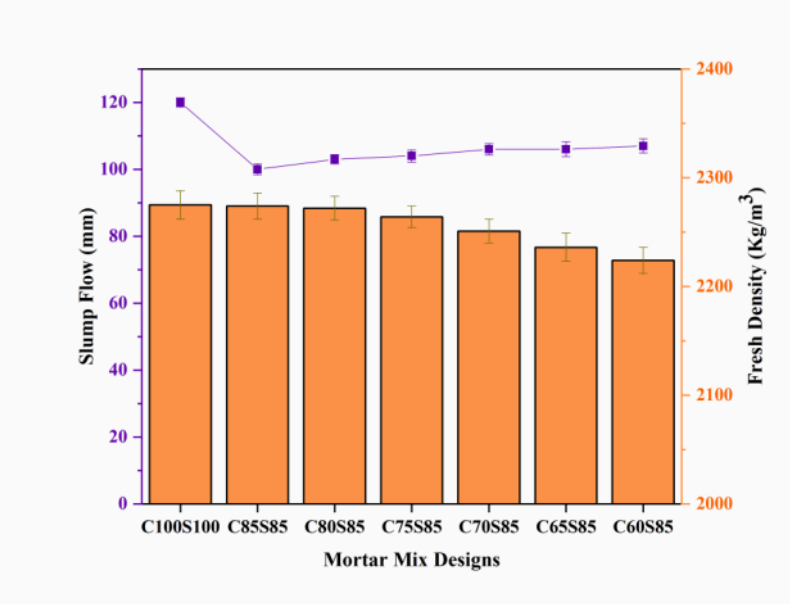

Figure 4.1 The fresh state properties conducted on fresh cementitious mortar mixes with different IWPs-replacement levels.

4.1.2 Strength Properties

The hardened mortar's strength is a critical factor in evaluating the structural performance of a cementitious material, such that, each strength property is essential in determining the mortar's overall performance in building applications and is directly linked to its durability. The strength characteristics of sustainable iron-rich cementitious mixes were evaluated through compressive strength, flexural strength, and split tensile strength, respectively.

4.1.2.1 Compressive Strength

The compressive strength of hardened mortar specimens was assessed at 7, 28, and 56 days, as illustrated in Figure 4.2. The testing of each mix involved three specimens, with the reported values reflecting the average of these measurements. The findings reveal a gradual enhancement in strength correlated with an increased curing period, emphasizing the long-term pozzolanic efficacy of FA and BS in IWPs-modified mixtures. The $C_{85}S_{85}$ mix demonstrated superior compressive strength across all curing ages compared to other IWPs-modified mixes.

At 7 days of curing, the compressive strength of the reference mix $C_{100}S_{100}$ was measured as 27.4 N/mm². The data indicates a reduction in early-age strength corresponding to higher levels of BS substitution, with recorded compressive strengths of 26.2, 24.2, 19.9, 18.7, 18.2, and 17.9 N/mm² for mixes $C_{85}S_{85}$ to $C_{60}S_{85}$, respectively. The decrease in early-age strength, which varies from 4.4% to 35% compared to the control mix, can be linked to the lower hydraulic reactivity of FA and BS. The presence of an activator, like calcium hydroxide ($Ca(OH)_2$), is essential for improving the pozzolanic reactivity of these materials during the initial curing phases [346]. Research has indicated comparable patterns [347], validating that incorporating FA and BS hinders early-age strength development related to their slower hydration kinetics relative to OPC.

The hydration reaction of OPC is given by:

$$\boldsymbol{Cement\ (C_3S + C_2S)\ +\ H_2O\ (H)\ \rightarrow CSH\ gel\ + Ca(OH)_2\ (CH)} \qquad \textbf{4.1}$$

The pozzolanic reaction involving FA and BS occurs as follows:

$$\boldsymbol{Ca(OH)_2\ (CH)\ + SiO_2\ (S)\ +\ H_2O\ (H)\ \rightarrow CSH\ gel} \qquad \textbf{4.2}$$

This delayed pozzolanic reaction accounts for the lower early-age strength in FA- and BS-modified mixes. As curing expands, the continual reaction improves the microstructure, gradually increasing strength over time [348].

After 28 days of curing, there was a notable enhancement in the compressive strength of all mixes, attributed to the continuous hydration and pozzolanic reactions taking place. The $C_{85}S_{85}$ mix demonstrated strength of 36.2 N/mm², indicating a 4.9% increment compared to the reference $C_{100}S_{100}$ mix, which recorded strength of 34.55 N/mm². The compressive strengths for mixes $C_{80}S_{85}$ to $C_{60}S_{85}$ were measured at 33.4, 27.1, 24.4, 23.0, and 20.9 N/mm², respectively. The strength values for these mixes have been obtained at 98.8%, 92.5%, 90%, 88.5%, and 86.5% of the reference mix. This trend is consistent with earlier research [349], which concluded that higher FA and BS content contributes to improved long-term strength development by generating additional CSH gel. Similarly, Gholampour et al. (2021) [343] observed an 11% increase in 28-day strength with the inclusion of 23% FA, 47% BS, and 50% FS in mortar mixes. The findings indicate that an effectively optimized mix, like $C_{85}S_{85}$, demonstrates enhanced strength performance compared to traditional cementitious materials.

At 56 days, the strength gain persisted, with the $C_{85}S_{85}$ mix achieving a compressive strength of 50.8 N/mm², reflecting a 9.7% increase compared to the reference mix $C_{100}S_{100}$, which recorded 46.3 N/mm². The strength values for mixes $C_{80}S_{85}$ to $C_{60}S_{85}$ were recorded as 45.1, 40.4, 37.2, 36.6, and 31.3 N/mm², which represent 98.8%, 94.1%, 91%, 90.3%, and 85% of the reference mix, respectively. The extended strength improvement in FA- and BS- modified mixes is due to the ongoing pozzolanic reaction, which refines the pore structure and boosts matrix densification [348]. Nedunuri et al. (2020) [350] reported comparable findings, noting that OPC samples initially surpassed FA- and BS-modified mixes at 7 days yet demonstrated reduced strength gains in the later curing stages. It was observed that a 20% FA substitution led to strength increases of 6% and 15% at 28 and 56 days, respectively, while a 22% BS replacement resulted in strength gains of 11% and 17.6%, respectively.

The results indicate that well-designed FA- and BS- modified cementitious mixtures can attain strength properties comparable to or better than conventional mortar. The observed trends are confirmed by SEM analysis (section 4.1.5.1), which demonstrates refined pore structures and improved microstructural integrity in optimized mix designs. The findings promote the viability of industrial by-products as sustainable substitutes for cementitious materials in construction applications.

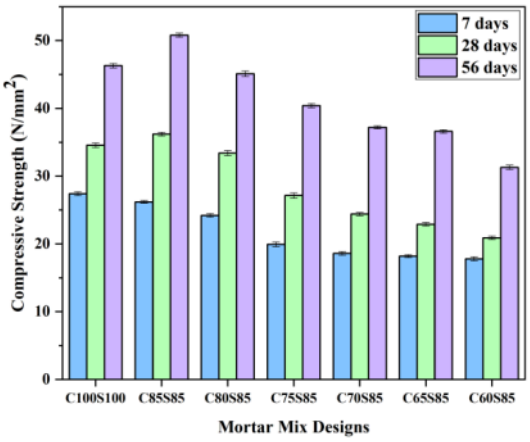

Figure 4.2 The compressive strength results of hardened mortar specimens at 7, 28, and 56 days, respectively.

4.1.2.2 Split Tensile Strength

Figure 4.3 illustrates the splitting tensile strength of IWPs-modified cementitious mortar specimens at 7 and 28 days, serving as an indirect measure of tensile performance. The results demonstrate a significant variation in tensile strength corresponding to varying levels of BS replacement. At an optimal 5% BS replacement ($C_{85}S_{85}$ mix), the tensile strength exceeded that of the reference mix ($C_{100}S_{100}$), followed by a decrease in the tensile strength in the subsequent mixes ($C_{80}S_{85}$ to $C_{60}S_{85}$).

After 7 days of curing, the reference mix ($C_{100}S_{100}$) demonstrated a split tensile strength of 1.91 N/mm^2. The $C_{85}S_{85}$ mix exhibited a slight improvement in strength, reaching 1.98 N/mm^2, which corresponds to a 3.7% increase compared to the reference mix. The recorded strength values for $C_{80}S_{85}$, $C_{75}S_{85}$, $C_{70}S_{85}$, $C_{65}S_{85}$, and $C_{60}S_{85}$ are 1.89 N/mm^2, 1.83 N/mm^2, 1.81 N/mm^2, 1.76 N/mm^2, and 1.76 N/mm^2, respectively. Notably, all these values are below the reference mix. This trend corresponds with the findings on compressive strength, indicating that early-age strength development was restricted by the slow pozzolanic reaction of BS and the diminished hydration rates in IWPs-modified mixes.

After 28 days, the tensile strength of the mortar specimens showed significant improvement. The reference mix achieved strength of 3.1 N/mm^2, whereas the $C_{85}S_{85}$ mix demonstrated a maximum strength of 3.8 N/mm^2, indicating a 22.6% improvement compared to the reference mix. The remaining mixes ($C_{80}S_{85}$ to $C_{60}S_{85}$) demonstrated tensile strengths of 3.0 N/mm^2, 2.6 N/mm^2, 2.5 N/mm^2, 2.3 N/mm^2, and 2.2 N/mm^2, respectively. The decline in tensile strength as BS content surpasses 5% aligns with the compressive strength results, demonstrating a comparable pattern attributed to the dilution of cementitious material and diminished early-age bonding properties.

The findings correspond with earlier research, such as, Kim et al. (2013) [351], which indicated a decline in split tensile strength as BS replacement increased; however, no notable reduction was observed for substitutions up to 10%. Similarly, Huynh et al. (2022) [352] found that the 28-day split tensile strength of concrete increased with the addition of BS, but this improvement was only observed up to a certain optimal level, after which a decline in strength occurred. Further research [353] indicates that excessive BS replacement lowers tensile strength over time, attributed to decreased cementitious material and compromised interfacial transition zones.

The results suggest that the IWP modification does not substantially impact the development of tensile strength at early ages, indicating that prolonged curing is necessary for optimal performance. The observed enhancement in strength during the later stages can be linked to increased pozzolanic activity, which facilitates ongoing pore refinement and matrix densification, as evidenced by the compressive strength results.

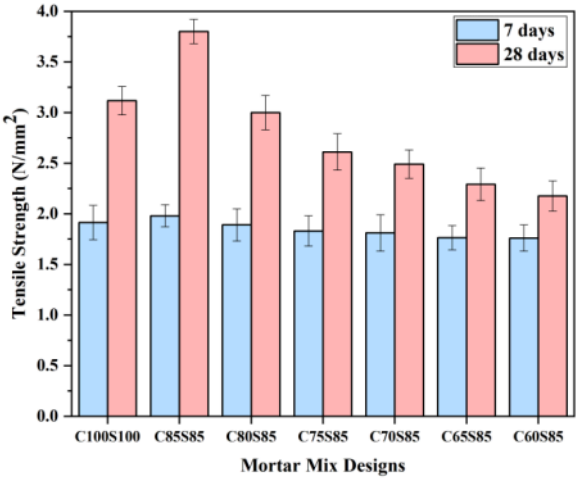

Figure 4.3 The split tensile strength of IWPs-modified cementitious mortar specimens at 7 and 28 days, respectively.

4.1.2.3 Flexural Strength

Figure 4.4 illustrates the flexural strength outcomes of IWPs-modified cementitious mortar specimens after 7 and 28 days of curing. The findings demonstrate that the flexural strength shows a progressive increase up to a 5% BS replacement level, with the $C_{85}S_{85}$ mix attaining the most noticeable improvement relative to the reference mix $C_{100}S_{100}$. Exceeding this threshold, the additional substitution of BS leads to a reduction in flexural strength, a pattern that corresponds with the previously mentioned results for compressive and splitting tensile strength.

After 7 days of curing, the $C_{85}S_{85}$ mix exhibited a flexural strength of 3.58 N/mm², indicating a slight improvement compared to the reference mix, which recorded strength of 3.66 N/mm². However, the subsequent rise in BS content resulted in a decrease in flexural strength. The flexural strength values recorded for mixes $C_{80}S_{85}$ to $C_{60}S_{85}$ are as follows: 3.44 N/mm², 3.13

N/mm^2, 3.03 N/mm^2, 2.99 N/mm^2, and 2.96 N/mm^2, respectively. The observed trend suggests that increased levels of BS substitution lead to a decrease in early-age flexural strength attributed to the delayed pozzolanic reaction of BS. The reduction in flexural strength observed at early curing age aligns with the compressive and split tensile strength results, both of which demonstrated decrement as BS replacement increased.

Following a 28-day curing period, a notable enhancement in flexural strength was recorded in all mixes. The $C_{85}S_{85}$ mix achieved the highest flexural strength at 4.69 N/mm^2, reflecting a 14.11% improvement over the reference mix, which measured 4.11 N/mm^2. The values obtained for $C_{80}S_{85}$, $C_{75}S_{85}$, $C_{70}S_{85}$, $C_{65}S_{85}$, and $C_{60}S_{85}$ are 4.05 N/mm^2, 3.65 N/mm^2, 3.45 N/mm^2, 3.36 N/mm^2, and 3.20 N/mm^2, respectively. The observed reductions in flexural strength at higher BS replacement levels are obvious; however, they are not as significant compared to the reductions in compressive strength at similar replacement levels. This observation indicates that flexural strength exhibits a lower sensitivity to BS replacement than compressive strength, thereby emphasizing the importance of prolonged curing for strength development in BS-modified mortar.

Prior research has indicated comparable patterns concerning the influence of BS on flexural strength. Ramakrishnan et al. (2017) [354] noted that substituting 10% BS led to a corresponding 10% enhancement in the 28-day flexural strength compared to the reference mix. Siddique et al. (2014) [355] demonstrated that the flexural strength of concrete increases with iron waste content up to 12%, beyond which a decline is observed. Bheel et al. (2020) [356] observed that binary cementitious material (BCM) mixtures, which included BS and metakaolin (MK) as partial cement replacements, demonstrated the most significant enhancements in flexural strength at a 10% replacement level, showing increases of 9.93% and 10.20% at 28 and 56 days, respectively. In conclusion, the $C_{85}S_{85}$ mix design demonstrates the highest flexural strength performance, with recorded values of 3.58 N/mm^2 and 4.69 N/mm^2 at 7 and 28 days, respectively. This observation is consistent with the trends in compressive and splitting tensile strength, thereby reinforcing the optimal BS replacement level for improving the mechanical properties of IWPs-modified mortar.

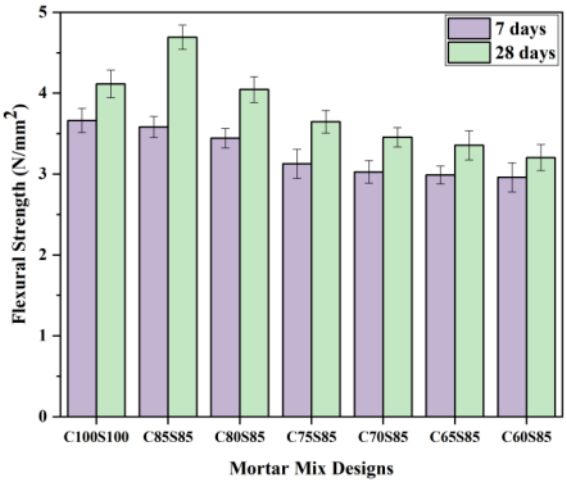

Figure 4.4 The flexural strength results of IWPs-modified cementitious mortar specimens at 7 and 28 days of curing period.

4.1.3 Physical Properties

The physical characteristics of hardened cementitious specimens serve as vital indicators of their suitability, durability, and performance in several construction applications. Each physical property is crucial in assessing the material's long-term durability and resistance against external stresses. The present study evaluated the open porosity, real, bulk and dry bulk density to assess the physical characteristics of IWPs-modified cementitious mixes.

4.1.3.1 Open Porosity

Figure 4.5 presents the porosity results of IWPs-modified cementitious mortar specimens after a curing period of 28 days. The data indicate a clear trend in porosity variation with increasing BS replacement levels. The reference mix $C_{100}S_{100}$ showed a porosity of 16.31%. The addition of IWPs led to a reduction in porosity up to 5% BS replacement ($C_{85}S_{85}$), after which a gradual increase was noted. The data indicates that $C_{85}S_{85}$ exhibited the lowest porosity at 15.79%. This was succeeded by $C_{80}S_{85}$ with a porosity of 16.39%, followed by $C_{75}S_{85}$ (17.69%), $C_{70}S_{85}$ (18.68%), and $C_{65}S_{85}$ (18.17%). The highest porosity was observed in $C_{60}S_{85}$, which measured 19.25%.

The results are consistent with existing literature, including the research conducted by Nedunuri et al. (2020) [350], which indicated an increase in porosity from 15.48% to 17.65% as the levels of BS replacement increased from 22% to 44%. The differences in porosity can be explained by the influence of BS and FA on the microstructural properties of the cementitious matrix. The decrease in porosity observed at 5% BS replacement ($C_{85}S_{85}$) suggests that this level of BS provides the most effective pozzolanic effect, resulting in better matrix densification through increased secondary hydration reactions. As the BS content surpasses 5%, the dilution effect becomes increasingly significant, increasing overall porosity.

The hydration mechanism of cement entails the generation of hydrated lime ($Ca(OH)_2$) as a key product, which then interacts with pozzolanic materials in the presence of moisture to produce further calcium silicate hydrate (C-S-H) gel [357]. This reaction is essential in optimizing the pore structure by minimizing the size and interconnectivity of capillary pores. However, the rate of pozzolanic reaction is influenced by the fineness and reactivity of the pozzolanic material [358]. Since the slow pozzolanic activity of BS and FA in a minimal pore-filling effect during the early curing stages [359]. At 28 days, the hydration process evolves, resulting in alterations to the distribution of pore sizes, their shapes, continuity, and tortuosity [360]. Thus, the ongoing enhancement of pore structure at later curing ages can be linked to the generation of supplementary C-S-H gel, which occupies voids and consequently diminishes total porosity.

The determined porosity trends are directly related to the compressive strength outcomes of IWPs-modified cementitious mortar specimens. The earlier analysis indicates that the $C_{85}S_{85}$ mix displayed enhanced compressive strength, correlating with its minimal porosity levels. The documented inverse relationship between porosity and compressive strength in cementitious systems suggests that a denser microstructure correlates with enhanced mechanical performance. The microstructural insights from SEM analysis (section 4.1.5.1) support this trend, showing a more compact and homogeneous matrix for the $C_{85}S_{85}$ mix. In contrast, higher BS replacement levels displayed increased pore interconnectivity and micro-crack formation, leading to decreased mechanical strength.

Thus, the porosity analysis confirms that the $C_{85}S_{85}$ mix exhibits enhanced performance regarding mechanical properties and microstructural densification. The equilibrium between the pozzolanic reaction and the dilution effect establishes the ideal replacement level, with 5% BS

yielding the most favorable results. Exceeding this 5% threshold, results in an increase in porosity, which undermine the strength and durability of the cementitious matrix.

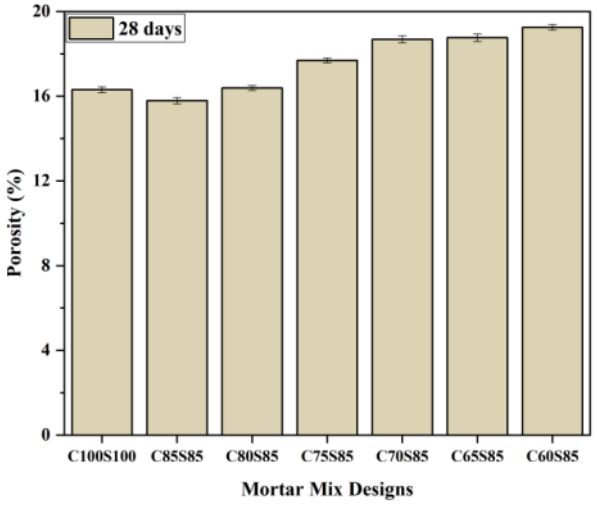

Figure 4.5 The 28-day porosity results for the IWPs-modified design mixes.

4.1.3.2 Real, Bulk and Dry Density

Figures 4.6 and 4.7 illustrate the 28-day real, bulk, and dry densities of the mixes modified with IWPs. The results demonstrate a decreasing trend in all density parameters with increasing BS replacement while remaining within the range of 2000–2500 kg/m^3, confirming their classification as standard cementitious materials [361]. The bulk density declined from 2811 kg/m^3 (reference $C_{100}S_{100}$ mix) to 2380 kg/m^3 ($C_{60}S_{85}$), indicating reductions of 16.1%, 10.3%, 13.1%, 13.6%, 15.3%, and 15.3% for mixes $C_{85}S_{85}$ to $C_{60}S_{85}$, respectively. Similarly , the real density exhibited a decline from 2365 kg/m^3 (reference mix) to 1946 kg/m^3 ($C_{60}S_{85}$), reflecting reductions of 13.3%, 15.6%, 15.8%, 16.5%, 17.7%, and 17.7% for $C_{85}S_{85}$ to $C_{60}S_{85}$ mixes, respectively. The dry bulk density displayed a comparable pattern, declining from 2215 kg/m^3 (reference mix) to 2029 kg/m^3, indicating reductions of 3.6%, 4%, 4.7%, 7.5%, 8.3%, and 8.5% for mixes $C_{85}S_{85}$ to $C_{60}S_{85}$, respectively.

The observed density variations result from the inclusion of FA and BS, which have a lower specific gravity compared to cement, thus reducing the overall density. Moreover, variations in

compaction levels had a significant impact on the observed density trends. The decrease in density corresponds with the findings on compressive and tensile strength, indicating that a reduction in strength at elevated BS replacement levels is associated with increased porosity and decreased material density.

Comparable trends have been documented in the literature. Phul et al. (2019) [362] noted a reduction in mortar density as the FA content increased, with conventional mortar density (2.42 g/cm³) decreasing to 2.29 g/cm³ at elevated FA replacement levels. Research conducted by Mangi et al. (2022) [363] has shown a decrease in concrete density corresponding to higher levels of marble and tile powder, along with wood waste ash. Akçaözoglu et al. (2011) [364] demonstrated that replacing cement with FA and BS led to lower bulk and dry densities, achieving reductions of up to 7% when compared to reference mixes. Thus, the current study demonstrates that the density reductions in IWPs-modified mixes fall within acceptable limits for structural applications, thereby affirming their potential as lightweight construction materials that enhance sustainability.

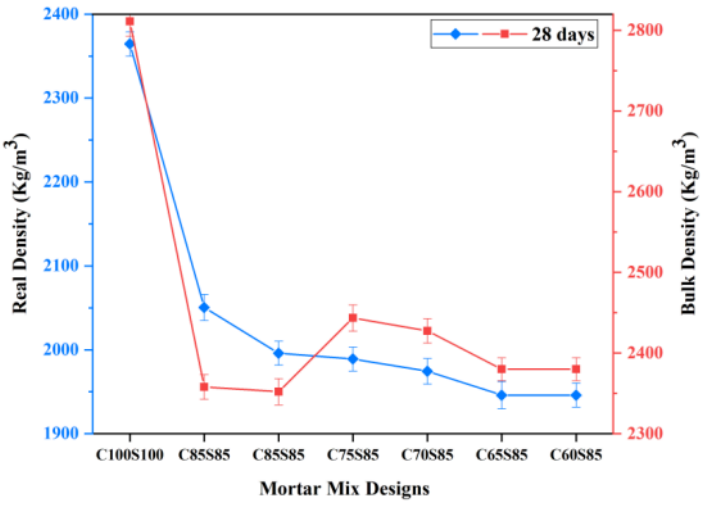

Figure 4.6 The 28-day real and bulk density for different IWPs-modified design mixes.

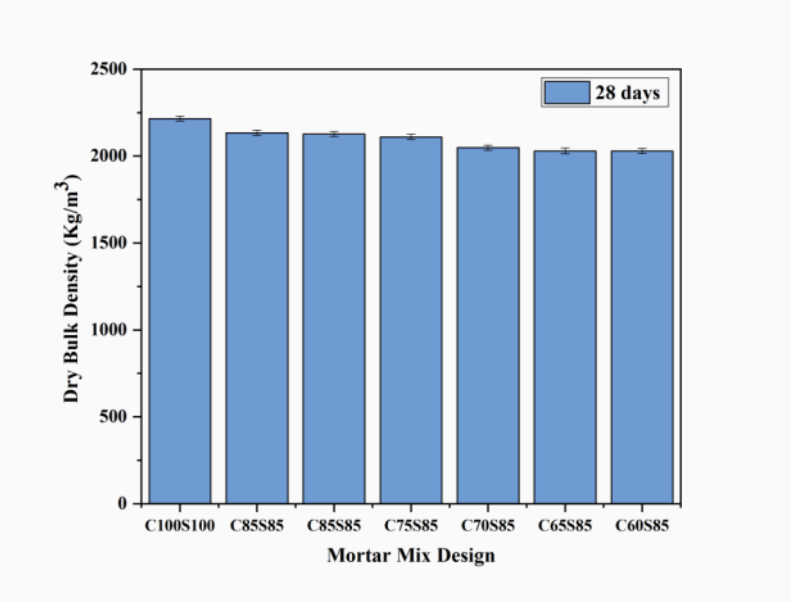

Figure 4.7 The 28 day dry bulk density of the IWPs-modified cementitious mortar specimens.

4.1.4 Durability Properties

To evaluate the structural integrity of cementitious mortar, durability is a crucial factor in addition to strength and reliability. It provides an indication of the duration for which the cementitious structure remains functional and the maintenance necessary to sustain its serviceability. The present study evaluated it using waste absorption by immersion property.

4.1.4.1 Water Absorption By Immersion

Figure 4.8 illustrates the 28-day water absorption by immersion capacity of IWPs-modified mixes. The findings reveal a progressive trend in water absorption corresponding to higher BS substitution levels, except a slight decline observed at 5% BS replacement ($C_{85}S_{85}$). The measured water absorption values varied between 5.84% for C85S85 and 7.98% for C60S85, with the reference mix ($C_{100}S_{100}$) showing a value of 6.30%.

The trend in water absorption corresponds with the previously discussed porosity results, highlighting the relationship between pore structure and water ingress. The elevated water absorption observed in mixes with higher BS replacement can be explained by increased porosity

and a prolonged hydration process, which hinders the densification of the microstructure. The increased void content promotes water penetration, aligning with findings from previous studies [365]. Kim et al. (2013) [351] observed that including BS and furnace bottom ash in concrete resulted in higher water absorption ratios.

Furthermore, existing literature suggests that increased water absorption negatively impacts compressive strength [366], a correlation demonstrated in this study. The decrease in compressive strength of IWPs-modified mixes aligns with their increased water absorption values, thereby reinforcing the microstructural observations (SEM analysis). Among the various mix designs, $C_{85}S_{85}$ exhibits the most balanced performance, with a minimal 7.3% reduction in water absorption compared to the reference mix, making it the optimal choice for durability and mechanical integrity.

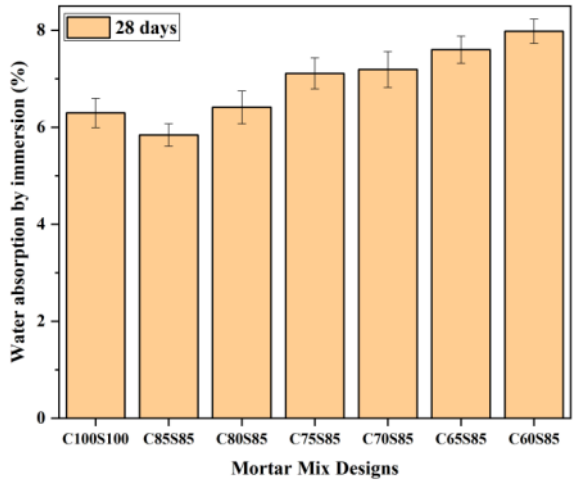

Figure 4.8 The 28-day water absorption by immersion capacity of IWPs-modified design mixes.

4.1.5 Microstructure Analysis

The microstructural examination of the iron-rich cementitious mortar specimen was conducted using SEM-EDS, XRD and TGA/DTA analysis to thoroughly assess the physicochemical and

mineralogical changes resulting from the integration of IWPs (FA, BS, and FS) within the complex cementitious matrix.

4.1.5.1 SEM with EDS Analysis

Figure 4.9 to 4.12 provides scanning electron micrographs of different IWPs-modified cementitious mortar specimens at the curing age of 28 and 56 days, respectively. The results demonstrated that at both curing ages, the OPC and IWPs (FA, BS, and FS) particles were converted into hydration products as a result of a successful hydration reaction (Figure 4.10).

The 28-day SEM micrographs of the reference $C_{100}S_{100}$ mix design (Figure 4.9) exhibited a densely packed microstructure characterized by the presence of needle-like ettringite (E), resulting from the initial hydration process [367]. Additionally, flaky-shaped crystals of calcium hydroxide (CH), also referred to as Portlandite (P), and C-S-H gel were observed, which are the primary strength-generating components responsible for the binding and strengthening properties of the mix during the initial curing days [368]. At 56 days, denser and more compact microstructure of reference $C_{100}S_{100}$ was observed, with the surface of the $C_{100}S_{100}$ mortar mix almost entirely covered by C-S-H gel.

In a similar manner, the mix $C_{85}S_{85}$, having a 5% BS replacement level, demonstrates the formation of calcium carbonate (CC) also referred to as Calcite, uniformly distributed throughout the micrograph (Figure 4.10a) at a curing age of 28 days. Over time, it was observed that the majority of pore voids were occupied by C-S-H gel, leading to a compact and dense microstructure, which substantially improved the strength and durability of the cementitious mix $C_{85}S_{85}$ at 56 days. These observations aligned with the compressive strength development of the $C_{85}S_{85}$ mix design relative to the reference $C_{100}S_{100}$ mix. The findings consistent with the above results were reported by [369]–[371].

Figures 4.10b to 4.12 illustrate the SEM micrographs of the mix design ranging from $C_{80}S_{85}$ to $C_{60}S_{85}$, such that, at 28 days, the IWPs-modified mix ($C_{80}S_{85}$ to $C_{60}S_{85}$) showed voids and micro-cracks. Needle-shaped ettringites were also observed during the initial curing stages, extending up to 28 days (refer to Figure 4.10b to 4.12). The formation of uneven CSH layers was notably evident in these mix designs ($C_{80}S_{85}$ to $C_{60}S_{85}$). Thus, the reduction in compressive strength of IWPs-modified mix designs with varying replacement levels of BS at the 28-day curing period

can be attributed to the differences in microstructure compared to the reference $C_{100}S_{100}$ mix (Figure 4.9). With an increase in curing age to 56 days, dense and homogeneous layers of CSH became evident, along with a greater presence of ettringites. This contributed to an improved structure, with FA and BS addressing voids and cracks, thereby enhancing the strength of different cementitious mortar mix designs ranging from $C_{80}S_{85}$ to $C_{60}S_{85}$. Therefore, at 56 days, the pozzolanic activity of IWPs (FA, FS, and BS) results in a significant improvement in the quality of cement paste and enhances the microstructure of the transition zone between the aggregate and the binding material, as illustrated in the Figure 4.11b to 4.12. Guo et al. (2023) [372] reported comparable findings regarding SEM imaging, indicating that the mix with a BS substitution level exceeding 30% exhibited a porous structure.

Figure 4.14 present the morphology of hydration products in complex cementitious matrix, namely, portlandite, ettringite, CSH gel, and calcite. The EDS spectrum for all mix designs (Figure 4.13) revealed the presence of essential elements, including Ca, Si, Mg, Fe, Na, K, Al, and O. In conclusion, the microstructure of IWPs-modified mix designs exhibited improvement and elevated density with the incorporation of IWPs across all mixes and curing ages. The extension of the curing period from 28 to 56 days correlates with the development of CSH layers in all mortar mixes, which is associated with enhanced compressive strength and decreased permeability.

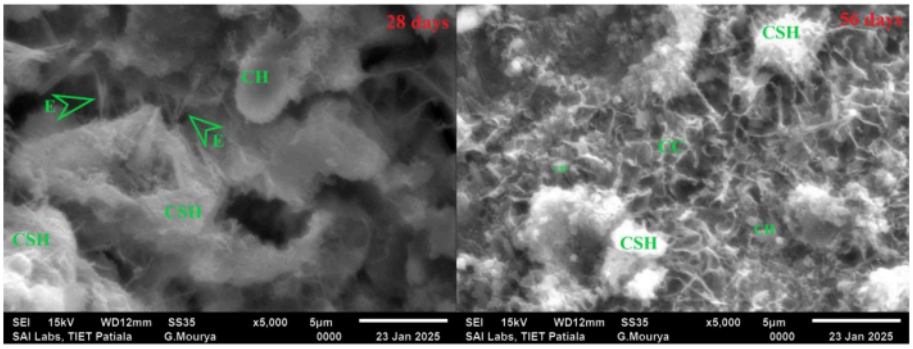

Figure 4.9 SEM micrograph of reference $C_{100}S_{100}$ mix design.

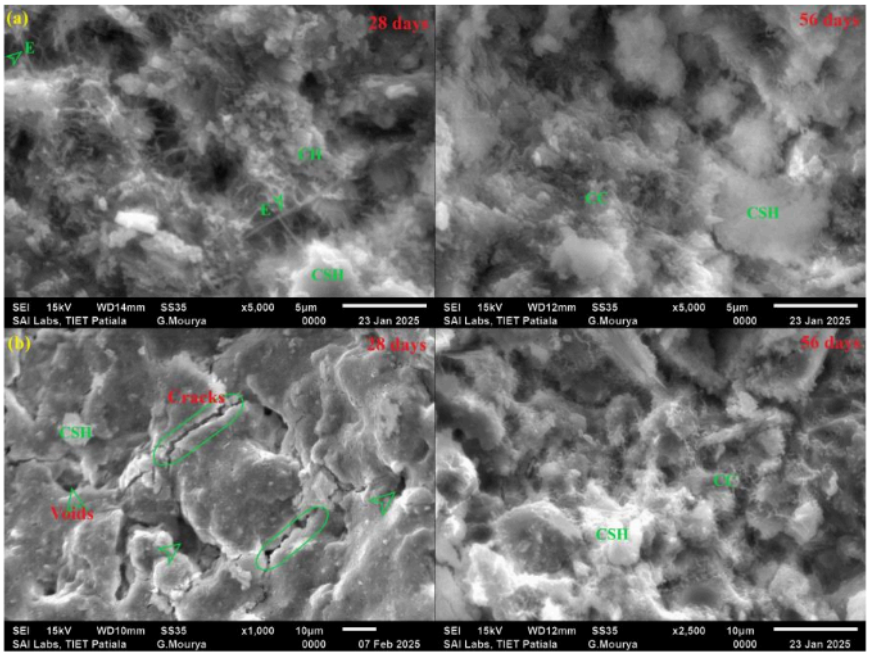

Figure 4.10 SEM micrographs of (a) $C_{85}S_{85}$ mix design and (b) $C_{80}S_{85}$ mix design.

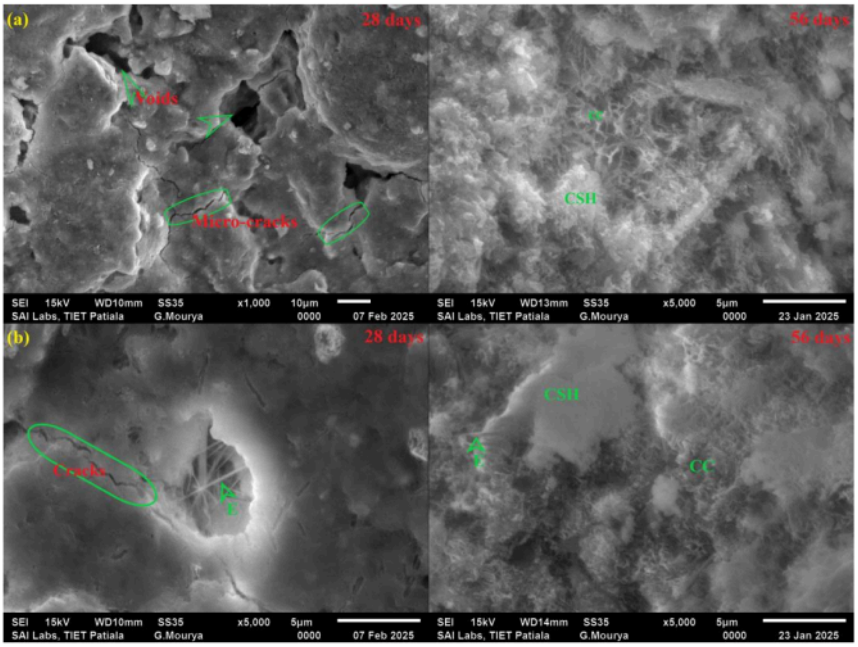

Figure 4.11 SEM micrographs of (a) $C_{75}S_{85}$ mix design and (b) $C_{70}S_{85}$ mix design.

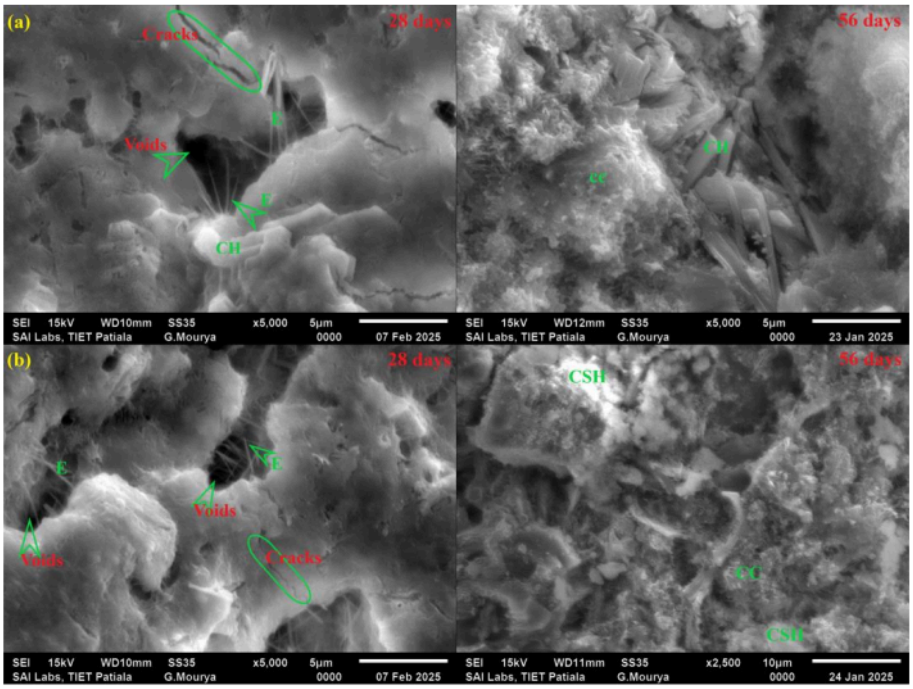

Figure 4.12 SEM micrographs of (a) $C_{65}S_{85}$ mix design and (b) $C_{60}S_{85}$ mix design.

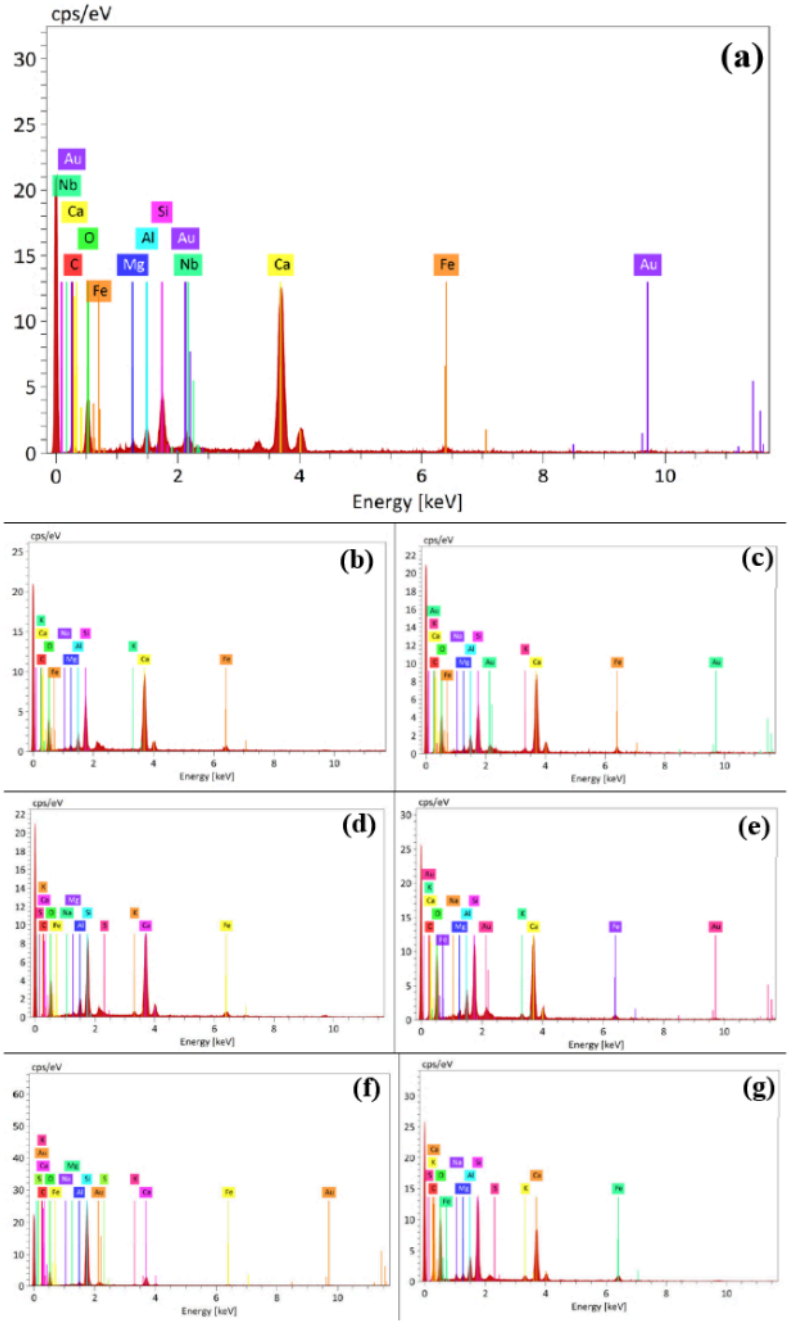

Figure 4.13 EDS spectrum of IWPs-modified cementitious mortar specimens (a) $C_{100}S_{100}$,(b) $C_{85}S_{85}$, (c) $C_{80}S_{85}$, (d) $C_{75}S_{85}$, (e) $C_{70}S_{85}$, (f) $C_{65}S_{85}$ and (g) $C_{60}S_{85}$.

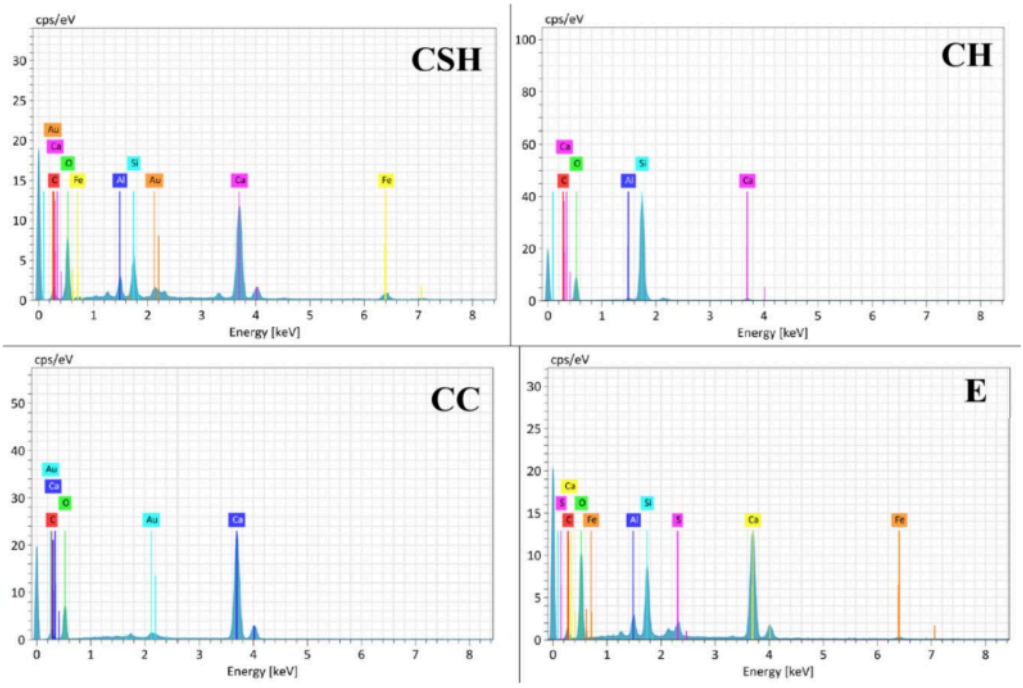

Figure 4.14 The EDS spectrum of hydration product: portlandite (CH), ettringite (E), CSH gel, and calcite (CC).

4.1.5.2 XRD

An XRD study was conducted to investigate the crystalline structure and phase development in different IWPs-modified cementitious mortar specimens. The outcomes for both the reference $C_{100}S_{100}$ mix and the IWPs-modified mix, ranging from $C_{85}S_{85}$ to $C_{60}S_{85}$, at curing ages of 28 and 56 days, respectively, are presented in Figure 4.15. The study of diffraction data indicated that the predominant hydrated phases were Quartz (silicon dioxide), Vaterite also known as calcium carbonate, and Sodium Aluminum Silicate Hydrate (TSZ) also recognized as Albite. Additional phases exhibiting low-intensity peaks included Gismondine, recognized as calcium aluminosilicate hydrate, Calcium Silicate hydrate, Calcium Hydroxide, Richterite, and Nepheline. The primary phases were found to be consistent across all ages. The illustration designates the hydrated planes of quartz (SiO_2) as 'Q', Vaterite ($CaCO_3$) as 'V,' Gismondine ($CaAl_2Si_7O_{18}$•$1.7H_2O$) as 'G,' Albite ($Na(AlSi_2O_6)(H_2O)1.1$) as 'A', Calcium Silicate Hydrate

(Ca_3SiO_5•$2H_2O$) as 'C', Calcium Hydroxide ($Ca(OH)_2$) as 'H', Richterite ((Na, Ca)$_2$.$75Mg_5Si_8O_{22}(OH)_2$) as 'R', and Nepheline ($NaAlSiO_4$) as 'N.'

At the curing age of 28 days, XRD analysis of IWPs-modified mix designs indicated that the predominant hydrated phase is SiO_2, which does not contribute to the pozzolanic activity of the cement mortar. However, Carbon dioxide (CO_2) in the ambient air combines with $Ca(OH)_2$ to produce $CaCO_3$, which enhances the mechanical strength of different mix designs. As the curing time extends, a chemical reaction involving SiO_2 in the hydrated products inside the cement matrix produces CSH gel, which provides strength to different IWPs-modified mortar mixes. Consequently, at 56 days, the pozzolanic activity of IWPs (FA, BS, and FS) results in a comprehensive enhancement of the cement paste quality and an increase in strength compared to the 28-day curing period. It should be noted that the minimal quantity of $Ca(OH)_2$ in all mortar mixes was observed for both age groups, indicating its extensive consumption during the hydration reaction. This facilitates the formation of a dense microstructure and further growth of CSH gel, enhancing the microstructure of the IWPs-modified mortar mix designs, hence improving their respective strength and durability qualities.

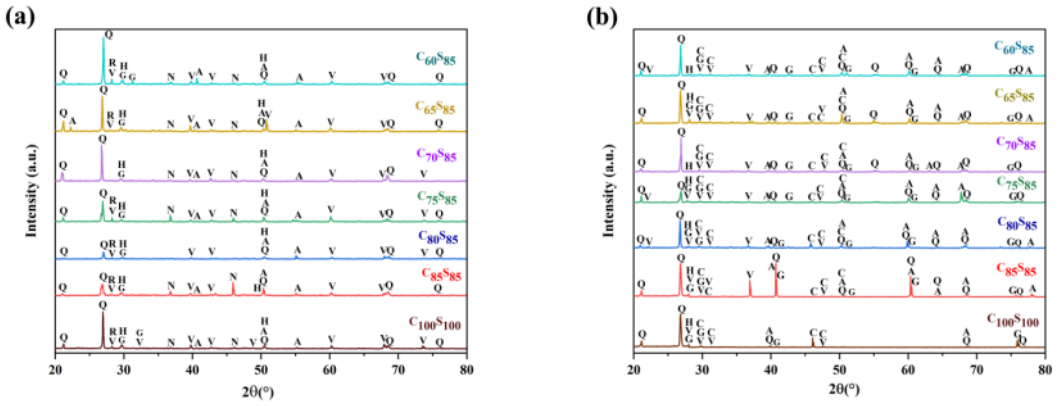

Figure 4.15 The XRD image of different IWPs-modified cementitious mortar specimens at (a) 28 days and (b) 56 days.

4.1.5.3 TGA/DTA

The thermal properties of different IWPs-modified cementitious mortar samples at curing ages of 28 and 56 days were assessed using TGA/DTA measurements, with results presented in the

Figure 4.16 and Table 4.1. The decomposition of compounds in a cementitious mortar matrix during TGA/DTA analysis can be categorized into three primary stages.

1. The initial stage involves the loss of free water within the 25–105°C temperature range, followed by the dehydration of hydrates at temperatures between 105–300°C.

2. The second stage involves the dehydroxylation of $Ca(OH)_2$ at temperatures ranging from 400°C to 600°C.

3. The third stage involves decarbonizing metastable and well-crystalline phases within the temperature range of 600–850 °C.

The results shown in the Figure 4.16 indicate the presence of peaks at approximately 100°C, 400°C, 650°C, and 850°C, respectively. As previously stated, the dehydroxylation of $Ca(OH)_2$ and the decarbonization of $CaCO_3$ are represented by the peak close to 400°C and in the 600°C to 900°C range, respectively. The mass loss % for the different IWPs-modified mortar mixes across significant temperature ranges are shown in the Table 4.1 and illustrated in the Figure 4.17. The results demonstrate that the mass loss pattern with increasing temperature is consistent across all IWPs-modified mortar samples. However, the mass loss % differs potentially due to different material responses across different temperature ranges. The data obtained w.r.t. total mass loss % across the temperature range of 105 to 1000°C demonstrates that the overall quantity of products in each sample grew over time. This is specifically associated with the increase in carbonate content at 56 days.

Similarly, the TGA curves (Table 4.1) for both age groups indicate that the concentration of $Ca(OH)_2$ in the IWPs-modified samples diminishes with increasing BS content. At 28 and 56 days, the $Ca(OH)_2$ quantity in all tested IWPs-modified mortar samples was lower than in the reference $C_{100}S_{100}$ mortar mix. However, a little variation was noted in the specific case of the $C_{85}S_{85}$ mortar mix at 56 days. This observed trend can be ascribed to the pozzolanic reaction and latent hydraulic properties of the associated SCMs (FA and BS). Hence, it can be stated that in all samples (except $C_{85}S_{85}$), a decline in the quantity of $Ca(OH)_2$ was observed over time.

The carbonate content of the mortar samples is typically estimated using the weight loss observed in the third TGA/DTA region. Therefore, the results derived from the TGA curves

(Table 4.1) indicate that, at 28 days, the carbonate content decreased as the proportion of BS replacement increased. However, sample with a 5% BS replacement level, precisely the $C_{85}S_{85}$ mix, exhibited a significantly distinct trend after 56 days compared to the 28-day results. Following 56 days of the curing period, the minimum value within this temperature range was recorded in the sample $C_{60}S_{85}$, which was likewise lower than the reference $C_{100}S_{100}$ mix. Hence, in most of the examined IWPs-modified mortar samples (for both age groups), the quantity of carbonate improved as the quantity of $Ca(OH)_2$ declined. This is because a considerable quantity of $Ca(OH)_2$ was involved in developing carbonates.

Table 4.1 Total mass loss (%) of different IWPs-modified cementitious mortar specimens across different temperature range.

Mix Designs	105-300°C	400-600°C	600-850°C	105-1000°C
28 days				
$C_{100}S_{100}$	0.60	0.41	5.14	5.44
$C_{85}S_{85}$	2.92	0.38	5.22	7.45
$C_{80}S_{85}$	1.94	0.36	4.75	7.33
$C_{75}S_{85}$	1.91	0.25	4.32	6.93
$C_{70}S_{85}$	1.72	0.26	3.36	6.64
$C_{65}S_{85}$	1.78	0.25	3.39	6.28
$C_{60}S_{85}$	1.62	0.21	4.64	6.33
56 days				
$C_{100}S_{100}$	1.26	0.31	7.47	9.53
$C_{85}S_{85}$	1.56	0.53	7.52	9.77
$C_{80}S_{85}$	1.87	0.24	4.52	7.65
$C_{75}S_{85}$	1.69	0.16	4.52	6.98
$C_{70}S_{85}$	1.35	0.13	4.22	6.8
$C_{65}S_{85}$	1.56	0.16	4.21	6.05
$C_{60}S_{85}$	1.41	0.24	4.11	6.45

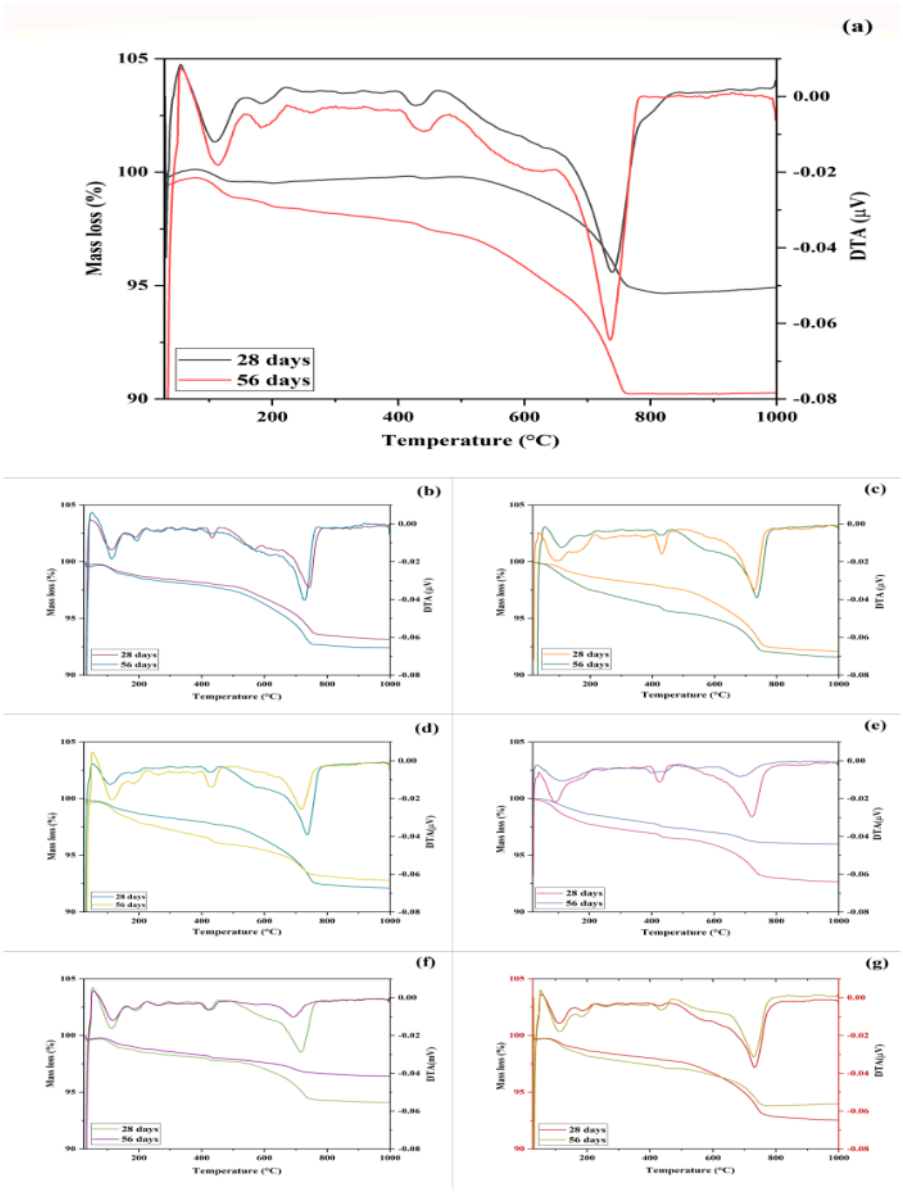

Figure 4.16 The TGA-DTA analysis of different IWPs-modified cementitious mortar samples at curing ages of 28 and 56 days (a) CON, (b) 5%, (c) 10%, (d) 15%, (e) 20%, (f) 25%, and (g) 30%.

4.2 Section B: Fabrication and Analytical Examination of Fe_2TiO_5 Heterostructure For Cementitious Composite

This section verifies the existence of Fe and TiO_2 in the synthesized Fe_2TiO_5 heterostructure and details its formation. The Fe_2TiO_5 heterostructure for cementitious composite was analyzed using a range of analytical techniques, including XRD, FESEM-EDS, UV-DRS, and others. The assessment of the durability and efficacy of the Fe_2TiO_5 heterostructure as a photocatalytic and antibacterial construction material under the visible light spectrum was also conducted.

4.2.1 Analytical Examination of Fe_2TiO_5 Heterostructure for cementitious composite

4.2.1.1 XRD Analysis of Fe_2TiO_5 Heterostructure

To examine the crystalline structure and phase modification of the Fe_2TiO_5 heterostructure after heat treatment at 350ºC, an XRD analysis was performed. The results for IWPs, P25-TiO_2 and Fe_2TiO_5 heterostructure are displayed in Figure 4.17, respectively. The IWPs samples displayed diffraction peaks corresponding to different iron oxide phases, with the predominant hematite (Fe_2O_3) lattice phase identified at 2θ angles of 26.6º, 33.2º, 36.5º, 40.7º, 45.8º, 50.1º, 59.8º, 64.4º, and 68.2º. Additionally, minor peaks of wuestite (FeO) and magnetite (Fe_3O_4) lattice phases were observed at 2θ angles of 36.9º, 42.5º, 60.6º and 36.9º, 53.7º, respectively. The diffraction peaks of Quartz (SiO_2) identified at 2θ angles of 26.5º, 39.5º, 42.7º, and 54.8º were also present in the XRD pattern of IWPs. The image (Figure 4.17b) designates the crystalline planes of hematite (reference code: 01-089-0596) as 'H', while those associated with wuestite (reference code: 01-085-0625) and magnetite (reference code: 01-086-1352) are called 'W' and 'M', respectively. The lattice crystalline planes associated with Quartz (reference code: 01-089-8936) were designated as 'Q'. The P25-TiO_2 sample exhibited distinct peaks corresponding to the anatase phase at angles of 2θ = 25.26º, 37.79º, 48.04º, 53.9º, 54.9º and the rutile phase at angles of 2θ = 27.552º, 36.6º, 39.6º, 41.4º, 55.03º, respectively. In the illustration (Figure 4.17a), the crystalline planes associated with anatase (reference code: 01-071-1166) were labeled as 'A', while the planes related to rutile (reference code: 01-073-1782) were labeled as 'R'.

After going through heat treatment, the Fe_2TiO_5 heterostructure (Figure 4.17a) exhibited new diffraction peaks corresponding to iron titanium oxide (reference code: 00-043-1011) referred to

as 'ITO', sodium titanium oxide (reference code: 00-037-0354) referred to as 'NaTO', titanium silicate (reference code: 00-043-0055) referred to as 'SiTO', and Iron(II) oxide (reference code: 00-047-1409) referred to as 'IO'. The peaks corresponding to ITO were observed at angle of 2θ = 20.8º, 25.6º, 27.4º, 37.8º, 48.5º, and 55.02º, respectively. NaTO exhibited peaks at angle of 2θ =27.4º, 29.4º, and 43.2º, respectively. SiTO showed peaks at angle of 2θ = 23.08º and 26.8º, respectively. IO displayed peaks at angle of 2θ = 26.8º, 29.4º, 36.04º, 39.5º, 47.6º, and 55.02º, respectively. The presence of anatase and rutile phases in the Fe_2TiO_5 heterostructure demonstrates that the photocatalytic activity of TiO_2 in the Fe_2TiO_5 heterostructure was maintained even after undergoing high temperature-heat treatment. Additionally, the presence of ITO and IO peaks supports the existence of both iron and TiO_2 in the Heterostructure. The IO peaks also explain the photo-excited electrons ($e^-_{(Iron\ Oxide)}$) captured by Fe^{3+} ions during the TiO_2 photocatalytic process, leading to the formation of Fe^{2+} ions (equation (4.18)). The existence of ITO peaks also confirms that the iron naturally incorporated in the TiO_2 lattice, forming an active layer of iron-titanium heterojunction oxide (Fe_2TiO_5: Pseudobrookite) (equation (4.3)) on the outer surface of the Heterostructure. Thus, the XRD pattern of the Fe_2TiO_5 Heterostructure displayed the distinctive peaks of anatase TiO_2 and IWPs (particularly Fe_2O_3), indicating the successful synthesis of the Fe_2TiO_5 heterojunction structure during the catalyst preparation method of the present research.

$$\boldsymbol{TiO_{2(outersurface\ coating)} + Fe^{3+}_{(main\ element\ of\ IWPs\ utilized\ for\ cement\ mortar\ production)}} \xrightarrow{\boldsymbol{heat\ treatment\ at\ 350^0C}} \boldsymbol{Fe_2TiO_{5(iron-titanium\ oxide\ complex)}} \quad \textbf{4.3}$$

Similar results have been reported by Afonso et al. (2022) [373] and Ali et al. (2017) [374], where they observed the appearance of new peaks corresponding to $FeTiO_3$ (ilmenite- ITO) after subjecting the Fe-modified TiO_2 powder to different heat treatment processes. However, conventional techniques have been utilized to synthesize the Fe-TiO_2 in the before-mentioned study, whereas the present research cites an inherent heterojunction formation approach to achieve Fe_2TiO_5 Heterostructure. This ITO complex improves the potency of the Fe_2TiO_5 catalyst under visible light, and the idea was further validated using UV–vis DRS spectroscopy, as described in section (4.2.2.3.). The presence of NaTO and SiTO peaks can be attributed to the

chemical connection between TiO_2 and the other components of cement and IWPs utilized in producing Fe_2TiO_5 Heterostructure.

It is commonly noted that following a heat treatment process, the diffraction peaks of iron-modified TiO_2 catalyst increase slightly in width. Their respective intensities of the anatase phase drop, whereas the rutile phase rises [373]. A similar finding for the anatase phase has been observed in the present study. Therefore, the XRD spectrum peaks corresponding to the anatase phase were analyzed. Specifically, the crystal planes (101), (105), and (200) were examined, along with the diffraction plane (110) and (101) of the rutile phase. These peaks were selected to calculate the average crystallite size and lattice parameters of the Fe_2TiO_5 Heterostructure. The crystallite size was calculated using the Scherrer equation (4.4), which is as follows:

$$\boldsymbol{D = \frac{K\lambda}{\beta cos\theta}} \qquad \textbf{4.4}$$

where crystallite size is denoted as D, the wavelength of the Cu Ka source is represented by λ, which has a value of 1.5406 Å. The diffraction peak's full width at half maximum (FWHM) is denoted as β. Additionally, K is a constant with a value of 0.94, and θ represents the diffraction angle at the peak maximum. The lattice parameters were obtained using the following equations (4.5) & (4.6):

$$\boldsymbol{d_{(hkl)} = \frac{\lambda}{2sin\theta}} \qquad \textbf{4.5}$$

$$\boldsymbol{\frac{1}{d_{(hkl)}}^2 = \frac{h^2+k^2}{a^2} + \frac{l^2}{c^2}} \qquad \textbf{4.6}$$

where $d_{(hkl)}$ represents the distance between crystal planes of (hkl). The variable λ represents the X-ray wavelength. The variable θ represents the diffraction angle of the crystal plane (hkl). The variables hkl represent the index of the crystal plane. The variables a, b, and c represent the lattice parameters, such that, for TiO_2 $a = b \neq c$ [376].

Table 4.2 The average crystallite size and lattice parameters for pure P25-TiO_2 and Fe_2TiO_5 Heterostructure, respectively.

Nano-composition	Crystalline Size (nm)		Lattice Parameter [A°]			
	Anatase	Rutile	Anatase		Rutile	
			a(=b)	*C*	*a(=b)*	*C*
TiO_2	28 ± 1.5	38 ± 1.92	3.78	9.51	4.59	2.95
Fe_2TiO_5 Heterostructure	31 ± 2.1	35 ± 1.94	3.78	9.51	4.59	2.95

Table 4.2 displays the determined average crystallite size and lattice parameters for pure P25-TiO_2 and Fe_2TiO_5 Heterostructure. The average crystallite size of TiO_2 nanoparticles w.r.t. the anatase and rutile phases was approximately 28.1 nm and 37.89 nm, respectively. Following the heat treatment process, the size of nanoparticles of Fe_2TiO_5 Heterostructure was measured to be 31.203 nm for the anatase phase and 34.95 nm for the rutile phase. Compared to the reference TiO_2, the crystallite size increased significantly for the anatase phase. Our findings align well with the results reported by Wang et al. (2011) [377]. However, specific investigations have presented contradictory findings regarding the impact of iron inclusion on the crystallite size of TiO_2. For instance, Moradi et al. (2016) [378] and AL Jawad et al. (2017) [379] have documented that incorporating iron into the TiO_2 lattice reduces the crystallite size. Therefore, based on the results, it can be concluded that adding iron improves the crystallization degree of the rutile phase in the nanoparticles of Fe_2TiO_5 Heterostructure.

The lattice constant values for the anatase phase of TiO_2 were calculated as 3.78 Å for a (=b) and 9.51 Å for c. For the rutile phase, the lattice constant values were estimated as 4.59 Å for a (=b) and 2.95 Å for c. The computed lattice parameters for heterostructure nanoparticles closely resemble the reference TiO_2. Therefore, this suggests that iron has been incorporated into the TiO_2 lattice without altering the average unit cell dimension [376]. Similar findings have been reported by Moradi et al. [378], Pang et al. [380], and Stoyanova et al. [381], where iron-modified TiO_2 demonstrated almost equal lattice parameters compared to reference TiO_2.

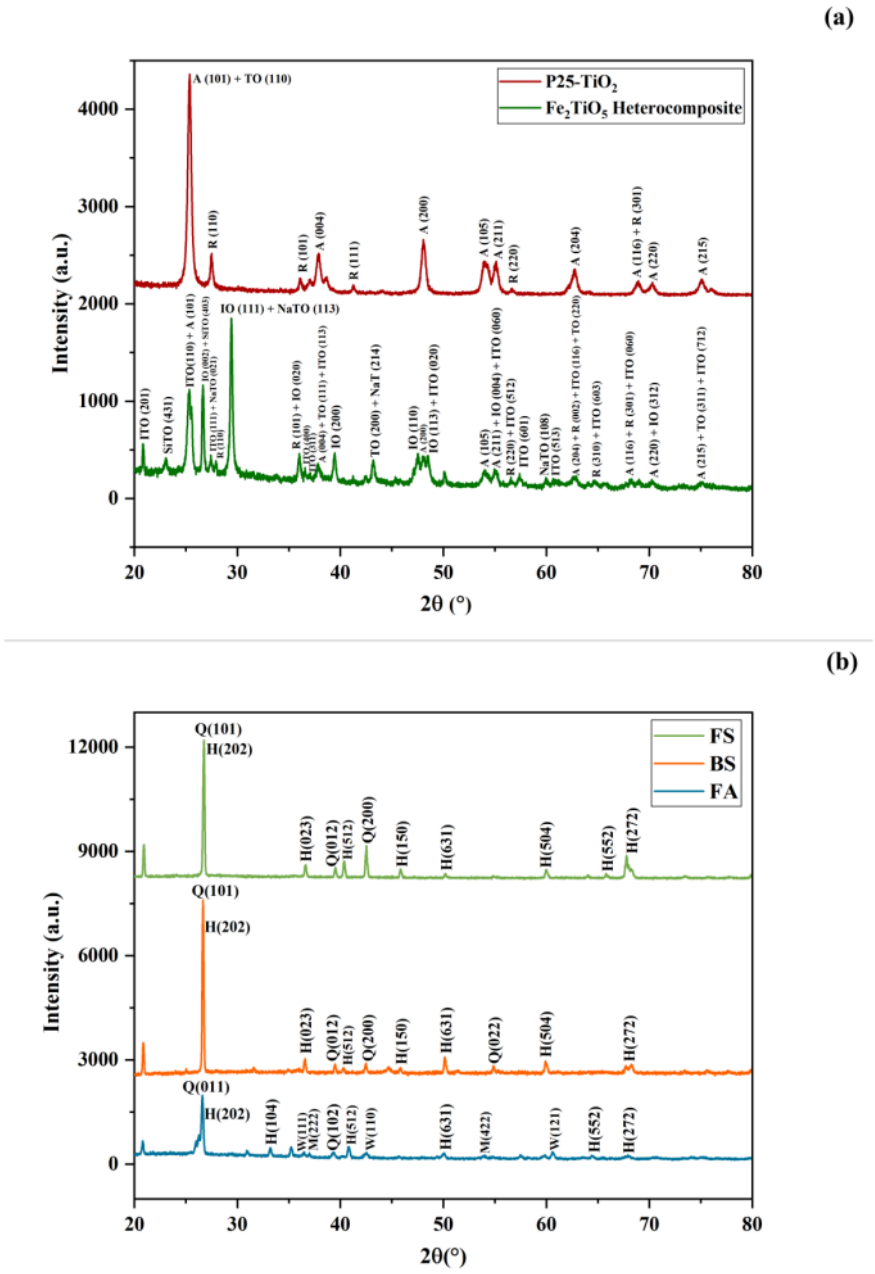

Figure 4.17 The XRD pattern of (a) simple P25-TiO_2 and Fe_2TiO_5 Heterostructure and (b) IWPs (FA, FS & BS).

4.2.2 Morphological Characteristics

4.2.2.1 FESEM-EDS with Elemental Mapping

The FESEM pictures provided a qualitative assessment of the particle size and morphology. The technique is utilized to examine the manner of homogenization and dispersion of the samples. Figure 4.18a and 4.18b show the FESEM micrographs/images of the cementitious samples before and after TiO_2 coating, respectively.. The images illustrate a clear morphological distinction between the coated nanoparticles of Heterostructure and the uncoated cementitious sample. Typically, Fe_2TiO_5 Heterostructure samples are composed of small primary particles clustered together. Conversely, the uncoated pieces comprise larger cementitious particles, measuring in the micron size range.

An EDS was performed to analyze the chemical characterization, emphasizing the elemental analysis of the selected samples. The resulting pattern is depicted in Figures 4.18. The EDS pattern of the Fe_2TiO_5 Heterostructure samples exhibits distinct peaks corresponding to titanium (Ti), iron (Fe), and oxygen (O). This demonstrates the effective incorporation of Fe into the host structure of TiO_2, resulting in oxygen deficits. To confirm that the presence of Fe in the coated Fe_2TiO_5 Heterostructure specimen is only a result of the utilized IWPs mixed with cement and sand, EDS was performed on the uncoated cementitious samples (Figure 4.18a), and IWPs (Figure 3.4 & 3.7). The EDS impressions of uncoated cementitious samples and IWPs show clear peaks, indicating the presence of Fe and O components. These peaks confirm that the iron used in the Fe_2TiO_5 Heterostructure casting procedure came from the IWPs, and no external iron was used.

The elemental mapping was also conducted on the selected samples. Figure 4.19a depicts the even distribution of Ti, Fe, and O elements throughout the whole visual area of the Fe_2TiO_5 Heterostructure specimens. In contrast, only Fe and O elements were detected in the visual area of the uncoated specimen (Figure 4.19b). The elemental mapping results show that the surface-active Fe_2TiO_5 heterojunction structure (equation 4.3) is dispersed evenly over the coated specimen, indicating that the Fe has been uniformly integrated with the TiO_2 lattice. Thus, the analysis results suggest that the utilized materials, TiO_2 and IWPs, worked well together to create sustainable building materials.

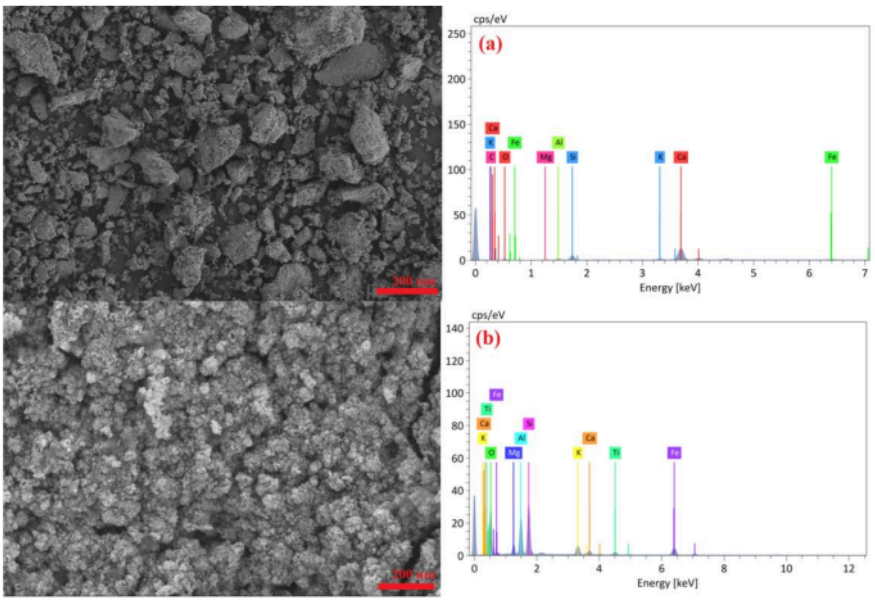

Figure 4.18 The FESEM microscopic images with corresponding EDS pattern of the (a) uncoated cement mortar sample and after (b) Fe_2TiO_5 Heterostructure sample.

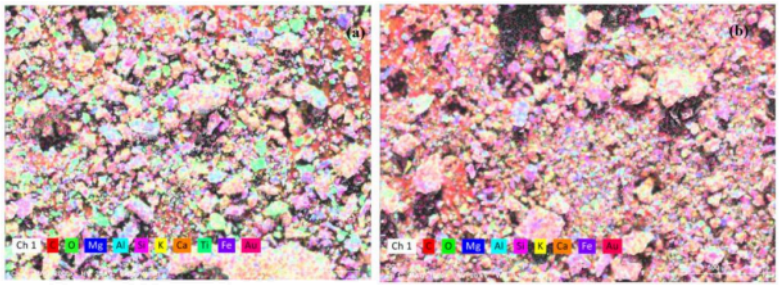

Figure 4.19 The elemental mapping plot of (a) Fe_2TiO_5 Heterostructure and (b) uncoated cement mortar sample.

4.2.2.2 TEM with SAED and HRTEM

While FESEM provides a general idea of particle size and morphology, TEM images can better assess the morphological characteristics, internal structure, and lattice spacing of Heterostructure nanoparticles. Figure 4.20a depicts the TEM images of Fe_2TiO_5 Heterostructure. The images demonstrate that the fabricated Fe_2TiO_5 nanoparticles formed a cluster with a highly crystalline structure. Furthermore, they exhibited non-spherical morphology, with an average particle size of

13 to 34.5 nm. The TEM results closely align with the average crystallite size derived from the XRD pattern using the Scherrer equation (Table 4.2). The size distribution is depicted in histogram form in the Figure 4.21b. The Figure 4.21a illustrates the SAED micrograph of the Fe_2TiO_5 Heterostructure, wherein the electron patterns reveal a combination of dotted rings and spots, comparable to the ones observed in pure P25-TiO_2 (i.e., continuous spotty rings) [382] and Fe_2O_3 (i.e., intense random spots) [383], respectively. Consequently, the observed electron pattern confirms the presence of Fe_2O_3 nanoparticles on the surface of TiO_2 nano-balls. The characteristic diffractions of both P25-TiO_2 and hematite are indicated in the SAED patterns. As a result, the SAED analysis is also compatible with the XRD results illustrated in Figure 4.18.

The lattice spacing was determined by measuring the distance between each lattice fringes [384]. In turn, two different types of crystalline plane spacing were identified via high-resolution TEM (HRTEM) microscope images of the Fe_2TiO_5 Heterostructure, as depicted in Figure 4.21b. The crystal structure of TiO_2 and Fe_2O_3 was recognized based on the close match between the d-spacing of their respective lattice plane from the JCPDS file and the width of the lattice fringe observed in HRTEM images [385]. Hence, the determined lattice spacing of 0.35 nm and 0.25nm aligns well with the arrangement of the crystalline plane (101) TiO_2 anatase and (110) hematite structure, respectively. The findings of the HRTEM image suggest that the Fe_2TiO_5 Heterostructure exhibits favorable lattice compatibility between TiO_2 and Fe_2O_3 at the interface region.

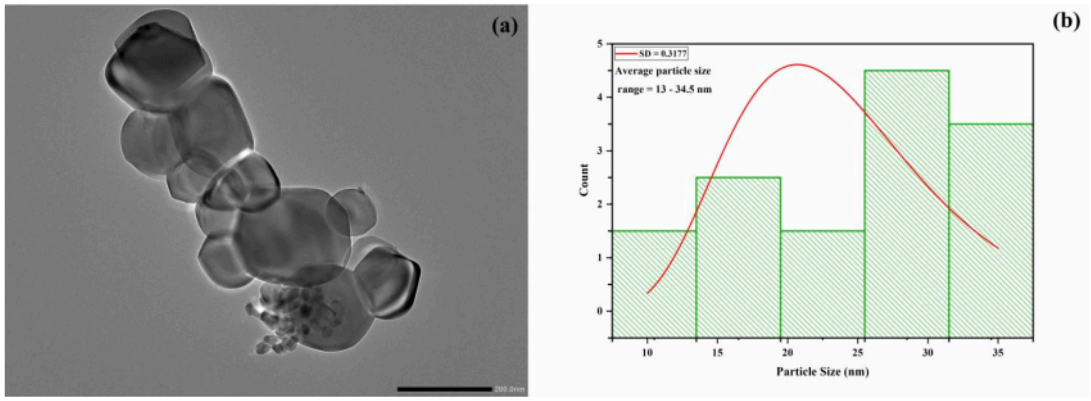

Figure 4.20 (a) TEM image of Fe_2TiO_5 Heterostructure with the histogram plot (b) of average particle size calculated using HRTEM images.

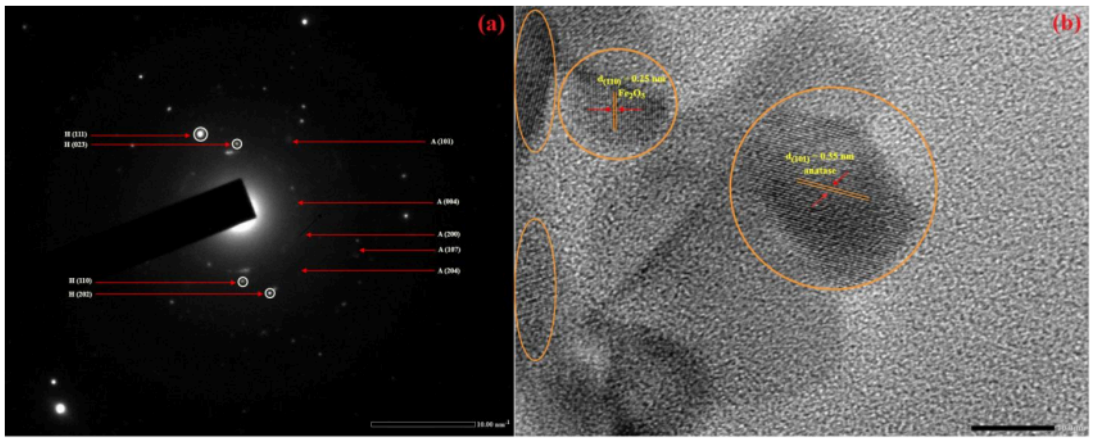

Figure 4.21 The (a) SAED pattern along with (b) HRTEM impression of Fe_2TiO_5 Heterostructure.

4.2.2.3 UV-DRS Analysis of Fe_2TiO_5 Heterostructure

The UV–vis diffuse reflectance spectra (DRS) were used to analyze the optical characteristics of the Fe_2TiO_5 Heterostructure and pure P25-TiO_2. The results are presented in Figure 4.22, demonstrating that the absorption peak of Fe_2TiO_5 Heterostructure is significantly extended towards visible light, in contrast to pure P25-TiO_2. The red shift observed in the UV-Vis spectrum is caused by incorporating the 3d electron state of Fe^{3+}, namely $3d^5$, into the conduction band of TiO_2 [386], [387]. While incorporating Fe ions into TiO_2 does not alter the position of the valence band gap of TiO_2, it does bring new energy levels (Fe^{3+}/Fe^{4+}) from the transition of Fe ions into the band gap of TiO_2 (Figure 4.42a). Consequently, the absorption peak of Fe_2TiO_5 Heterostructure extends to longer wavelengths.

To provide additional evidence for the abovementioned idea, we estimated the optical energy band gap of the Fe_2TiO_5 Heterostructure within the spectral range of 200 to 800 nm. The results of this calculation are displayed in the figure. The reference compound Barium sulfate ($BaSO_4$) was used to establish the baseline of the samples. The direct energy band gap of the samples was calculated by computing the linear intercept of the $(\varepsilon h\nu)^2$ vs $h\nu$ plots, using the Tauq equation [388] (Figure 4.22) as shown in equation (4.7).

$$(\alpha h\nu)^{1/n} = A(h\nu - E_g) \quad \textbf{4.7}$$

The equation represents the relationship between the energy band gap (E_g) in electron volts (eV), Planck's constant (h), the frequency of the photon (ν) in Hertz (Hz), and the proportionality constant (A). A reduction in the direct band gap of the Fe_2TiO_5 Heterostructure (2.57 eV) compared to pure P25-TiO_2 (3.05 eV) has been detected. This significant improvement in the light absorption capacity of the Fe_2TiO_5 Heterostructure can be due to the fabrication of a surface-active Fe_2TiO_5 heterojunction oxide layer, leading to an interfacial effect. The introduction of iron to the TiO_2 lattice reduced its band gap energy, leading to a trapping level between the valence and conduction bands [83]. This reduction caused a shift of the band gap towards the visible region of the electromagnetic spectrum. Khan et al. [389] found that reducing the band gap can enhance the photocatalytic reactivity when exposed to visible light. Therefore, it may be inferred that the developed Fe_2TiO_5 Heterostructure can undergo a photocatalytic reaction when exposed to visible light. Similar findings have been discovered by Pongwan et al. and Teoh et al., where the photodegradation of oxalic acid in visible light, which does not happen with TiO_2, was detected in Fe-TiO_2 photocatalyst samples [390], [391]. JImínez et al. found that the photocatalyst Fe-TiO_2 made it capable of degrading phenol under visible light conditions [392]. Therefore, confirming the practical functionality of the developed Heterostructure under visible light indicates that the iron has been doped onto the outer-coated photocatalyst TiO_2. Furthermore, research has shown that Fe-TiO_2 photocatalysts exhibit antibacterial properties when exposed to visible light, as confirmed by previous studies [381], [393], [394]. This could provide a rationale for our research findings on the antibacterial properties of the examined Fe_2TiO_5 Heterostructure (described in section 4.2.4. & 4.3.2..).

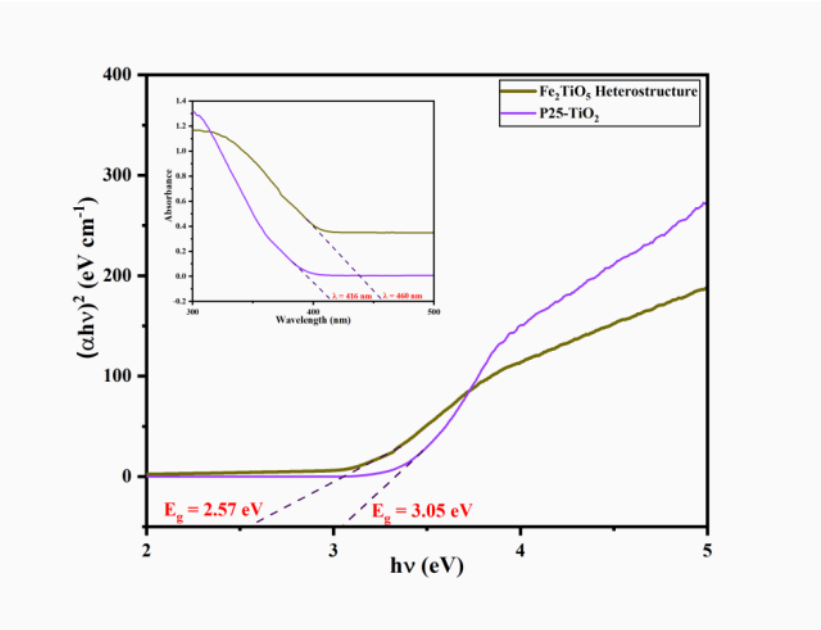

Figure 4.22 UV-DRS plot of P25-TiO_2 and Fe_2TiO_5 Heterostructure.

4.2.2.4 XPS Analysis of Fe_2TiO_5 Heterostructure

Utilizing X-ray photoelectron spectroscopy (XPS), the chemical composition of surface elements was investigated using a surface-sensitive characterization technique. Table 4.3 displays the atomic percentage (%) of various elements present on the outer surface of the Fe_2TiO_5 Heterostructure, such that the elements Ti, O, Fe, Na, Si, and Fe were detected. Na and Si suggest other elements in the IWPs utilized during the Heterostructure production, as confirmed in the XRD and EDS analysis (4.2.1.1.) & (4.2.2.1.). The corresponding survey spectra of detected elements are depicted in Figure 4.23. The fabricated Heterostructure is devoid of carbon; nevertheless, the carbon peak observed in the survey spectrum scan of the Fe_2TiO_5 Heterostructure is attributed to the background. The presence of two distinct peaks in the survey spectrum scan of O 1s can be attributed to Fe_2O_3, Fe_3O_4, and TiO_2 at around 530.2 eV and surface H_2O at around 532.1 eV [392]. Four peaks were identified at 457.8, 458.8, 463.4, and 464.6 eV after the Ti high-resolution survey scan was de-convolved. These peaks are associated with Ti^{3+} $2p_{3/2}$, Ti^{4+} $2p_{3/2}$, Ti^{3+} $2p_{1/2}$, and Ti^{4+} $2p_{1/2}$, respectively. The Ti^{3+} peaks can be attributed to the formation of oxygen vacancies. In this process, the electrons from O atoms cause the conversion of Ti^{4+} ions to Ti^{3+} ions to maintain charge equilibrium. It is important to

highlight that, based on the literature, the XPS spectrum scan of pure TiO_2 did not show any Ti^{3+} peaks [395], [396]. In figure 4.24, the weak iron peaks are also displayed. In the Fe high-resolution survey spectrum scan, the presence of Fe_2O_3 and Fe_3O_4 was confirmed by the peaks identified at around 709.3, 710.6, 711.9, 713.7, and 725.2 eV [397]. Ismail et al. [398] have reported similar research, observing identical Fe, Ti, and O peaks at 724 eV, 458.6 eV, and 529.8 eV, respectively. Consequently, the presence of both Fe and Ti elements in a single system has been verified, confirming the formation of the surface-active Fe_2TiO_5 heterojunction oxide layer on the cementitious composite.

Table 4.3 The atomic percentage (%) of elements present on the outer surface of the Fe_2TiO_5 Heterostructure.

Element	Atomic Percentage (%)
Ti	19.18
O	64.07
Fe	5.25
Si	6.17
Na	5.33

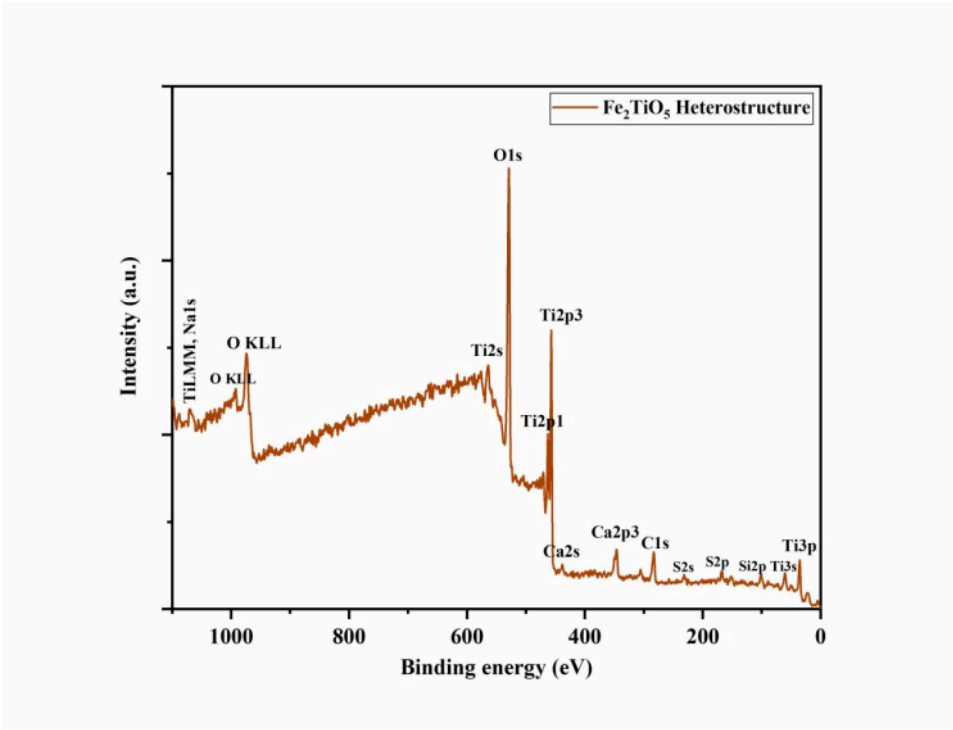

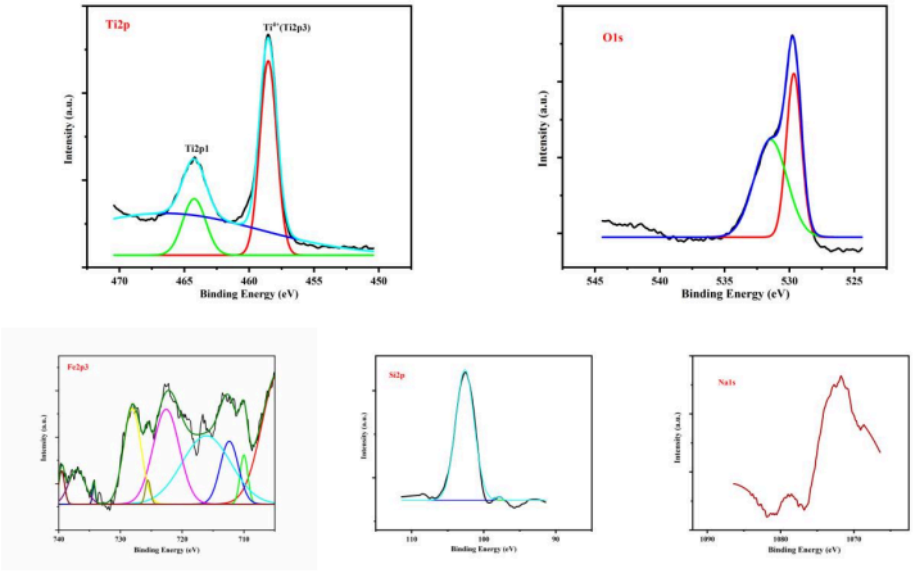

Figure 4.23 XPS survey spectra of Fe_2TiO_5 Heterostructure

4.2.2.5 FTIR Analysis of Fe_2TiO_5 Heterostructure

The FTIR spectrum offers evidence regarding the functional groups present in the system, inter- or intra-molecular interactions, and its molecular geometry. The FTIR spectrum of the Fe_2TiO_5 Heterostructure was analyzed to determine the vibrational bands present in the cementitious system. The IR spectra of the P25-TiO_2 and Fe_2TiO_5 Heterostructure are illustrated in Figure 4.24.

The formation of Ti-O-Ti vibration bonds in both spectra is shown through multiple peaks between 400 and 1200 cm^{-1} wavenumber, thus verifying the presence of the TiO_2 lattice. The TiO2 anatase phase for the P25-TiO_2 and Fe_2TiO_5 Heterostructure appeared in the spectra at 503.42 cm^{-1} and 451 cm^{-1} wavenumber, respectively. The findings align with a previously published study [399] that indicated the presence of Ti-O-Ti vibrations, particularly in the anatase phase, within the range of 400 to 640 cm^{-1}. These bands are crucial for augmenting the photocatalytic properties in the Fe_2TiO_5 Heterostructure [400]. The peak at 458 cm^{-1} in the IR spectrum of Fe_2TiO_5 Heterostructure indicates the existence of a Si-O-Fe bond [401]. Similarly, the existence of peaks at 618 cm^{-1} and 774 cm^{-1} in the IR spectra of Fe_2TiO_5 Heterostructure is attributed to Si-O vibration bonds. Wang et al. (2016) [402] indicated that bonds within the range of 510-590 cm^{-1} wavenumber may signify vibrations among FeO_6 molecules. Therefore, the peak at 555 cm^{-1} may signify identical Fe-O vibrational bonds in the IR spectra of the Fe_2TiO_5 Heterostructure. Additionally, the peaks at 2309 cm^{-1} and 2332 cm^{-1} in the Fe_2TiO_5 Heterostructure spectra indicate the formation of Ti–O–Fe vibrational bonds, which, arising from the intrinsic heterojunction process, further substantiates the presence of Fe in the cementitious Heterostructure. Bansal et al. (2018) [403] observed analogous peaks indicating the occurrence of Ti–O–Fe bonds in Fe/TiO_2 composite beads. Thus, the FTIR results align well with the XRD pattern of the Fe_2TiO_5 Heterostructure (Figure 4.18), confirming the occurrence of 'ITO' and 'IO' diffraction peaks.

In the photocatalytic process, all oxygen-containing groups significantly influence the photocatalytic activity and can produce additional hydroxyl (OH•) radicals ions [404]. The peaks at 1622 cm^{-1} and 1632 cm^{-1} for P25-TiO_2 and Fe_2TiO_5 Heterostructure, respectively, belong to the Ti–OH groups, indicating hydroxyl groups present on the TiO_2 surface, which reveal coordination voids in the presence of water [405]. Furthermore, the IR spectra bands

observed at 1564.3 cm^{-1} and 3045 cm^{-1} wavenumber for P25-TiO_2 and at 1588 cm^{-1} and 3045 cm^{-1} for the Fe_2TiO_5 Heterostructure are indicative of the asymmetrical and symmetrical stretching vibration bonds of the –OH group, specifically pertaining to water and hydroxyl groups, as reported in multiple research studies [382], [406]–[408]. These suggest the absorption of hydroxyl (OH) groups in the collected samples. The presence of OH groups could improve the photocatalytic capability of the developed Fe_2TiO_5 Heterostructure, as these groups act as primary scavengers for photo-generated charge carriers (e-/h+), facilitating the generation of OH• radical ions essential for contaminant degradation. Thus, the distinctive peaks at 458 cm^{-1}, 555 cm^{-1}, 1632 cm^{-1},and 2332 cm^{-1}in the Fe_2TiO_5 Heterostructure sample demonstrate the inclusion of both TiO_2 and Fe in the cementitious composite.

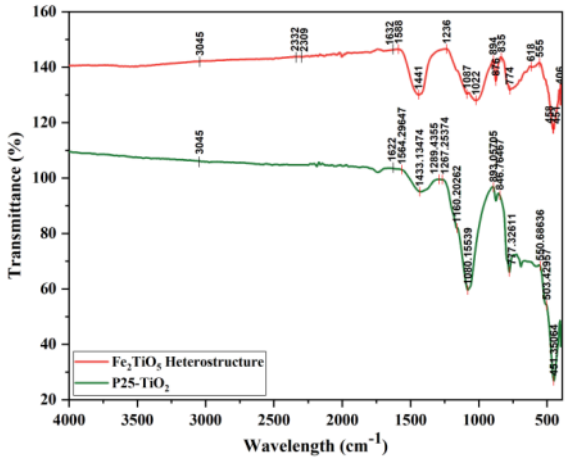

Figure 4.24 FTIR spectra of P25-TiO_2 and Fe_2TiO_5 Heterostructure.

4.2.2.6 Raman Spectroscopy of Fe_2TiO_5 Heterostructure

Raman spectroscopy was conducted to examine the structural phases of Fe_2TiO_5 Heterostructure nanoparticles (NPs) in comparison to P25-TiO_2, as illustrated in Figure 4.25. The Raman spectra of P25-TiO_2 exhibit peaks at 142.8 cm^{-1}, 319.7 cm^{-1}, 517.16 cm^{-1}, and 638 cm^{-1}, confirming that anatase NPs are the primary species in the TiO_2 photocatalyst [409]. The spectra of P25-TiO_2 also displayed additional Raman peaks at 235.02 cm^{-1}, 446.9 cm^{-1}, and 609.3 cm^{-1}, indicating the existence of the rutile phase in the sample. Previous reports have documented the identical band for the rutile phase [383], [410], [411]. The Raman spectra of the Fe_2TiO_5

Heterostructure showcased five TiO_2 anatase peaks at approximately 144.52, 197.05, 395.8, 517.16, and 638.4 cm^{-1}, corresponding to Ti-O vibrations [412]. The anatase peak at 140-142 cm-1 in both samples' spectra is the most prominent among all discovered peaks, indicating the predominance of anatase TiO_2 NPs. The results align with previously reported studies [413]–[415] discussing the impact of different levels of Fe-doping on the photocatalytic and antibacterial properties of TiO_2. Weak and wide bands in the 300-350 cm^{-1} range were also observed in the spectra of the Fe_2TiO_5 Heterostructure. The presence of these bands is not associated with either the anatase or rutile phases of TiO_2, suggesting a correlation with the presence of iron or iron oxides. No other significant peaks of iron oxides were detected in the Raman spectra. Furthermore, the Fe_2TiO_5 Heterostructure NPs maintained the anatase structure, suggesting that the Fe^{3+} dopants naturally integrated into the TiO_2 framework, displacing Ti^{4+} ions. It has been noticed that the Raman band at 142.8 cm^{-1} for Pure-TiO_2 NPs shifts to a higher wavenumber in the Fe_2TiO_5 Heterostructure NPs. The shifts in the Raman peak are generally attributed to alterations in structure, particle size, and the nature of defects, among other factors [413]. Also, the intensity of the Raman bands for Heterostructure NPs was lower compared to that of P25-TiO_2, further supporting the natural incorporation of Fe^{3+} into the substitution site of the TiO_2 lattice, which resulted in lattice distortion and a change in crystallite size (Table 4.2). Hence, it can be stated that the Raman spectral observations align well with the XRD findings.

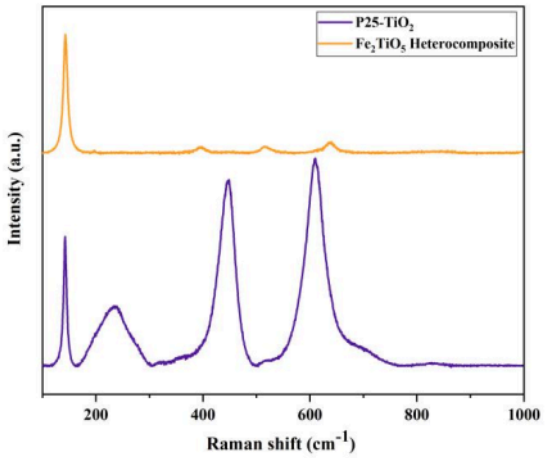

Figure 4.25 Raman Spectra of P25-TiO_2 and Fe_2TiO_5 Heterostructure.

4.2.2.7 TGA/DTA Analysis of Fe_2TiO_5 Heterostructure

The TGA/DTA analysis was employed to examine the weight reduction and phase transition of the Fe_2TiO_5 Heterostructure from 25 to 1000 °C. The thermo-gravimetric curves of the Fe_2TiO_5 Heterostructure and fresh P25-TiO_2 are depicted in Figure 4.26. The findings demonstrate no substantial change in the mass of either sample with temperature variations. The TiO_2 and Fe_2TiO_5 Heterostructure samples exhibited endothermic peaks at 104°C, 640°C, and 80°C, respectively. No additional endothermic peaks were seen in either sample upon heating to 750 °C. This signifies the endothermal reaction, i.e., the evaporating procedure of residual water, and the anatase to the rutile phase transition of TiO_2 does not occur between 25 to 750 °C. Similarly, two exothermic peaks were observed in TiO_2 at 120°C and 788°C, whereas three exothermic peaks were detected in the Fe_2TiO_5 Heterostructure at 133°C, 205°C, and 754°C. The exothermic peak is related to the degradation and combustion of the residual organic compounds adsorbed on the catalyst's surface.

The TG curve indicates that the weight loss of both samples concludes at 800°C, with a total mass loss of 5% for TiO_2 and 5.65% for the Fe_2TiO_5 Heterostructure. The results indicate minimal variations in mass loss for both samples, demonstrating that the existence of iron did not

influence the thermal property of the Fe_2TiO_5 catalyst. Thus, it can be suggested that the Fe_2TiO_5 Heterostructure demonstrated identical thermal stability compared to P25-TiO_2. The current findings are consistent with prior research [416], [417].

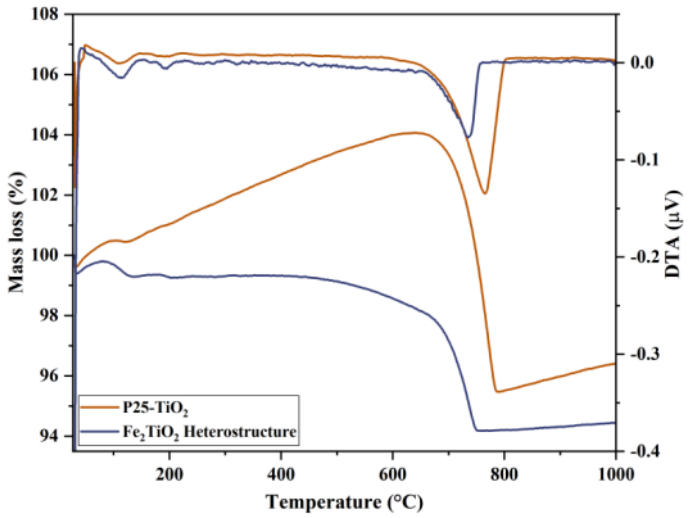

Figure 4.26 TGA-DTA analysis of P25-TiO_2 and Fe_2TiO_5 Heterostructure.

4.2.2.8 BET Analysis of Fe_2TiO_5 Heterostructure

Nitrogen (N_2) adsorption-desorption study was conducted to investigate the porosity of the Fe_2TiO_5 Heterostructure. The adsorption isotherms of N_2 at 77 K were derived from 14 relative pressure values varying from 0.05 to 1. The pore size distribution curve was derived from the desorption region of the N_2 isotherm using the Barrett–Joyner–Halenda (BJH) approach [383], and the resulting N_2 adsorption-desorption isotherm for the Fe_2TiO_5 catalysts is illustrated in the Figure 4.27. The pore size measurements revealed a broad spectrum of pore sizes within the Fe_2TiO_5 Heterostructure, demonstrating the uniformity and non-accumulated components. A BET type II curve was obtained, confirming the mesoporous characteristics of the Fe_2TiO_5 Heterostructure, with a mean pore diameter of 2.64 nm. In a type II isotherm, the horizontal segment in the center signifies the establishment of a monolayer. Such mesoporous heterojunction catalysts often offer expanded active sites for surface contact reactions, resulting in improved photocatalytic activity and high porosity. The BET analysis indicated that the

surface area of the Fe_2TiO_5 Heterostructure was determined to be 73.757 m^2g^{-1}, with a pore volume of 9.1 x $10^{-2}cm^3g^{-1}$. The tested Fe_2TiO_5 Heterostructure samples exhibited a significantly larger surface area, approximately 47.5% more than that of pure P25-TiO_2 (50 m^2g^{-1}) [418] (refer to Table 4.4), which can be ascribed to the surface modification resulting from Fe_2O_3 (IWPs) nanoparticles. The results from adsorption experiments align with the Langmuir adsorption isotherm, indicating a monolayer chemisorption process consistent with the N_2 adsorption-desorption study.

Table 4.4 The surface area and porous parameters of the Fe_2TiO_5 Heterostructure.

Nanomaterial	BET (S_{BET}) m^2/g	Pore Volume (V_{Total}) cc/g	Pore Size ($D_{Average}$) nm
P25-TiO_2	50	--	--
Fe_2TiO_5	73.757	9.1 X 10^{-2}	2.64

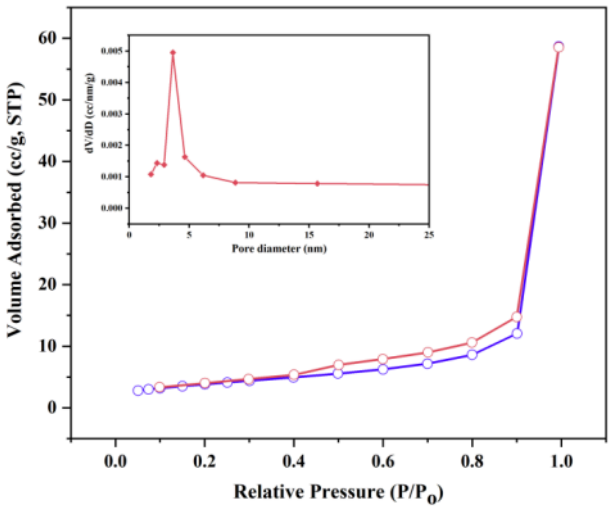

Figure 4.27 The N_2 adsorption-desorption isotherm for the Fe_2TiO_5 catalysts.

4.2.2.9 PL Study of Fe_2TiO_5 Heterostructure

The PL spectrum of pure P25-TiO_2 and Fe_2TiO_5 Heterostructure was analyzed to assess the relationship between photocatalytic efficiency and the recombination rate of photo-induced charge carriers. The PL spectrum was acquired in the range of 300 to 800 nm with an excitation wavelength of 315 nm, and the results are presented in Figure 4.28. Photoluminescence (PL) primarily emerges from the recombination of photo-induced charge carriers. The intensity of the PL spectrum is closely associated with the photo-electro-chemical properties of a semiconductor, wherein the lower PL spectrum suggests a decreased recombination rate of photo-induced carriers [419]. Therefore, the PL evaluation method is predominantly employed to examine the transfer and separation efficiency of photo-induced (e^-/h^+) pairs in semiconductors [420].

Figure 4.28 illustrates that the PL intensity of the Fe_2TiO_5 Heterostructure is less compared to that of pure P25-TiO_2. This indicates that the Fe_2TiO_5 Heterostructure exhibits a considerably decreased (e^-/h+) recombination rate and improved charge separation efficiency relative to pure TiO_2. Also, the decrement in the recombination rate signifies that a substantial amount of photo-induced e^- and h^+ contributes to the photochemical changes, enhancing the photocatalytic and

antibacterial characteristics of the Fe_2TiO_5 Heterostructure (as detailed in sections 4.2.3. and 4.2.4.).

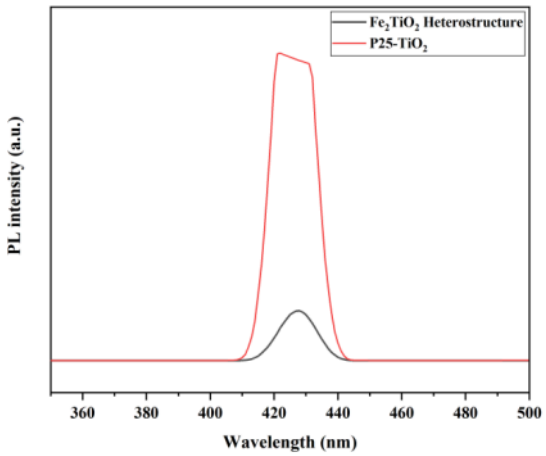

Figure 4.28 The PL spectrum of pure P25-TiO_2 and Fe_2TiO_5 Heterostructure

4.2.3 Evaluation of the Photocatalytic Properties of the Fe_2TiO_5 Heterostructure

The photocatalytic activity of the synthesized Fe_2TiO_5 Heterostructure was assessed by observing the discoloration of MB in aqueous solution under solar-visible light irradiation. The catalyst adsorption and photocatalytic degradation performance of MB are illustrated in Figure 4.31.

4.2.3.1 Initial Findings: UV-vis. Spectrophotometric Measurement

The dye concentration was determined using UV-vis. spectrophotometric measurement. Figure 4.29 demonstrates a gradual decrease in the primary absorption peak of MB dye at 668 nm, accompanied by a corresponding discoloration of the MB solution's color (Figure 4.30) as the time of irradiation increased. This can be attributed to the photocatalytic degradation of the chromophoric group responsible for the color of the MB dye [421]. For the experimental conditions employed, we presume that the measured amount of MB at adsorption-desorption equilibrium is equivalent to the initial concentration C_0.

4.2.3.2 The Photocatalytic Degradation Efficiency of MB Dye

Figure 4.31 illustrates the photocatalytic degradation efficiency of MB dye utilizing two different type of specimens, specifically TiO_2-coated cementitious composite and Fe_2TiO_5 Heterostructure. Initially, a blank experiment was conducted to ensure the accuracy of the experimental program. The MB solution was stirred continuously for 45 min without a catalyst and self-degraded under solar-visible light for 1h. The self-degradation experiment demonstrated that, regardless of the presence of dark or solar-visible light, there was negligible variation in the MB concentration due to the absence of a catalyst. The self-decomposition reaction of MB barely occurred.

Under dark conditions, the change in concentration of MB in the presence of a catalyst can be related to the specific surface area of Fe_2TiO_5 catalyst, which is greater than that of pure TiO_2 (Table 4.4). Consequently, the adsorption capacity of the former was 28% greater than the latter's. This difference can be attributed not only to the adsorption capability, which includes physical adsorption associated with the specific surface area and the porous nature of the material [422] but also to electrostatic adsorption linked to the electrical characteristics of the material [423], [424]. Unlike the neutral electrical charge of TiO_2, the electronegative Fe_2O_3 demonstrated superior cation absorption properties for the cationic MB^+ [425]. Hence, the adsorption capacity of the fabricated Fe_2TiO_5 Heterostructure catalyst improved relative to pure TiO_2.

Under visible light, the investigation on MB degradation demonstrated that the total MB removal rate in the Fe_2TiO_5 Heterostructure was approximately 25% greater than that in TiO_2-coated cementitious composite after 45 min of adsorption followed by 1h of degradation, indicating superior photocatalytic efficiency of the Fe_2TiO_5 Heterostructure compared to TiO_2. Efficient degradation of MB was accomplished using the Fe_2TiO_5 Heterostructure, such that the Heterostructure demonstrated a 93.1% MB removal rate after 1h, in contrast to 68% for simple P25-TiO_2 coated specimens. Hence, the solar-visible light reactivity of TiO_2 is substantially improved by the intrinsic development of a heterojunction with Fe_2O_3. Comparable findings have been reported by [417], wherein the authors investigated the photocatalytic efficacy of various TiO_2/α-Fe_2O_3 (TF) nano-composites (fabricated with different α-Fe_2O_3 ratios) in the visible light spectrum for the decomposition of organic MB dye. The results demonstrated that

after approx. 60 min, the attained degradation ratios were 68% for TF1:0.1, 75% for TF1:0.2, 91.2% for TF1:0.5, and 98% for TF1:1. In conclusion, the 1:1 TiO_2/α-Fe_2O_3 nanocomposite exhibited better photocatalytic efficiency compared to pure TiO_2, pure Fe_2O_3, and other TiO_2/α-Fe_2O_3 (TF) nano-composites.

As a result, it may be inferred that the Fe_2TiO_5 Heterostructure has superior photocatalytic activity compared to simple-TiO_2 coated specimens. The improvement in the solar-visible light photocatalytic activity of the Fe_2TiO_5 Heterostructure can be ascribed to several factors. 1) Enhanced solar energy harvesting via Fe_2TiO_5 Heterostructure, attributed to its reduced band gap energy. 2) the Heterostructure exhibits a larger surface area than pure TiO_2, leading to improved dye adsorption for degradation. 3) Prevention of e^-/h+ recombination occurs through spatial e- transfer from TiO_2 to Fe_2O_3, which extends the duration of photo-generated charge carriers. In addition to photocatalytic studies, the kinetics of MB degradation was also examined by plotting ln (C/C_0) against irradiation time (Figure 4.32). A linear correlation was observed for both catalysts, aligning closely with a pseudo-first-order model. The kinetic data are presented in Table 4.5 as below.

Table 4.5 The kinetic parameters obtained from pseudo-first order fitting the experimental points of Figure 4.32.

Nanomaterial	k constant (min^{-1})	R^2
TiO_2-coated cementitious composite	0.015	0.96
Fe_2TiO_5 Heterostructure	0.029	0.97

4.2.3.3 Mechanism of the Photocatalytic Activity

The potential mechanism underlying the photocatalytic activity of the Fe_2TiO_5 Heterostructure is illustrated in Figure 4.41a and is elaborated upon as follows: Under solar-visible light irradiation, e-/h+ pairs are generated in photocatalyst TiO_2, with Fe_2O_3 acting as shallow trapping sites for the generated charge carriers (e^- or h^+) [426]. The photo-generated e- in the conduction band of TiO_2 can be transferred to the conduction band of Fe_2O_3 via the developed Fe_2TiO_5 heterojunction. The Fe_2O_3 functions both as an e^- and h^+ trap, facilitating the separation of arrival

times to the solution phase (Eqs. (4.10) and (4.11)) or the substrate [427]. This mechanism reduces the recombination rate of the (e^-/h^+) pair, thereby increasing the charge carrier transfer rates and improving the photocatalytic activity of the Fe_2TiO_5 Heterostructure. The same has been expressed through the following equations ((4.8) to (4.13)).

$$TiO_2 + h\nu \rightarrow TiO_2\,(e^- + h^+) \quad \textbf{4.8}$$

$$TiO_2\,(e^-) \rightarrow Fe_2O_3\,(e^-) \quad \textbf{4.9}$$

$$Fe_2O_3(e^-) + O_2 \rightarrow O_2^{\cdot-} \quad \textbf{4.10}$$

$$Fe_2O_3(h^+) + HO^- \rightarrow OH^{\cdot} \quad \textbf{4.11}$$

$$O_2^{\cdot-} + MB\ dye \rightarrow CO_2 + H_2O \quad \textbf{4.12}$$

$$OH^{\cdot} + MB\ dye \rightarrow CO_2 + H_2O \quad \textbf{4.13}$$

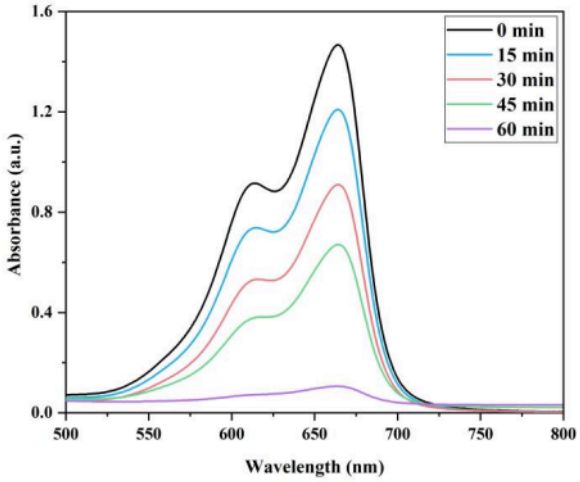

Figure 4.29 UV–vis absorption spectra of aqueous solution of MB during illumination in the presence of Fe_2TiO_5 Heterostructure.

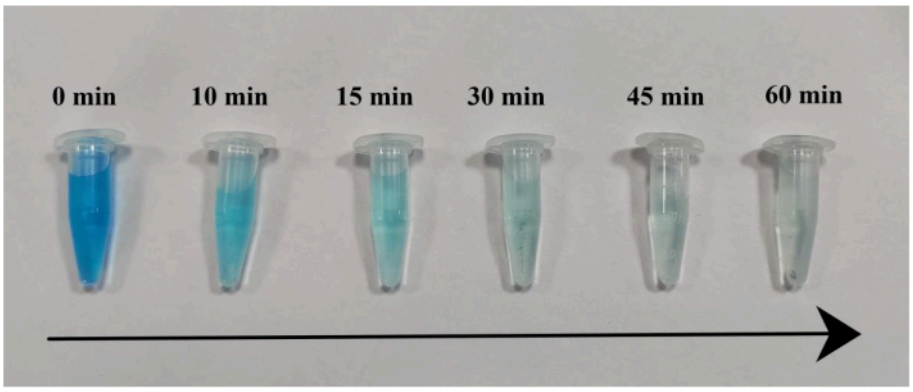

Figure 4.30 The discoloration of the MB solution's color as the time of irradiation increased in the presence of Fe_2TiO_5 Heterostructure.

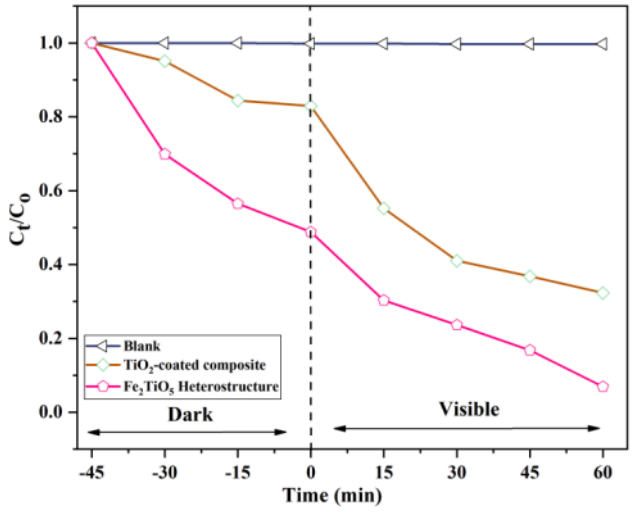

Figure 4.31 Efficiency of the photocatalytic degradation of MB as the variation of C_t/C_0 with irradiation time in the presence of TiO_2-coated composite and Fe_2TiO_5 Heterostructure.

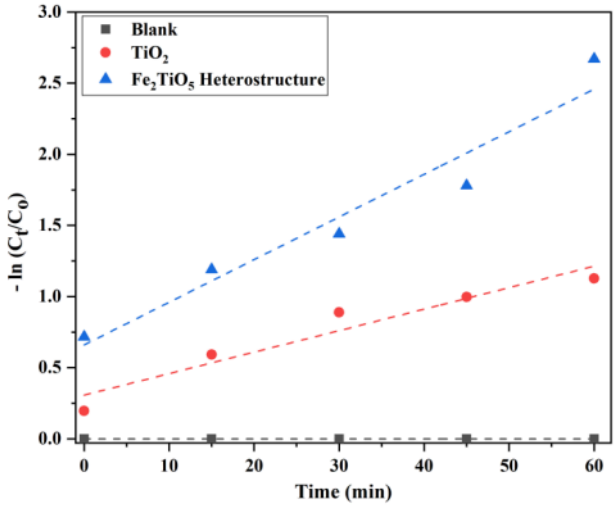

Figure 4.32 The linear (kinetics) plots of – ln (C_t/C_0) vs time for the photocatalytic MB degradation using TiO_2-coated composite and Fe_2TiO_5 Heterostructure.

4.2.4 Evaluation of Photocatalytic-Induced Antibacterial Properties of the Fe_2TiO_5 Heterostructure

Figure 4.33 presents the results of *E. coli* inactivation across different time intervals and conditions under solar-visible light irradiation. The results indicate that the blank (control) samples display the highest number of *E. coli* bacterial colonies. Also, the Fe_2TiO_5 Heterostructure exhibits superior antibacterial efficiency under solar irradiation, achieving an antibacterial ratio of 99% against *E. coli*, in contrast to 68.7% for the simple TiO_2 cementitious composite.

4.2.4.1 Dark Experiment

The dark experiments were conducted with and without each photocatalyst, TiO_2 or Fe_2TiO_5, to assess potential dark inactivation or bacterial adsorption. The blank samples exhibited insignificant results. A reduction of approximately 0.007 ± 0.08 log in *E. coli* count was observed under dark conditions. This minor reduction may be associated with the basic fact that the double-distilled water does not disturb the existence of the *E. coli* within 45 min of the dark

experiment [428]. Similarly, the simple TiO_2 cementitious composite demonstrated a marginally reduced bacterial count compared to the blank samples. A reduction of approximately 0.097 ± 0.06 log in *E. coli* count was observed in TiO_2 cementitious samples after 60 min in the dark.

However, the Fe_2TiO_5 Heterostructure samples demonstrated a 61% antibacterial efficiency, resulting in a log reduction of 0.408 ± 0.07 after the dark experiment. The observed dark inactivation can be ascribed to two main factors:

1) The act of adsorption on the surface of the Fe_2TiO_5 catalyst. As previously discussed (section 4.2.2.8.), the specific surface area of the Fe_2TiO_5 catalyst exceeds that of simple TiO_2 (Table 4.4), resulting in a greater number of adsorption sites for bacteria on the surface of the Fe_2TiO_5 Heterostructure.

2) Additionally, we propose that the antibacterial efficacy without irradiation is linked to Fe ions. Previous studies demonstrate that Fe^{3+} ions possess antibacterial properties by interacting with cell walls and disrupting bacterial metabolic processes [429]. Consequently, these two factors led to a degree of anti-bacterial activity in the absence of irradiations. Similarly findings have been reported by [430]–[432].

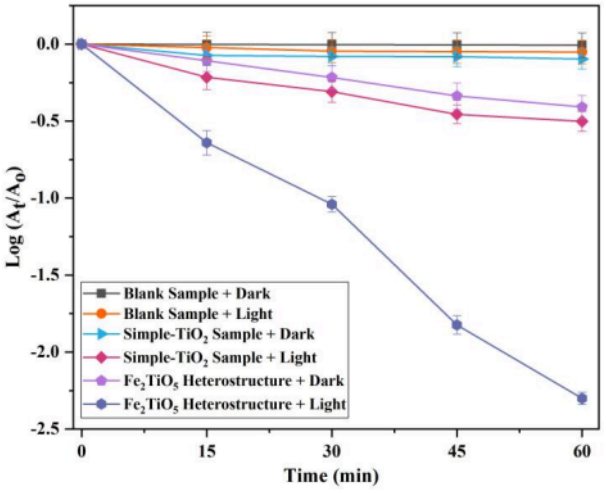

Figure 4.33 The bacterial inactivation curve of TiO_2-coated composite and Fe_2TiO_5 Heterostructure under dark and solar-visible light conditions.

4.2.4.2 Solar-Light Experiment

Insignificant results were again noted for blank samples. An *E. coli* count of approx. 0.012 ± 0.08 log reduction was observed after the 60-min solar light-assisted experiment. This slight reduction in *E. coli* cell count in a blank sample may be attributed to osmotic pressure effect [433]. Furthermore, under solar illumination, the Fe_2TiO_5 Heterostructure samples exhibited a bacterial inactivation efficiency of 99%. The Heterostructure achieved an *E. coli* count of 2.301 ± 0.04 log reduction within 60 min of solar light treatment. Thus, the antibacterial efficiency findings of the Fe_2TiO_5 Heterostructure are consistent with its photocatalytic results (section 4.2.3). As a result, the enhanced photocatalytic efficiency correlates with increased ROS generation under solar-visible light irradiation, thereby improving antibacterial properties [54].

The mechanism of improved photocatalytic disinfection of Fe_2TiO_5 Heterostructure is illustrated graphically in Figure 4.41a and is discussed below: The observed bacterial disinfection by the Fe_2TiO_5 Heterostructure primarily results from the intrinsic heterojunction formation between the Fe_2O_3 catalyst and TiO_2, as confirmed by XRD results. Consequently, the inherent modification of TiO_2 by Fe^{3+} ions reduces the direct energy band gap of TiO_2 (2.52 eV). Thus, the Fe_2TiO_5 Heterostructure can harvest both pure UV and visible light, generating more ROS when exposed to solar sunlight, as confirmed by UV-vis DRS results. Hence, the Fe in cementitious composite behaved as a transitional agent for exchanging photo-generated electrons (e^-) of the outer coated TiO_2 to its conduction band. This Fe^{3+} ions could have volunteered to restrain the recombination of the electron-hole (e^-/h^+) pair. Also, Fe incorporated into TiO_2 lattice and developed Ti^{3+} ions, which further boosted the e^-/h^+ separation ability of the photocatalyst. As a result, the e^-/h^+ pairs were generated without any difficulty even when the fabricated cementitious composite was photo-excited by visible light. After then, these generated e^-/h+ pairs respond chemically with molecular oxygen and water absorbed on the outer surface of the photocatalyst to produce more oxidized radical ions like superoxide radical anions ($^{\bullet}O_2^-$) and radical hydroxyl ions ($^{\bullet}OH$) [432]. These radicals attack the organic constituents of *E .coli*, i.e., the external membrane, lipid, and genetic material, to oxidize and decay them, following the inactivation of bacteria [434], [435]. The generation of radical ions majorly involves the following procedural chemical reactions (Equations (4.15) to (4.23)) when the visible light irradiates Fe_2TiO_5 Heterostructure:

$$TiO_2 + h\nu \rightarrow e^- + h^+ \quad (4.14)$$

$$h^+ + H_2O \rightarrow H^+ + \dot{O}H \quad (4.15)$$

$$e^- + O_2 \rightarrow O_2^- \quad (4.16)$$

$$Ti^{3+} - e^- \rightarrow Ti^{4+} \quad (4.17)$$

$$e^- + Fe^{3+} \rightarrow Fe^{2+} \quad (4.18)$$

$$Fe^{2+} + O_2 \rightarrow Fe^{3+} + O_2^- \quad (4.19)$$

$$O_2^- + e^- + H^+ \rightarrow H_2O_2 \quad (4.20)$$

$$H_2O_2 \rightarrow \dot{O}H \quad (4.21)$$

$$\dot{O}H + organic\ components\ of\ E.coli \rightarrow CO_2 + H_2O \quad (4.22)$$

After evaluating the bactericidal proficiency of the Fe_2TiO_5 Heterostructure, the antibacterial action of the simple-TiO_2 coated cementitious sample under solar-visible light was examined. This investigation aimed to detect whether the decrease in inactivation of *E. coli* is due to simple TiO_2 or Fe_2TiO_5 heterojunction oxide layer under solar irradiation. The result (Fig. 10) discloses that the Fe_2TiO_5 Heterostructure shows more effective photocatalytic induced antibacterial inactivity than the simple-TiO_2 coated cementitious composite. The simple TiO_2 coated specimens showed 68.7% bacterial inactivity as an *E. coli* count of approximately 0.502 ± 0.06 log reduction was observed at the end of 60 min experiment. Murillo et al. (2017) [436] reported comparable results, demonstrating the use of TiO_2-coated glass raschings for the inactivation of *E. coli*, achieving a similar log reduction by the end of its treatment period. In conclusion, the developed Fe_2TiO_5 Heterostructure exhibits effective antibacterial properties for addressing various indoor and outdoor organic contaminants.

4.2.5 Performance Evaluation of the Catalyst

The reaction rate constants were determined to evaluate the inactivation efficacy of the different catalysts, specifically TiO_2 and Fe_2TiO_5, utilized in this study. The rate constant for each of the processes is presented in Table 4.6. The Fe_2TiO_5 Heterostructure demonstrated a notably higher rate constant of 0.038 min^{-1}, in contrast to the simple-TiO_2 coated cementitious composite, which exhibited a rate constant of 0.0083 min^{-1}. Thus, the adequate performance of the Fe_2TiO_5 Heterostructure in comparison to a simple TiO_2-coated cementitious composite is clearly demonstrated. Also, the inactivation efficacy of the Fe_2TiO_5 Heterostructure was approximately

four times greater than that of the simple TiO_2-assisted photocatalysis-induced antibacterial process. Therefore, the high kinetic rate constant and the incorporation of waste iron as IWPs in this study render the Fe_2TiO_5 Heterostructure a highly appealing option for real-life/practical applications.

Table 4.6 Reaction rate constant (k) of different catalyst for *E. coli* inactivation under solar irradiation in the present study.

Treated Volume (mL)	Initial *E.coli* count (CFU/mL)	Catalyst	Intensity of light (W/m^2)	Treatment Time (min)	Reaction rate (k) constant (min^{-1})	Log reduction
250	10^6	TiO_2	590-600	60	0.0083	0.5
250	10^6	Fe_2TiO_5	590-600	60	0.038	2.3

4.2.5.1 Field Emission Scanning Electron Microscopy (FESEM) for *E. coli* Morphology and Potassium (K^+) Leakage Test

FESEM analysis was employed to directly examine the morphological variations in bacterial cells following treatment with Fe_2TiO_5 Heterostructure in deionized water. Figure 4.35a presents a FESEM picture of the untreated *E. coli* cells. The cells have consistent electron density, indicating they are in a standard state devoid of environmental disruption. On the contrary, the *E. coli* cells subjected to the Fe_2TiO_5 Heterostructure under identical conditions exhibited significant structural modifications during the cell dying/inactivation process. The cells treated with Heterostructure (shown in Figure 4.35b) got entirely disintegrated, leaving nothing but only plenty of fibriform cell fragments to be observed. The cellular fragments depicted in Figure 4.36b may have resulted from the lysis of bacterial cells, causing the release of compromised DNA molecules. This indicates that an effective oxidizing intermediate was generated to eradicate the bacterial cells in aqueous medium efficiently.

The outer cell membrane of *E. coli* consists of a lipopolysaccharide layer that serves a crucial function as a barrier to the permeability of Gram-negative bacteria. Potassium ions (K^+) are common in all bacteria and are essential for efficient protein synthesis and polysome formation regulations [437], [438]. Hence, the present study utilized the K^+ leakage test from *E. coli* to help

asses cell membrane permeability. The Fe_2TiO_5 Heterostructure may compromise the outer cell membrane and the cell wall via ROS, resulting in elevated cell permeability and the consequent leakage of intracellular chemicals, including K^+ [439]. The K^+ leakage tests (shown in Figure 4.34) of both initial (untreated) and final (treated) water were analyzed to compare the two distinct conditions.

In the absence of Fe_2TiO_5 catalyst, i.e., the control sample, K^+ leakage from *E. coli* cells was negligible (some cells may have sustained damage during the procedure), and the K^+ concentration remained reasonably steady for 90 min. The application of the Fe_2TiO_5 catalyst resulted in a progressive rise in K^+ concentration until 60 min of treatment, after which it stabilized despite additional treatment duration. In the present investigation, the K^+ ion leaked out immediately, and as the *E. coli* inactivated with the visible light treatment time, the concentration of leaked K^+ ions grew as well. The overall K^+ concentration, i.e., 123 ppm from the examined *E. coli*, was entirely released upon the complete inactivation of the *E. coli* bacterial cells after 60 min of visible light treatment, as illustrated in Figure 4.35. Thus, the outcome indicates that the permeability of the cell membrane was compromised due to the inactivation of *E. coli* cells.

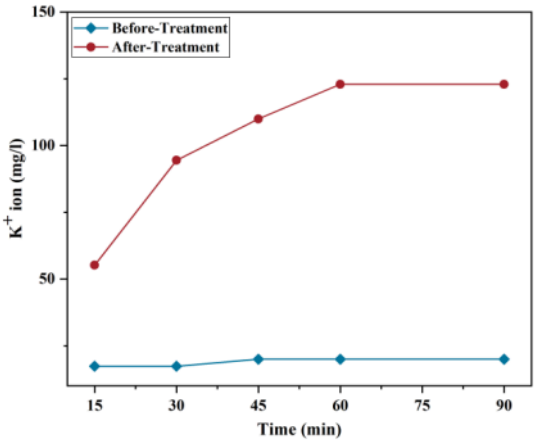

Figure 4.34 Leakage of K^+ ions from the cell damage before and after Fe_2TiO_5 Heterostructure-assisted treatment.

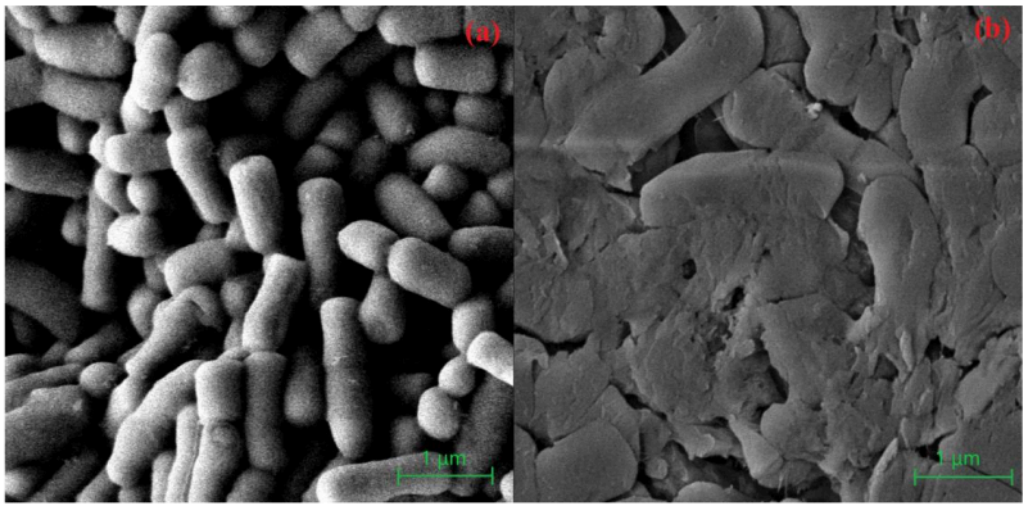

Figure 4.35 FESEM micrograph of *E. coli* before (a) and after (b) treatment.

4.2.5.2 Trapping Study: Generation and Impact of Different RoSs on Photocatalytic Performance of Fe_2tio_5 Heterostructure

Previous studies [440] indicate that bacteria are primarily inactivated through the release of ROS by semiconductor photocatalysts, which arises from the separation of e^- and h^+. Three primary ROSs serve an essential part in the photocatalytic disinfection of microorganisms: hole (h^+), superoxide radical ($•O_2^-$), and hydroxyl radical (•OH) [441]. Scavengers provide a valuable method for evaluating the role of these individual reactive species in the photocatalytic disinfection process and for defining its underlying mechanism.

Therefore, to identify the primary oxidative species (•OH, $•O_2^-$, and h+) involved in the photocatalytic *E. coli* disinfection using the Fe2TiO5 Heterostructure, a series of experiments were conducted under optimal conditions over a 45-min reaction period. Three quencher compounds were utilized: TBA for •OH , EDTA for h+, and BQ for $•O_2^-$, each at a concentration of 0.01 M. Identifying active oxide species involved in the photocatalytic disinfection process induced by Fe_2TiO_5 catalyst is a direct approach to validate the transfer mechanism of photo-generated charge carriers [442]. The trapping experiment of the Fe_2TiO_5 Heterostructure is illustrated in Figure 4.36.

The disinfection efficiency ratio of *E. coli* was 96% under blank conditions without scavengers, as illustrated in Figure 4.36. Different trapping agents resulted in varying disinfection efficiency ratios, indicating that all specified oxidative species contribute to the photocatalytic disinfection process of *E. coli*. The disinfection efficiency rates for *E. coli* were 81% following the addition of EDTA, 64% on BQ addition, and 13% after the addition of TBA. The *E. coli* removal efficacy varied significantly in the presence of BQ and TBA, demonstrating that the most active oxidative species in the Fe_2TiO_5 Heterostructure for photocatalytic disinfection were $\cdot O^{2-}$ and •OH . The introduction of EDTA resulted in a minimal shift in the reduction ratio, nearly 19%, indicating that the h^+ contributed little to the photocatalytic disinfection process of *E. coli*.

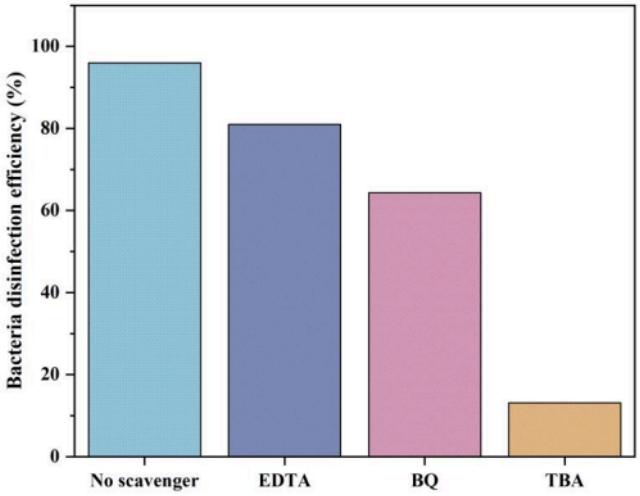

Figure 4.36 Investigation of several reactive oxygen species through trapping study.

4.2.5.3 Generation of OH Radicals At Different Time Intervals

The fluorescence spectroscopy was performed to confirm the photocatalytic relevance of the Fe_2TiO_5 Heterostructure by assessing the quantity of •OH formation at different time intervals under solar-visible light, as shown in Figure 4.37. The findings indicate that the intensity of •OH increased as the time increased from 0 to 60 min. Consequently, the higher concentration of •OH boosts the availability of adsorption surface sites for different organic contaminants and effectively captures the h^+ [443]. This significantly hinders the recombination of e^-/h^+ pairs,

thus enhancing the photocatalytic quantum efficiency of Fe_2TiO_5 Heterostructure and facilitating the degradation of targeted contaminants. Hence, the •OH spectra results of Fe_2TiO_5 Heterostructure correspond with its effective photocatalytic MB dye removal (section 4.2.3) and the solar-light assisted disinfection of *E. coli* (section 4.2.4) over different time intervals.

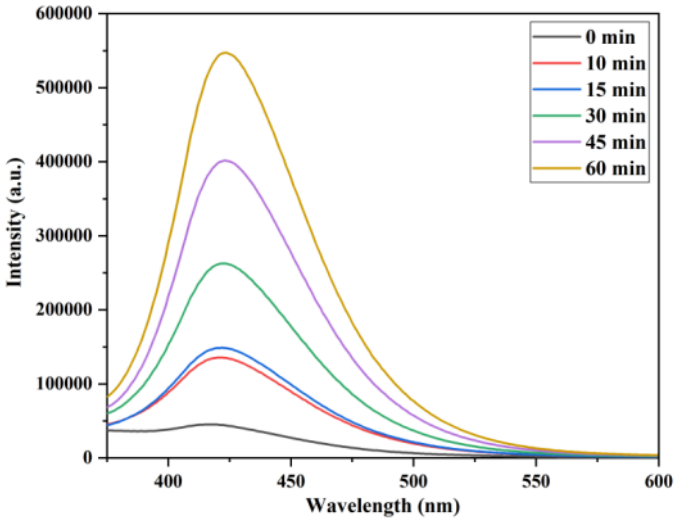

Figure 4.37 The •OH spectra obtained at different time intervals via fluorescence spectrophotometer

4.3 Section C: Photocatalytic Treatment of Bioaerosols Using Fe_2TiO_5 Heterostructure

This chapter examines the efficiency of the fabricated Fe_2TiO_5 heterostructure in inactivating *E. coli* bioaerosols within a room prototype glass reactor. This involves optimizing the experimental program and analyzing the impact of irradiation time on the photocatalytic inactivation efficiency of bioaerosols utilizing Fe_2TiO_5 heterostructure. The photocatalytic efficiency of the developed heterostructure was assessed compared to various predetermined boundary conditions for the treatment of bioaerosols.

4.3.1 Process Optimization

The recommended antibacterial protocol can be optimized based on factors such as time, light intensity, initial bacterial load, treating surface area, temperature, and humidity. Given the constraints associated with reactor design and the lab-scale implementation of bioaerosols treatment, this study investigated the optimization range for time, humidity, and temperature while maintaining a constant visible light intensity of 3.27 mW/cm^2 and an initial bacterial load at a maximum concentration of 10^9 CFU/ml. Furthermore, the current study employed an active-sampling method, and the optimized experimental program maintained the surface area of the Fe_2TiO_5 Heterostructure for cementitious composite at a maximum of 14 cm^2. Increasing the surface area within the same setup will enhance the system's efficiency. Thus, we investigated the efficiency of the Fe_2TiO_5 Heterostructure with minimal surface area and maximal bacterial load. Also, the experiments were conducted in triplicate and independently. (n = 3, mean ± SD)

Prior to examining the optimal treatment time for the maximum efficacy of the bioaerosol disinfection process, the most appropriate temperature and humidity range was assessed. The experimental results demonstrate that antibacterial activity was observed exclusively within a temperature range of 26 to 34°C and a humidity range of 50 to 74%. Observations were impossible during peak winter months (mid-December to mid-February), when maximum temperatures ranged from 8 to 12°C, and peak summer months (mid-April to the end of May), characterized by low humidity levels between 30 to 50%. During the specified period, failure results were observed in the experiments. Therefore, a temperature range of 26 to 34°C and humidity levels between 50% and 74% were established as critical parameters for the successful experimentation and observations in the present study.

4.3.2 Impact of Reaction Time on Disinfection Performance of Fe_2TiO_5 Heterostructure

The study examines the impact of visible light irradiation time on photocatalytic inactivation efficiency of bioaerosols using Fe_2TiO_5 Heterostructure, revealing optimal disinfection performance and the minimum and optimized disinfection time. Figure 4.38 presents the inactivation results of *E. coli* bioaerosols by the Fe_2TiO_5 Heterostructure, assessed under both dark and visible light conditions across different time intervals. The study's boundary condition

was established by conducting experiments under both dark and visible light conditions, utilizing uncoated-$C_{100}S_{100}$ cementitious samples.

4.3.2.1 Dark Experiments

The findings demonstrate that the $C_{100}S_{100}$ cementitious samples display the highest number of *E. coli* bacterial colonies in both visible-light and dark environments. Under dark conditions, an *E. coli* count of 0.028 ± 0.02, 0.028 ± 0.03, 0.031 ± 0.05, 0.035 ± 0.06, 0.041 ± 0.01, and 0.042 ± 0.03 log reductions was noted at the end of 10 min, 15 min, 30 min, 45 min, and 90 min, respectively. Also, exposure to visible light resulted in a minimal reduction in *E. coli* counts, with log reduction values of 0.29 ± 0.03, 0.029 ± 0.05, 0.036 ± 0.04, 0.038 ± 0.02, 0.049 ± 0.04, and 0.049± 0.02 observed after 10 min, 15 min, 30 min, 45 min, and 90 min, respectively. The observed minor reduction (<0.2 log reduction) in *E. coli* count may be due to the dying of sensitive cells, primarily resulting from osmotic shock in the reactor environment or bacterial cell adsorption on the outer surface of the uncoated-$C_{100}S_{100}$ cementitious samples.

4.3.2.2 Visible-light Experiments

Following the execution of boundary experiments, the disinfection efficiency of the Fe_2TiO_5 Heterostructure was evaluated, with results illustrated in Figure 4.38. The findings demonstrate that the Fe_2TiO_5 Heterostructure exhibited exceptional bioaerosols disinfection efficacy both under dark and visible light conditions, respectively. Under dark conditions, the Fe_2TiO_5 Heterostructure demonstrated an *E. coli* count of 0.096 ± 0.02, 0.124 ± 0.04, 0.201 ± 0.05, 0.301 ± 0.02, 0.481 ± 0.03, and 0.481± 0.02 log reductions at the end of 10 min, 15 min, 30 min, 45 min, 60 min, and 90 min, respectively. Whereas, under visible light, the Fe_2TiO_5 Heterostructure achieved log reduction values of 0.252 ± 0.04, 0.456 ± 0.02, 0.721± 0.02, 1.045 ± 0.04, 1.312 ± 0.03, and 1.312 ± 0.02 at 10 min, 15 min, 30 min, 45 min, 60 min, and 90 min, respectively. Based on the findings, it can be seen that the Fe_2TiO_5 Heterostructure exhibited a maximum efficiency of 67.2% and 90 ± 5% at the end of 60 min under dark and visible light exposure, respectively.

Also, it has been observed that after 60 min, the log reduction value of *E. coli* remained constant, indicating nearly complete disinfection of *E. coli* bioaerosols following 60 min of visible light irradiation on the Fe_2TiO_5 Heterostructure samples. Hence, the antibacterial property of the

Fe_2TiO_5 Heterostructure for cementitious composite is influenced by the duration of irradiation. As a result, the analysis reveals that the optimal time interval for achieving maximum bioaerosols disinfection efficiency using Fe_2TiO_5 Heterostructure is determined to be 60 min, based on the comparative analysis of different time intervals: 10 min, 15 min, 30 min, 45 min, and 90 min, under both dark and visible light conditions. Figure 4.40 displays optical images of Petri plates illustrating the reduction in *E. coli* bacterial colony growth at different exposure times with Fe_2TiO_5 Heterostructure.

Additionally, as illustrated in Figure 4.38, the initial rate of log reduction is slower, which subsequently increases with extended treatment time, thereby indicating the significance of reaction time in bacterial reduction. It is important to observe that the survival curve was not limited to a basic single exponential reduction process in relation to irradiation time, which is commonly observed in chemical oxidation processes (like photocatalytic degradation). The initial step of photocatalytic inactivation was slow, followed by a more rapid bacterial inactivation process. This aligns with prior research conducted by Wang et al. (2017) [442]. The study indicated that the photo-disinfection of *E. coli* occurs in two phases: an initial slower rate followed by a more rapid phase. The cell wall and cytoplasmic membrane are recognized as the primary targets of photo-generated ROSs. The complicated structure of these initial targets necessitates a degree of cumulative damage and requires a more significant number of radicals [444], [445]. Therefore, the initial step requires a considerable time frame, resulting in a noticeable delay in the profiles of bacterial inactivation. When oxidative damage sufficiently compromises the cell wall and membrane, intracellular materials within the cell begin to move out of the cells rapidly. This later ultimately leads to a rapid decline in cell viability.

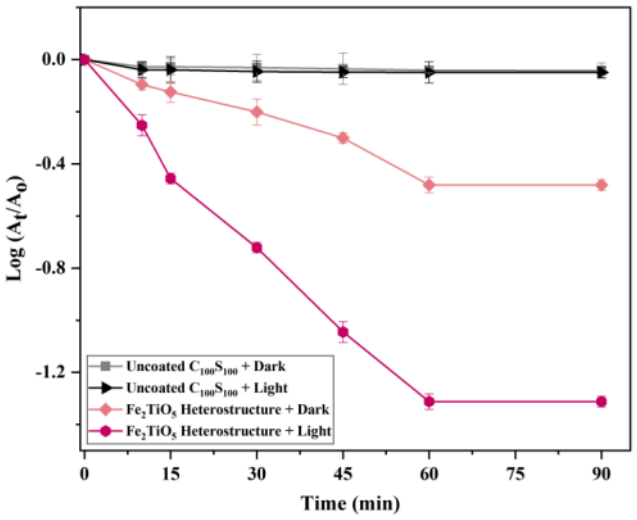

Figure 4.38 The impact of visible light irradiation time on photocatalytic inactivation efficiency of *E. coli* bioaerosols using Fe_2TiO_5 Heterostructure.

4.3.2.3 Rationale for the disinfection of bioaerosols using Fe_2TiO_5 Heterostructure under both dark and visible light conditions:

The observed dark inactivation (as discussed before in section 4.3.2.1.) may be associated with the act of adsorption on the Fe_2TiO_5 catalyst surface, as well as the inherent antibacterial properties of the Fe^{3+} ions within the Fe_2TiO_5 Heterostructure. Consequently, these two factors contributed to a certain level of disinfection activity by theFe_2TiO_5 Heterostructure in the absence of light.

The mechanism of visible-light-assisted bioaerosols disinfection utilizing Fe_2TiO_5 Heterostructure can be analyzed through various pathways, as multiple studies have presented distinct photocatalytic-induced antibacterial mechanism patterns. The primary factors contributing to the bioaerosols disinfection activity of the Fe_2TiO_5 Heterostructure in this study include the presence of surface hydroxyl groups (discussed in section (4.2.5.3)), the small particle size of the Fe_2TiO_5 nano-catalyst (section (4.2.2.8).), and alterations in the crystalline structures (discussed in section (4.2.1.1.)). The initial two factors have been presented

in numerous research papers [427], [432], [446], [447]: (a) After exposure to visible light, the generation of oxidative species such as •OH on the surface of the cementitious material takes place. The higher concentration of •OH increases the availability of surface sites for the adsorption of organic molecules, such as bacterial cell membranes, and effectively captures h+. This significantly hinders e-/h+ pair recombination, thereby enhancing photocatalytic quantum efficacy and resulting in the death of the cells. As discussed in section (4.2.2.9), the PL study demonstrated that the Fe_2TiO_5 catalyst inhibits the recombination of photo-generated e-/h+ pair. (b) The small size of the Fe_2TiO_5 nanoparticle is evidenced by the broadening peaks observed in the XRD (section 4.2.1.1) and TEM (section 4.2.2.2.) images. A reduction in the particle size results in an increase in its specific surface area (as discussed in section 4.2.2.8). An increased surface area results in improved interactions with bacteria, thereby enhancing the antibacterial efficacy of the Fe_2TiO_5 Heterostructure under visible light. (c) Moreover, the reduced band gap of the Fe_2TiO_5 Heterostructure (discussed in section 4.2.2.3) enhances its capacity for visible light absorption, expands its surface area, and leads to the formation of ROSs, causing damage to the bacterial cells. Thus, the bioaerosols disinfection capability of the Fe_2TiO_5 Heterostructure is solely attributable to its enhanced photocatalytic and intrinsic antibacterial abilities, as discussed in section 4.2.3. and 4.2.4.

4.3.3 Photocatalytic-Induced Antibacterial Efficiency Comparison

The antibacterial efficacy of the fabricated Fe_2TiO_5 Heterostructure against *E. coli* was examined through a series of experiments having controlled environmental conditions. The pre-determined boundary conditions explained in section (3.3.3) have been subjected to dark and visible light conditions for optimal 60 min irradiation time. The corresponding observations have been discussed in the following sections, and Figure 4.40 illustrates the obtained bacterial inactivation curve against each boundary condition. Also, Figure 4.39 displays optical images of petri dishes illustrating the growth of *E.coli* colonies after a 60 min exposure experiment to different specimens under visible light.

4.3.3.1 Under Dark

The *E. coli* culture was subjected to different trials where it was exposed to uncoated-$C_{100}S_{100}$ cementitious samples, uncoated-$C_{85}S_{85}$ cementitious samples, simple-TiO_2 cementitious samples, and Fe_2TiO_5 Heterostructure samples in the dark for the duration of 60 min. As illustrated by

Figure 4.40, no noticeable difference was observed for the uncoated-$C_{100}S_{100}$ and simple-TiO_2 cementitious specimens under the dark. An *E.coli* count of 0.042 ± 0.03 and 0.067 ±0.05 log unit reduction was observed for uncoated-$C_{100}S_{100}$ and simple-TiO_2 specimens, respectively. This marginal decrease in *E. coli* count noticed in both samples can be attributed to the adsorption of bacteria cells on the external surface of the cement mortar specimens. Furthermore, in the case of simple TiO_2 samples, the photocatalyst (TiO_2) activation necessitates some form of irradiation. In the absence of light, such activation is not achievable. However, the uncoated-$C_{85}S_{85}$ specimens demonstrated 17% antibacterial efficiency under dark. An *E.coli* count of 0.082 ± 0.09 log unit reduction was observed for the same specimens. This slight decrement in the *E.coli* counts by the uncoated-$C_{85}S_{85}$ samples may be attributed to the presence of Fe in the samples (as validated by SEM-EDS analysis in section (4.2.2.1.)). The bacterial cell absorbs Fe from the sample upon contact. This Fe is taken up as Fe^{2+} by non-specific porins in the cell's outer membrane. It is then transported into the cytoplasm [448], [449]. This results in a temporary disturbance of the Fe^{+2} balance within the cell [450], leading to some extent of bacterial inactivation.

After conducting the boundary experiments, the efficiency of the Fe_2TiO_5 Heterostructure was studied under dark conditions. According to the results (presented in Figure 4.41 & Table 4.7), the Fe_2TiO_5 Heterostructure reported an *E.coli* count of 0.481 ±0.06 log unit reduction. The specimens reduce bacterial survival by 69.33% without light. This is explained by the enhanced antibacterial properties of the Fe_2TiO_5 Heterostructure and the intrinsic antimicrobial characteristics of Fe [394], [451]. Prior studies conducted by [379], [381], [452]–[454] have found comparable findings, indicating that the Fe-modified TiO_2 photocatalyst demonstrates an antibacterial efficiency of 50-70% under dark. Previous studies (above-mentioned) have used traditional methods to synthesize the Fe-TiO_2 composite; however, this current research employs an inherent heterojunction formation strategy to fabricate the Fe_2TiO_5 Heterostructure.

4.3.3.2 Under Visible Light

As described before, comparable trials were conducted by subjecting the boundary experiments under visible light for 60 min. Based on the results (Figure 4.41 & Table 4.7), similar observations for uncoated-$C_{100}S_{100}$ and uncoated-$C_{85}S_{85}$ cementitious specimens have been noticed under visible light. Insignificant changes with an *E.coli* count of 0.049 ± 0.34 log unit

reduction were observed for the uncoated-$C_{100}S_{100}$ cementitious samples (same as a dark condition). Whereas, uncoated-$C_{85}S_{85}$ samples, when exposed to visible light, experienced a decrease of 15-17% (equivalent to the dark condition) in the number of viable *E.coli* bacteria count. Thus, according to the results, an *E.coli* count of 0.096 ± 0.04 log unit reduction was observed for the uncoated-$C_{85}S_{85}$ samples. The simple-TiO_2 cementitious specimens demonstrate an antibacterial efficiency of 23% with an *E.coli* count of 0.123 ± 0.03 log unit reduction under visible light. The low performance exhibited by simple TiO_2 samples can be related to the (TiO_2) photocatalyst's wide band gap, which leads to a higher occurrence of recombination reactions [455] and a slightly negative zeta potential [456]. As a result, the TiO_2 surface exhibits a repellent effect on the negatively charged bacterial cell membrane, leading to a lack of cell attachment on its surface.

Furthermore, the Fe_2TiO_5 Heterostructure showed remarkable antibacterial activity and effectively suppressed bacterial proliferation by 90-95% (Figure 4.41) under visible light conditions. A reduction of 1.312 ±0.03 log unit in *E. coli* count was observed for the samples. The Fe_2TiO_5 Heterostructure exhibits a narrower energy band gap due to the intrinsic production of Fe_2TiO_5 heterojunction, as verified by XRD and UV-DRS investigations in sections (4.2.1.1) and (4.2.2.3). This results in improved absorption of visible light and, hence, the production of highly reactive oxygen species (ROS), which induce damage to the bacterial cells. Figure 4.40 presents the optical pictures of petri plates depicting the formation of *E. coli* colonies following a 60 min exposure experiment to different specimens under visible light. A comparative investigation was conducted by [379], [381], [455], [457], [458], where authors obtained similar results, such that the synthesized Fe-TiO_2 composite could attain 90-98% antibacterial efficiency under visible light. However, the previously stated Fe-TiO_2 composite was synthesized using already established conventional techniques. In contrast, the present study yields the same results using a sustainable and economical approach to fabricate Fe_2TiO_5 photocomposite.

4.3.3.3 A Detailed Mechanism of Excitation of Fe_2TiO_5 Heterostructure And Its Bacterial Inactivation Under Visible Light

The detailed mechanism illustrating the bacterial inactivation and excitation of Fe_2TiO_5 Heterostructure under visible light is also shown in Figures 4.41a & 4.41b. The excitation mechanism of the Fe_2TiO_5 Heterostructure under visible light is triggered by the

transfer of electrons from the (Fe^{3+}/Fe^{4+}) energy level to the TiO_2's conduction band. The Fe^{3+} ion undergoes photo-absorption when it absorbs a photon with a wavelength $\lambda \geq 400nm$, producing Fe^{4+} ions and a TiO_2 electron conductive band (e_{cb}^-). The following reactions occur when Fe^{4+} reacts with the surface hydroxyl group to produce hydroxyl ion radical (°OH), while e_{cb}^- continues to react with adsorbed O_2 to make superoxide anion radicals ($°O_2^-$). However, they typically remain on the membrane and do not enter the bacterial cytoplasm. On the other hand, electrically neutral H_2O_2 can cross the cell membrane. Hydrogen radicals (H°) can remove hydrogen atoms from the fatty acids found in bacterial membrane lipids. Thus, the produced reactive oxygen species (ROS) exhibit high efficacy in eradicating bacteria by inducing lipid peroxidation, depleting glutathione, causing DNA damage, and ultimately leading to cell membrane breakdown [459]. This leads to the release of cellular contents, resulting in cell lysis and, ultimately, the death of cells [433]. The production of radical ions mainly occurs through the chemical reactions outlined in the following equations (4.24) to (4.37) when the Fe_2TiO_5 Heterostructure is exposed to visible light irradiation.

$$TiO_2 + h\nu \rightarrow e^- + h^+ \quad \textbf{4.23}$$

$$h^+ + H_2O \rightarrow H^+ + \dot{O}H \quad \textbf{4.24}$$

$$Fe^{3+} + e^- \rightarrow Fe^{2+} \quad \textbf{4.25}$$

$$Ti^{3+} \rightarrow e^- + Ti^{4+} \quad \textbf{4.26}$$

$$Fe^{2+} + O_{2(abs)} \rightarrow Fe^{3+} + \dot{O}_2^- \quad \textbf{4.27}$$

$$Fe^{2+} + Ti^{4+} \rightarrow Fe^{3+} + Ti^{3+} \quad \textbf{4.28}$$

$$Fe^{3+} + h_{vb}^+ \rightarrow Fe^{4+} \quad \textbf{4.29}$$

$$Fe^{3+} + h\nu \rightarrow Fe^{4+} + e^- \quad \textbf{4.30}$$

$$Fe^{4+} + OH^- \rightarrow Fe^{3+} + \dot{O}H \quad \textbf{4.31}$$

$$e^- + O_2 \rightarrow \dot{O}_2^- \quad \textbf{4.32}$$

$$\dot{O}_2^- + e^- + H^+ \rightarrow H_2O_2 \quad \textbf{4.33}$$

$$e^-_{(Iron\ Oxide)} + H_2O_2 \rightarrow \dot{O}H + OH^- + Iron\ Oxide \quad \textbf{4.34}$$

$$e^-_{(Iron\ oxide)} + Fe^{3+} \rightarrow Iron\ oxide + Fe^{2+} \quad \textbf{4.35}$$

$$Radical\ ions + Organic\ compound \rightarrow CO_2 + H_2O \quad \textbf{4.36}$$

Therefore, iron in the Fe_2TiO_5 Heterostructure enhances the oxidative stress caused by TiO_2, producing free radicals. This, in turn, increases the antibacterial activity of the Fe_2TiO_5

photocatalyst. Hence, the findings indicated in Table 4.7 suggest that the developed Fe_2TiO_5 Heterostructure has excellent antibacterial efficacy in dark and visible light environments.

Table 4.7 Photocatalytic efficiency comparison of different specimens under dark and visible light conditions.

S.No.	Boundary Condition	Findings	Efficiency
1	uncoated-$C_{100}S_{100}$	No activity both under light and dark condition	1.5%
2	uncoated-$C_{85}S_{85}$	Executed antibacterial property both under light and dark condition	15-17%
3	simple-TiO_2 cementitious specimens	No activity under dark condition. However, some photocatalytic activity has been observed under light.	1.33% (Dark) & 23% (Light)
4	Fe_2TiO_5 Heterostructure	Excellent antibacterial plus photocatalytic property has been noted both under dark and light condition.	69.33% (Dark) & 90±5 % (Light)

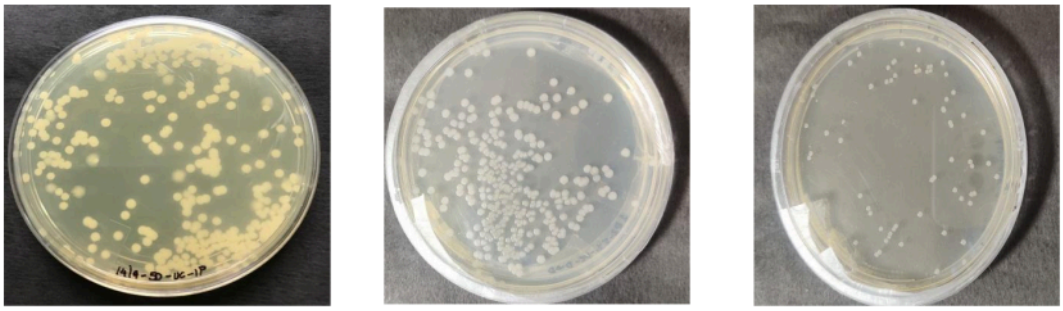

uncoated-$C_{85}S_{85}$ P25-TiO_2 Fe_2TiO_5 heterostructure

Figure 4.39 The Petri dish images illustrate the development of *E. coli* colonies following a 60-min exposure to several specimens under visible light.

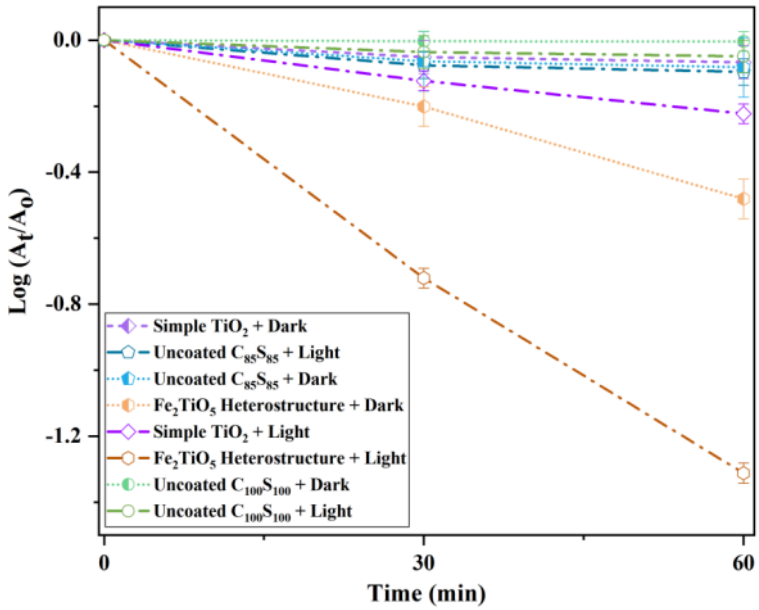

Figure 4.40 The bacterial inactivation curve of uncoated-$C_{85}S_{85}$, simple-TiO_2, and Fe_2TiO_5 Heterostructure samples under dark and visible light conditions.

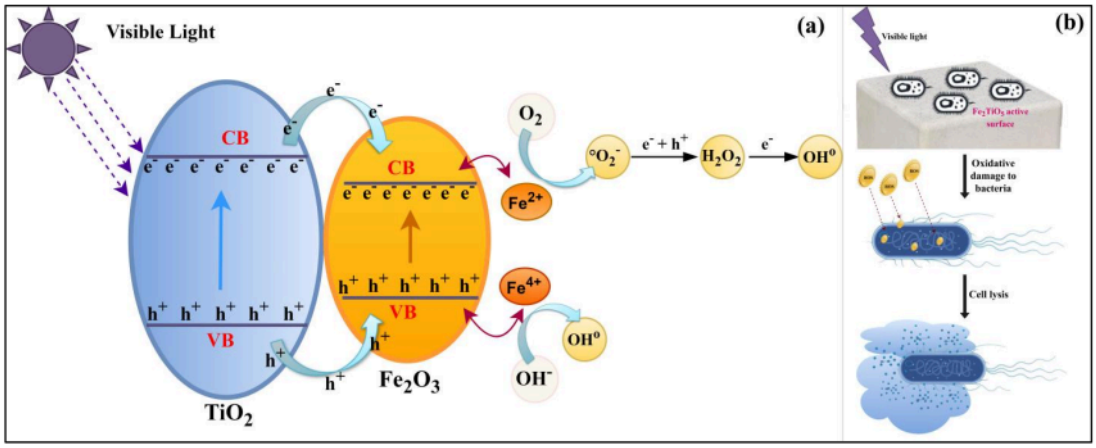

Figure 4.41 Graphic representation of (a) photocatalytic mechanism of Fe_2TiO_5 Heterostructure under visible light (CB: conduction band and VB: valence band), (b) antibacterial mechanism of Fe_2TiO_5 Heterostructure.

4.3.4 Performance Evaluation of the Different Catalyst

This section of the study aimed to assess the catalytic performance of various catalysts (Fe, TiO_2, and Fe_2TiO_5) with regard to their efficacy in inactivating *E. coli* bioaerosols under visible light conditions. In this context, the reaction rate constants of the various catalysts were assessed to evaluate their respective inactivation efficiency in the present study. The rate constant for each process is detailed in the Table 4.8. The Fe_2TiO_5 Heterostructure exhibited a considerably high rate constant (k) value of 0.022 min^{-1}, compared to the simple-TiO_2 coated and uncoated-C75S75 cementitious composite, which showed rate constants of 0.0021 min^{-1} and 0.0016 min^{-1}, respectively. Hence, the effective performance of the Fe_2TiO_5 catalyst, when compared to the simple TiO_2 and Fe catalysts, is evidenced. Also, the inactivation efficacy of the Fe_2TiO_5 Heterostructure was approximately twice that of the simple TiO_2-assisted antibacterial disinfection process. Thus, the boosted kinetic rate constant and the integration of waste iron as IWPs in this study make the Fe_2TiO_5 Heterostructure a desirable option for practical applications in real-world scenarios.

Table 4.8 Reaction rate constant (k) of different catalyst for *E. coli* bioaerosols disinfection in the present study.

Pollutant	**Catalyst**	**Light source**	**Intensity of light (mW/cm^2)**	**Treatment Time (min)**	**Reaction rate (k) constant (min^{-1})**	**Log reduction**
E. coli K12	Fe	Visible light	3.27	60	0.0016	0.096
E. coli K12	TiO_2	Visible light	3.27	60	0.0021	0.123
E. coli K12	Fe_2TiO_5	Visible light	3.27	60	0.022	1.312

4.3.5 Durability Studies of Fe_2TiO_5 Heterostructure

The current investigation presents a significant finding concerning the extensive durability of the Fe_2TiO_5 Heterostructure, particularly in its ability to demonstrate a long-term in-situ heterojunction active-oxide layer effect. To validate our theory, we conducted parametric optimization studies utilizing the Fe_2TiO_5 Heterostructure, which had been employed for a minimum of 45 cycles. In the recycling tests, the reported approach validates both the sustainability of the cementitious composite as a catalyst-supporting material and the stability of the TiO_2 coating over the cementitious composite. The efficiency of the Fe_2TiO_5 Heterostructure in terms of recyclability was assessed through its ability to disinfect *E. coli* bioaerosols across multiple cycles, with the findings illustrated in the Figure 4.42.

The findings reveal that during the initial 20 cycles of reuse, the Fe_2TiO_5 Heterostructure exhibited only a 9% reduction in its photo-activity (i.e., disinfection of *E. coli* bioaerosols), as illustrated in the Figure 4.42. After this, a reduction of 11% was observed for the next 10 recycles, followed by a 12.4% reduction for the subsequent 5 recycles and, thereafter, a 13% reduction for the next 10 recycles. This moderate reduction can be linked to the weathering of the catalyst within the Heterostructure [460]. Hence, the results validate that an adequate quantity of Fe_2TiO_5 catalyst particles remained adhered to the surface, even within the recycled Heterostructure cementitious composites. The integrity and stability of TiO_2 within the Heterostructure were also confirmed through a range of characterization procedures outlined in the following section, verifying the existence of photocatalysis in the system. The results indicate the substantial assurance of this technology for large-scale studies.

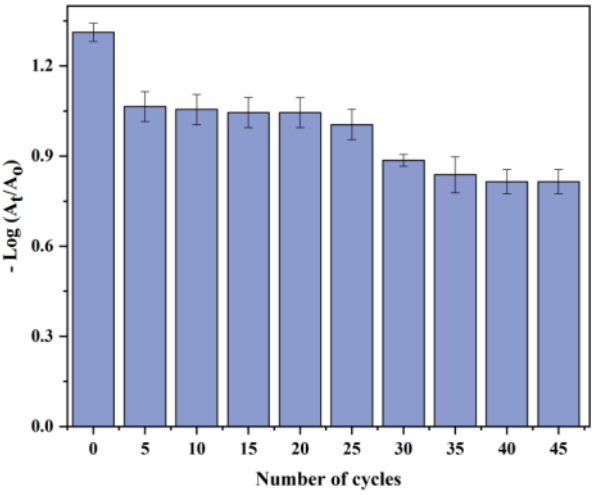

Figure 4.42 Evaluation of the recyclability of Fe_2TiO_5 heterostructure for the inactivation of *E. coli* bioaerosols.

4.3.5.1 Characterization of Recycled Fe_2TiO_5 Heterostructure For Cementitious Composites

The integrity of catalyst particles (Fe and TiO_2) in recycled Heterostructure samples (45 recycles) was evaluated against fresh Heterostructure samples using various characterization techniques, as detailed below:

4.3.5.2 SEM-EDS Analysis of Recycled Fe_2TiO_5 Heterostructure

SEM-EDS analysis was conducted to verify the elemental composition and examine the surface morphology of the Fe_2TiO_5 Heterostructure samples, including both freshly coated and recycled variants. A comparatively smooth surface has been noted in the SEM impression (Figure 4.43) of both specimens, confirming the existence of TiO_2 and its integrity even post-recycling. The prominent peaks of titanium (Ti), iron (Fe), and oxygen (O) elements observed in the EDS image of both fresh and recycled Heterostructure samples validate the presence and unification of the targeted materials, namely Fe and TiO_2. The existence of iron in both Heterostructure samples can be associated with the utilization of IWPs in the fabrication process of cementitious composites.

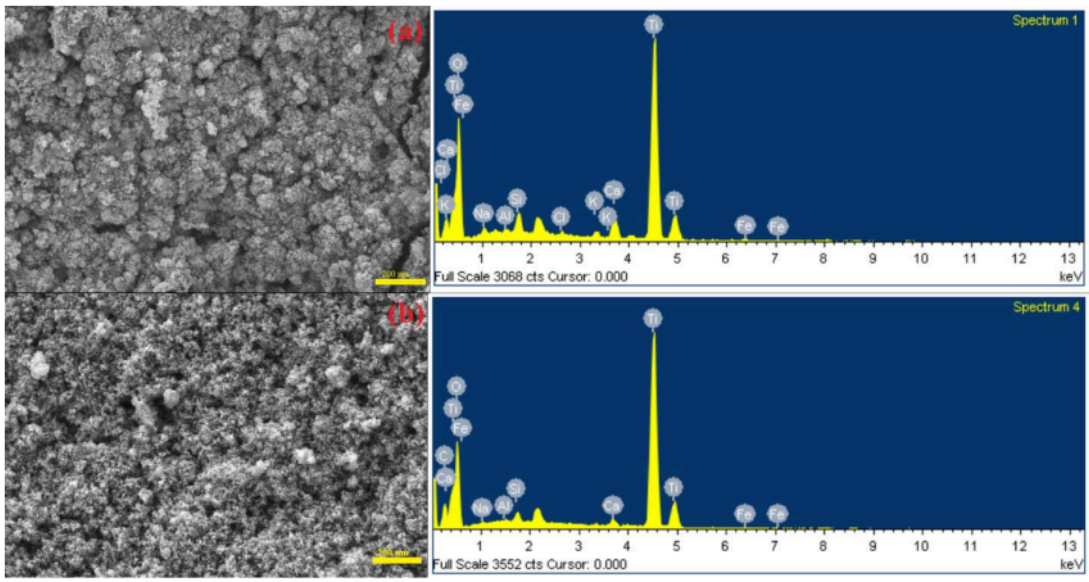

Figure 4.43 SEM-EDS impression of (a) Freshly-coated and (b) recycled Fe_2TiO_5 Heterostructure

4.3.5.3 XRD Analysis of Recycled Fe_2TiO_5 Heterostructure

The XRD analysis was performed on both the freshly coated and recycled Fe_2TiO_5 Heterostructure to verify the preservation of TiO_2 crystalline planes, even after 45 recycles, as illustrated in Figure 4.44. The detection of anatase (A) and rutile (R) diffraction phases in both the freshly coated and recycled Fe_2TiO_5 Heterostructure samples indicates that the integrity of TiO_2 and its photocatalytic activity in the recycled samples were preserved, even after 45 recycles. Furthermore, the detection of diffraction peaks corresponding to iron titanium oxide (ITO) and iron oxide (IO) reinforces the presence of both iron and TiO_2 in the samples analyzed. The IO peaks also explain the capturing of photo-excited electrons ($e^-_{(Iron\ Oxide)}$) by Fe^{3+} ions during the TiO_2 photocatalytic process, resulting in the generation of Fe^{2+} ions. The presence of ITO peaks further validates that the naturally occurring Fe_2TiO_5 heterojunction oxide layer on the outer surface of the cementitious composite remained active and intact even after 45 recycles. Thus, the XRD results of the recycled Fe_2TiO_5 Heterostructure sample demonstrate the expanded viability of the surface-active Fe_2TiO_5 heterojunction oxide layer. The presence of NaTO and SiTO peaks can be attributed to the bonding/interactions among TiO_2 and the various components of cement and IWPs utilized to prepare cementitious composites.

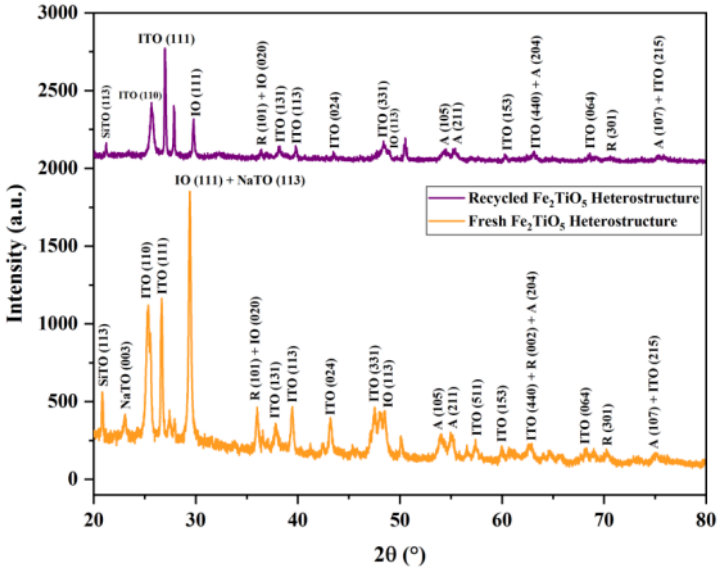

Figure 4.44 The XRD pattern of Freshly-coated and recycled Fe_2TiO_5 Heterostructure.

4.3.5.4 UV DRS Analysis of Recycled Fe_2TiO_5 Heterostructure

UV–vis. Diffuse reflectance spectroscopy (UV-DRS) was performed to determine the energy band gap of the Fe_2TiO_5 Heterostructure (fresh) before and after recycling across the spectral range of 200 to 800 nm, with the results presented in Figure 4.45. The baseline of the samples was set using the reference compound Barium sulfate ($BaSO_4$). The results indicate a reduction in the energy band gap of both Heterostructure samples relative to P25–TiO_2. This transition illustrates the potential of Fe_2TiO_5 Heterostructure samples to function photocatalytically within the visible light spectrum. However, it is due to the occurrence of Fe within the intricate crystalline framework of the Fe_2TiO_5 Heterostructure, causing higher valence electrons in Fe^{3+} than Ti^{4+} and thus prompting the filling up of new energy levels []. The absorption spectrum of P25–TiO_2 was observed at 416 nm, which subsequently shifted to 460 nm and 480 nm before and after recycling the Fe_2TiO_5 Heterostructure samples, respectively. The energy band gap of TiO_2 was measured at 3.05 eV, which decreased to 2.57 eV for the freshly coated sample and further reduced to 2.33 eV for the recycled Fe_2TiO_5 Heterostructure for cementitious composite.

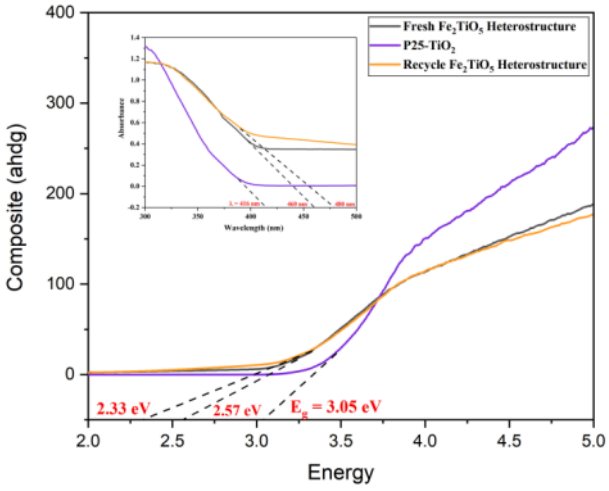

Figure 4.45 UV-DRS plot of P25-TiO_2, fresh and recycled Fe_2TiO_5 Heterostructure.

4.3.5.5 FTIR Analysis of Recycled Fe_2TiO_5 Heterostructure

The FTIR spectra of the freshly coated and recycled Fe_2TiO_5 Heterostructure were examined to identify the vibrational bonds in both cementitious systems, as illustrated in Figure 4.46. The presence of Ti-O-Ti vibrational bonds in both sample spectra is shown through several peaks between 400 and 1200 cm^{-1} wavenumbers, thus confirming the existence of the TiO_2 lattice. The TiO_2 anatase phase for the freshly coated and recycled Heterostructure samples was observed in the spectra at 451 cm^{-1} and 467 cm^{-1} wavenumber, respectively. These findings agree with a prior study [427] that demonstrated the existence of Ti-O-Ti vibrations, specifically in the anatase phase, within the range of 400 to 640 cm-1wavenumber. These bands are essential for enhancing the photocatalytic capabilities in the Fe_2TiO_5 Heterostructure samples [415]. Also, the peak at 555 cm^{-1} wavenumber indicates Fe-O vibrational bonds in the IR spectra of both fresh and recycled Fe_2TiO_5 Heterostructure samples. The Fe-O-Ti bond was detected at 2023 cm^{-1} and 2038 cm^{-1} wavenumber, confirming the existence of Fe in the recycled Heterostructure sample. Bansal et al. (2018) [408] also reported a comparable peak of the Fe-O-Ti bond in its Fe-TiO_2 clay beads.

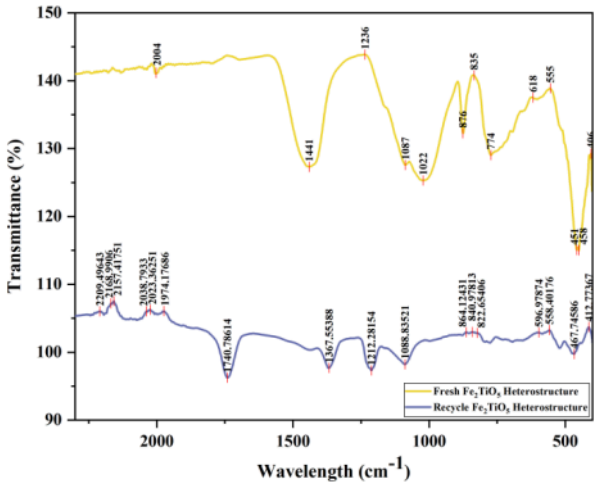

Figure 4.46 FTIR spectra of freshly-coated and recycled Fe_2TiO_5 Heterostructure.

4.3.6 Cost Analysis

Table 4.10 presents a comprehensive analysis of the costs of collecting materials necessary to produce one cubic meter of iron-rich cementitious mortar specimens. The cost of materials was estimated based on current prices from local vendors in Noida, UP, and TIET, Patiala, who provided the materials. OPC and IWPs were packaged in 50 kg bags, and the cost per kg was calculated accordingly. Sand was acquired at the rate of per cubic foot, and its cost per kg was calculated. The superplasticizer was obtained in 20 kg drums, and the associated costs were estimated comparably. Transportation costs were incorporated into the per-kilogram cost of all materials. The total cost for each element was calculated by multiplying the unit cost listed in Table 4.9 by the quantity needed to produce one cubic meter of iron-rich cementitious mortar specimens. Table 4.10 provides a summary of this overall cost.

The findings in Table 4.10 indicates that as the percentage replacement of IWPs (particularly BS) increased from $C_{85}S_{85}$ to $C_{60}S_{85}$, the total cost of the iron-rich cementitious specimens reduced compared to the control mix $C_{100}S_{100}$. The overall material cost dropped from 6.69% for $C_{85}S_{85}$ to 14.08% for $C_{60}S_{85}$ compared to the control mix $C_{100}S_{100}$ while preserving the strength and durability of the iron-rich cementitious materials.

Table 4.9 Cost per kg for materials utilized in the iron-rich cementitious mortar production

Materials	Cost per Kg	
	Rupee (₹)	US Dollar ($)
OPC	8	0.092
FA	1	0.012
BS	4.4	0.051
Sand	1.36	0.016
BS	1.5	0.017
Water	0.02	0.00023
SP	44	0.51

* The exchange rate between the US dollar and the Indian rupee is 86.96.

Table 4.10 Cost for producing one cubic meter of iron-rich cementitious building material

Mix design	OPC (₹/m^3)	Sand (₹/m^3)	FA (₹/m^3)	BS (₹/m^3)	FS (₹/m^3)	Water (₹/m^3)	SP (₹/m^3)	Total cost (₹/m^3)	Total cost ($/$m^3$)	% change w.r.t. $C_{100}S_{100}$ (control mix)
$C_{100}S_{100}$	4216	2150.2	0	0	0	5.27	58.08	6429.5	73.93	0
$C_{85}S_{85}$	3583.2	1827.6	52.7	116.2	355.7	5.27	58.08	5998.7	68.98	(+)6.69
$C_{80}S_{85}$	3372.8	1827.6	52.7	231.8	355.7	5.27	58.08	5904.1	67.89	(+)8.17
$C_{75}S_{85}$	3161.6	1827.6	52.7	348.04	355.7	5.27	58.08	5809.1	66.8	(+)9.64
$C_{70}S_{85}$	2951.2	1827.6	52.7	463.7	355.7	5.27	58.08	5714.4	65.71	(+)11.11
$C_{65}S_{85}$	2740.4	1827.6	52.7	579.7	355.7	5.27	58.08	5619.5	64.62	(+)12.61
$C_{60}S_{85}$	2529.6	1827.6	52.7	695.6	355.7	5.27	58.08	5524.6	63.53	(+)14.08

4.3.7 Mathematical Models used in *E. coli* Bioaerosols Inactivation

The present research compares various kinetic disinfection models with experimental data, linking the results to key operating parameters that influence the disinfection efficacy of the current system. The kinetic parameters, including k from the log-linear model and δ from the

double Weibull model, were utilized to compare various techniques for fitting the *E. coli* inactivation results. The findings of this research offer valuable insights through the analysis of inactivation rates, kinetic parameters, and fitting parameters, such as regression distribution (R^2) and root mean square deviation (RMSD), to understand the mechanisms of *E. coli* inactivation. Figure 4.48 demonstrates that all applied mathematical models exhibited a strong fit when utilizing the Fe_2TiO_5 Heterostructure in the photocatalytic disinfection process under dark and visible light conditions. The double Weibull and biphasic distributions exhibited the best fit, as indicated by R^2 values of 0.992 for both models and RMSD values of 0.066 and 0.068, respectively.

Comparison of the k values (Table 4.10) from the fitted curve for the log-linear and biphasic distributions indicates that the inactivation rate was more rapid under visible light ($k = 0.04\ min^{-1}$; d = 57.57 min) than in dark conditions ($k = 0.01\ min^{-1}$; d = 230.3 min). Comparative analysis of the δ values from the fitted curves of the Weibull and double Weibull distributions indicates that the disinfection rate of *E. coli* is higher under visible light conditions than in dark conditions, as demonstrated in the table. The results obtained from these techniques are perfectly fitted using a double Weibull distribution. This model assumes the presence of two distinct sub-population groups: sub-population 1, consisting of sensitive cells that inactivate over a short period (δ_1), and sub-population 2, which is more resistant and requires a longer duration to inactivate (δ_2). Each group exhibits different levels of resistance to the disinfection treatment conditions. Furthermore, biphasic parameters for the visible condition supported the theory as mentioned above, indicating that the inactivation rate for the first subpopulation/phase ($k_{1max} = 0.07\ min^{-1}$) was higher than that of the latter phase ($k_{1max} = 0.04\ min^{-1}$). Often observed in the context of microbial adaptation or the emergence of resistant subpopulations [428]. Thus, the results indicate the potential of Fe_2TiO_5 Heterostructure technology for disinfection of *E. coli* bioaerosols under visible light irradiation.

Table 4.11 Kinetic parameters of mathematical models used in the inactivation of *E. coli* bioaerosols subjected to (a) dark and (b) visible light irradiation treatment.

Treatment	Model	K_1 (min^{-1})/ δ_1 (min)	K_2 (min^{-1})/ δ_2 (min)	R^2/RMSD
Dark	L (k)	0.01	--	0.984/0.025
	W (δ)	192.15	--	0.991/0.017
	DW (δ)	192.15	192.15	0.995/0.018
	B (k)	0.01	0.01	0.968/0.032
Visible	L (k)	0.04	--	0.905/0.19
	W (δ)	42.81	--	0.953/0.137
	DW (δ)	34.29	32.86	0.992/0.066
	B (k)	0.07	0.04	0.991/0.068

4.3.8 Remark

When exposed to visible light, the Fe_2TiO_5 heterostructure showed exceptional antibacterial capabilities in neutralizing *E. coli* bioaerosols. Within 60 min, , the Fe_2TiO_5 heterostructure reduced bioaerosols by 1.312 log units. Additionally, as confirmed by a number of analytical tools, the heterostructure showed exceptional durability and recyclability, surpassing 45 cycles. This implies that it could be used commercially to remove biological pollutants from indoor environments.

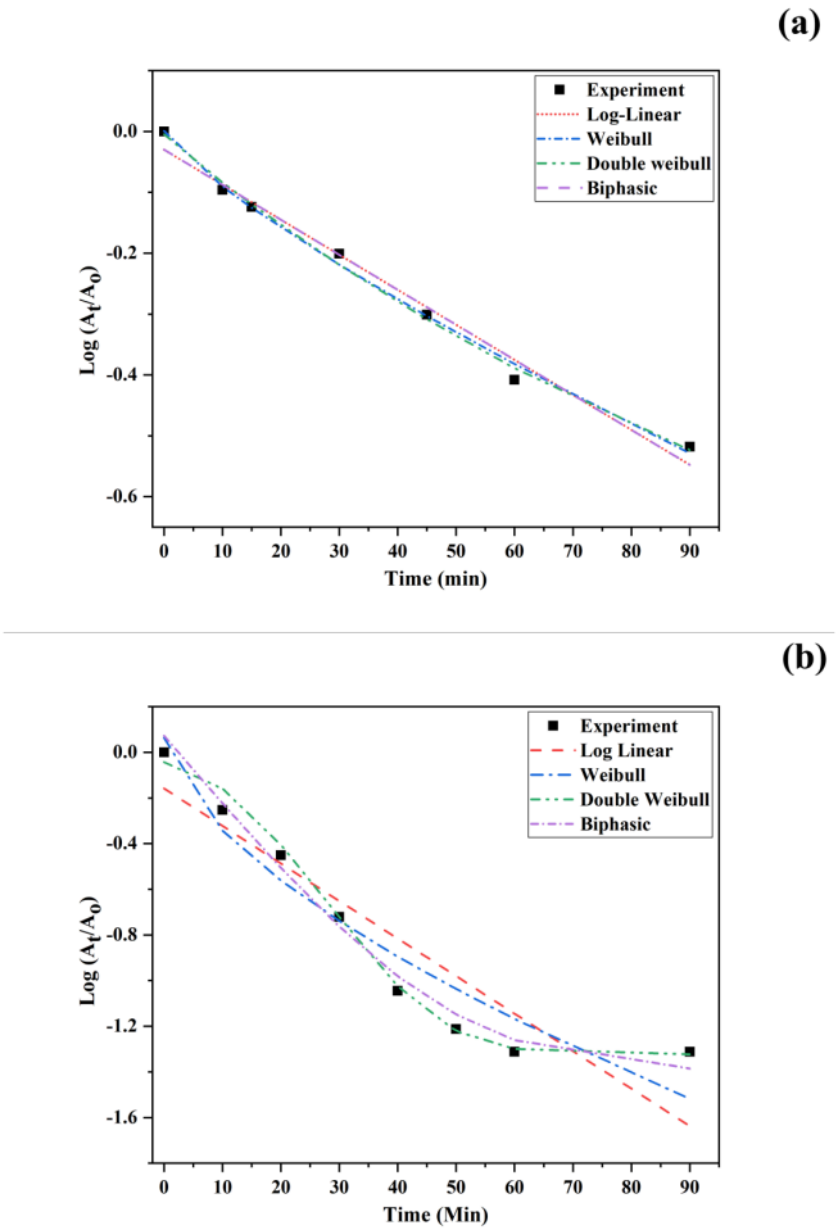

Figure 4.47 Fitting mathematical models to the inactivation curve of *E. coli* bioaerosols subjected to (a) dark and (b) visible light irradiation treatment.

Chapter 5

Conclusion

5.1 Over-view

The present study introduces a novel concept of inherent heterojunction formation process, such that the fabricated surface-active Fe_2TiO_5 heterostructure executes photocatalytic and antimicrobial properties under the visible light spectrum. The study explored the potential application of economically viable Fe_2TiO_5 heterostructure, such that, it can be utilized efficiently for inactivating *E.coli* bioaerosols in indoor environments. The developed antimicrobial and sustainable cementitious construction material comprises of cement, sand, iron-rich industrial waste products (FA, FS, and BS) and TiO_2 as an active photocatalyst. The primary objective of the present research study was to assess the suitability of the developed iron-rich cementitious material as a sustainable construction material, specifically in terms of its durability and strength properties. The findings are indicated in section (5.2) such that, the iron-rich cementitious material contributes to environmental sustainability by promoting circular economy and green building practices.

Following that, the cementitious specimens underwent TiO_2 coating. The resulting Fe_2TiO_5 heterostructure for cementitious composite was then analyzed using various analytical tools like XRD, HRTEM, UV-DRS, and soon. Also, the photocatalytic and antibacterial property check were also executed on the developed heterostructure (both before and after TiO_2 coating), and a detailed result and discussion was accomplished. The results (section (5.3)) demonstrated the durability and effectiveness of the Fe_2TiO_5 heterostructure as a photocatalytic material under visible light spectrum. Furthermore, the bioaerosols inactivation efficiency of the fabricated Fe_2TiO_5 heterostructure was confirmed via a series of disinfection experiments. The results discussed in section (5.4) reveal that the Fe_2TiO_5 heterostructure executes excellent antimicrobial properties in inactivating *E. coli* bioaerosols under dark and visible light conditions. Hence, it can be concluded that the fabricated Fe_2TiO_5 heterostructure on cementitious composite is economically, ecologically, and sustainably viable to be utilized as a construction material for the remediation of various indoor microbial contaminants.

The following primary conclusions can be drawn from each section of the current study based on the various experimental tests conducted.

5.2 Section A: Fabrication of Iron-Rich Cementitious Mortar

- The results indicate that the utilized IWPs, i.e., FA, BS, and FS, have a substantial impact on the physical and mechanical properties of the developed iron-rich cementitious composite material.
- The cementitious mortar mix $C_{85}S_{85}$ exhibited superior strength and durability characteristics compared to the reference mix design $C_{100}S_{100}$. Therefore, it is recommended that the mortar mix $C_{85}S_{85}$ effectively use FS, BS, and FA as substitutes for sand and cement in sustainable building materials.

➢ **Fresh Properties**

- The fresh properties of the different IWP-modified mortar mixtures indicated that the slump value increased with higher levels of BS replacement, thereby enhancing workability and cohesiveness.
- The fresh density of various IWPs-modified mortar mixtures showed a slight decrease, which can be attributed to the lower density of the incorporated SCMs (FA and BS).

➢ **Strength Properties**

- The study indicated that the mix $C_{85}S_{85}$ exhibited superior compressive strength compared to other cementitious mortar mixtures, achieving values of 36.2 N/mm^2 at 28 days and 50.8 N/mm^2 at 56 days.
- The split tensile strength of IWPs-modified cementitious mortar specimens at 7 and 28 days demonstrated that the $C_{85}S_{85}$ mix, which had 5% BS replacement, exceeded the reference $C_{100}S_{100}$ mortar mix. Other mortar mix ($C_{80}S_{85}$ to $C_{60}S_{85}$) had lower split tensile strength after that. As a result, the design mix $C_{85}S_{85}$ demonstrated an optimum outcome with split tensile strengths of 1.98 N/mm^2 at 7 days and 3.8 N/mm^2 at 28 days.
- The flexural strength results of IWPs-modified cementitious mortar specimens at 7 and 28 days of curing indicated that the mix $C_{85}S_{85}$ demonstrated higher 28-day flexural strength relative to the reference mix $C_{100}S_{100}$. The data indicate that increasing BS content beyond 5% results in a reduction of flexural strength.

- It can be concluded that varying levels of BS replacement affect the flexural strength of IWPs-modified cementitious mortar specimens in a manner similar to their impact on compressive and split tensile strength. Therefore, the mix $C_{85}S_{85}$ produces the most favorable results, demonstrating flexural strengths of 3.58 N/mm^2 and 4.69 N/mm^2 at 7 and 28 days, respectively.

➢ **Physical Properties**

- The 28-day porosity results for the IWPs-modified design mixes indicated that the reference mix $C_{100}S_{100}$ achieves a porosity of 16.31%, and an increase in the BS replacement level beyond 5% ($C_{85}S_{85}$ mix) resulted in a proportional increase in its value.
- The 28-day real and bulk density for different IWPs-modified design mixes decreased as the replacement level of BS increased yet remained within the range of 2000–2500 kg/m3, confirming its suitability for normal cement mortar class. The results suggest that proposed mortar mixes can make low-density building materials.
- The dry bulk density of the IWPs-modified cementitious mortar specimens at 28 days exhibited a reduction in dry density as the BS replacement level of IWPs-modified mixes increased compared to the reference $C_{100}S_{100}$ mix.

➢ **Durability properties**

- The 28-day water absorption by immersion capacity of the various IWPs-modified design mixes exhibited a comparable trend. The results indicated that increased levels of BS substitution corresponded with higher water absorption values via immersion. The mix C85S85 attained the optimal water absorption value of 5.84% compared to other IWPs-modified mixes.
- This suggests that the compressive strength results of the mix $C_{85}S_{85}$ in the present study align well with its durability and physical properties results. Therefore, the mortar mix $C_{85}S_{85}$ demonstrated superior durability and strength properties than the reference mix $C_{100}S_{100}$.

➢ **Microstructure analysis**

- The SEM results demonstrate that the microstructure of various mix designs enhanced and became denser with the incorporation of IWPs at all curing ages. The voids reduction and compressive strength enhancement in the mix $C_{85}S_{85}$ positively influence its

durability properties. The increased formation of CSH gel in the mix $C_{85}S_{85}$ is directly associated with its better compressive strength and lower permeability properties.

- The XRD results demonstrate that all IWPs-modified mix designs exhibited crystalline behavior at 28 and 56 days. No significant phase transition was observed with the increasing percentages of BS replacement levels across various IWPs-modified mix designs. All mixes exhibited the formation of a substantial peak of quartz characterized by its hexagonal crystal structure. Additional hydrated phases identified include calcium hydroxide, calcium carbonate, calcium silicate hydrate, and gismondine.
- The TGA data indicate that the mass loss pattern with rising temperature is uniform across all IWPs-modified mortar samples.

5.3 Section B: Fabrication and Analytical Examiation of Fe_2TiO_5 Heterostructure For Cementirtious Composite.

This section verified the stability and the potency of the Fe_2TiO_5 heterostructure as photocatalytic and antimicrobial material under visible light spectrum.

➢ **Analytical Examination**

- The detection of both Fe and TiO_2 elements in the Fe_2TiO_5 heterostructure confirms the development of the surface-active Fe_2TiO_5 heterojunction oxide layer on the cementitious composite. This was validated through XRD, XPS, FTIR, Raman spectra, and EDS with elemental mapping.
- The presence of ITO peaks in XRD analysis confirmed that iron was naturally integrated into the TiO_2 lattice, resulting in the formation of an active layer of Fe_2TiO_5 heterojunction oxide on the outer surface of the cementitious composite.
- In the FTIR spectra of the Fe_2TiO_5 heterostructure, the peaks observed at 2309 cm-1 and 2332 cm-1 signify the formation of Ti–O–Fe vibrational bonds. These bonds, resulting from the intrinsic heterojunction process, provide further evidence for the presence of Fe within the cementitious heterostructure.
- Using EDS, elemental mapping, and XPS, elements such as Ti, O, Fe, Na, Si, and Fe were identified on the outer surface of the Fe_2TiO_5 heterostructure.
- The crystallite size of Fe_2TiO_5 nanoparticles was determined to be 31.203 nm for the anatase phase and 34.95 nm for the rutile phase. The calculated lattice parameters for

Fe_2TiO_5 heterostructure nanoparticles closely agree with the reference TiO_2, measuring 3.78 Å for a (=b) and 9.51 Å for c. This indicates that Fe has been integrated into the TiO_2 lattice without altering the average unit cell dimension.

- The TEM images reveal that the Fe_2TiO_5 nanoparticles exhibit a highly crystalline structure and a non-spherical morphology, with an average particle size ranging from 13 to 34.5 nm. The observed lattice spacing of 0.35 nm and 0.25 nm correspond to the crystalline plane of (101) TiO_2 anatase and (110) hematite structures, indicating a favorable lattice compatibility at the interface between TiO_2 and Fe_2O_3.
- UV-DRS results revealed that the Fe_2TiO_5 heterostructure functions effectively under visible spectrum light with an energy band gap of 2.57 eV.
- The BET analysis indicated that the surface area of the Fe_2TiO_5 heterostructure was determined to be 73.757 $m^2 g^{-1}$, with a pore volume of 9.1 x 10^{-2} cm^3/g.
- The PL spectrum analysis of Fe_2TiO_5 heterostructure showed a reduction in the recombination rate and an enhancement in its charge separation efficiency, suggesting that a considerable quantity of photo-induced e- and h+ contributes to photochemical changes, thereby improving its photocatalytic and antibacterial properties under the visible spectrum of light.

➢ **Photocatalytic inactivation**

- The photocatalytic efficacy of the Fe_2TiO_5 heterostructure was evaluated by analyzing the degradation of methylene blue (MB) in aqueous solutions under solar-visible light exposure.
- The findings indicated that the presence of the Fe_2TiO_5 heterostructure improved the photocatalytic decolorization of MB under solar-visible light.
- A progressive reduction in the principal absorption peak of MB dye at 668 nm, together with a corresponding lightening of the MB solution's color, was noted as the duration of irradiation increased.
- An effective photocatalytic degradation of MB was achieved with the Fe_2TiO_5 heterostructure, which exhibited a 93.1% MB removal rate at the end of 60 min, in contrast to 68% for simple P25-TiO_2 coated specimens.

- Also, the study examined the kinetics of MB degradation using Fe_2TiO_5 catalysts, revealing a linear correlation and a significant increase in reaction rate constant (0.029 min-1) compared to TiO_2-coated cementitious composite (0.015 min^{-1}).

➢ **Antibacterial property check**

- The antibacterial efficiency of the Fe_2TiO_5 heterostructure was assessed utilizing an aliquot of *E. coli* bacterial suspension in a batch reactor under solar-visible light irradiation.
- The findings indicate that the Fe_2TiO_5 heterostructure samples exhibited remarkable bacterial inactivation performance of 99%. A log reduction of 2.301 ± 0.04 was achieved at the end of the 60 min experiment.
- The study also evaluated the bacterial inactivation efficacy of TiO_2 and Fe_2TiO_5 catalysts. The Fe_2TiO_5 heterostructure showed a higher rate constant of 0.038 min^{-1} than a simple TiO_2-coated cementitious composite (0.0083 min^{-1}). Its inactivation efficacy was four times greater than the TiO_2-assisted photocatalysis-induced antibacterial process, making it an appealing option for real-life applications.
- The trapping experiments demonstrated that the antibacterial efficacy of *E.coli* removal varied significantly with BQ and TBA scavengers, with $\cdot O_2^-$ and •OH identified as the most active oxidative species in the Fe_2TiO_5 heterostructure for photocatalytic disinfection process.
- Fluorescence spectroscopy showed an increase in •OH intensity, enhancing photocatalytic efficiency of Fe_2TiO_5 heterostructure and, thereby, aiding in the degradation of MB dye and solar-light-assisted disinfection of *E. coli* in water.
- Hence, the Fe_2TiO_5 heterostructure on cementitious composite material presents an innovative approach aiming to address different environmental challenges and promote a sustainable, low-carbon footprint.

5.4 Section C: Photocatalytic Treatment of Bioaerosol Using Fe_2TiO_5 Heterostructure.

- **Indoor application**

- The indoor antimicrobial efficacy of the Fe_2TiO_5 heterostructure was evaluated by neutralizing *E. coli* bioaerosols.
- The optimized conditions established for the disinfection of *E. coli* bioaerosol under visible light in a glass reactor included a visible light intensity of 3.27 mW/cm^2, an initial bacterial load at a maximum concentration of 10^9 CFU/ml, a temperature range of 26 to 34 °C, a humidity range of 50 to 74%, and an active sampling method.
- The optimized condition demonstrated a 1.312 log reduction of *E. coli* bioaerosols within a 60 min reaction time.
- The photocatalytic disinfection comparison results demonstrated that the Fe_2TiO_5 heterostructure displays superior antimicrobial characteristics relative to uncoated-$C_{85}S_{85}$ and simple TiO_2 cementitious specimens.
- The findings demonstrated that the simple-TiO_2 cementitious specimen attained an antibacterial efficiency of merely 23% under visible light, exhibiting no activity in dark conditions. In contrast, the Fe_2TiO_5 heterostructure achieved an antimicrobial efficiency of 69.33% in the dark and between 90-95% under visible light.
- The Fe_2TiO_5 heterostructure exhibited a considerably high rate constant (k) value of 0.022 min^{-1}, compared to the simple-TiO_2 coated and uncoated-$C_{85}S_{85}$ cementitious composite, which showed rate constants of 0.0021 min^{-1} and 0.0016 min^{-1}, respectively.
- The overall cementitious material cost dropped from 6.69% for $C_{85}S_{85}$ to 14.08% for $C_{60}S_{85}$ compared to the control mix $C_{100}S_{100}$ while preserving the strength and durability of the iron-rich cementitious materials..
- Therefore, the broader applications of the novel Fe_2TiO_5 heterostructure for the disinfection of indoor biological contaminants validate its potential for commercial-scale implementation.

- **Durability studies**
  - The Fe_2TiO_5 heterostructure demonstrated a remarkable durability and recyclability, exceeding 45 cycles throughout this study, as validated by various analytical tools, including XRD, FTIR, UV-DRS, XRD, FTIR, UV-DRS, and SEM-EDS.
  - Hence, the enhanced durability and stability of the Fe_2TiO_5 heterostructure further underscore its potential for commercial applications.

5.5 Recommendation

The Fe_2TiO_5 heterostructure for cementitious composites demonstrates significant potential for disinfecting indoor biological contaminants, specifically bioaerosols. The utilization of waste materials such as FA, FS, and BS as alternative sources of Fe presents a commendable recycling and reuse strategy for reducing hazardous solid waste in the environment. Hence, future research is expected to employ additional waste materials from the environment, either as alternative Fe sources or as efficient binding agents for developing more resilient catalyst-immobilized supports.

Furthermore, future research should focus on a comprehensive technological and economical assessment to facilitate the large-scale application of Fe_2TiO_5 heterostructure in addressing different types of indoor microbial contaminants, utilizing more durable and practical cementitious composite materials. The application of the present study Fe_2TiO_5 heterostructure for cementitious composites, combined with an optimized reactor design for large-volume processing, could boost the advancements in indoor air treatment utilizing advanced oxidation technology.

The scale-up studies will demonstrate the efficacy of the in-situ heterojunction information concept in addressing various types of indoor microbial pollutants. However, real validation necessitates the design of practical reactors and the implementation of actual field-scale trials.

Thesis for plag check (1).docx

ORIGINALITY REPORT

10%	5%	9%	2%
SIMILARITY INDEX	INTERNET SOURCES	PUBLICATIONS	STUDENT PAPERS

PRIMARY SOURCES

1	Shelly Tiwari, Anoop kumar, Gurbir kaur. "Photocatalytic Inactivation of Bio-Aerosol Using Surface-Active Iron-Titanium Thin Film Immobilized on Sustainable Cementitious composite", Ceramics International, 2024 Publication	3%
2	Jun Chen, Chi-sun Poon. "Photocatalytic construction and building materials: From fundamentals to applications", Building and Environment, 2009 Publication	2%
3	www.mdpi.com Internet Source	1%
4	Marcin Janczarek, Łukasz Klapiszewski, Patryk Jędrzejczak, Izabela Klapiszewska, Agnieszka Ślosarczyk, Teofil Jesionowski. "Progress of functionalized TiO2-based nanomaterials in the construction industry: A comprehensive review", Chemical Engineering Journal, 2022 Publication	1%

5	ira.lib.polyu.edu.hk Internet Source	<1%
6	www.researchgate.net Internet Source	<1%
7	fastercapital.com Internet Source	<1%
8	Hanan H. Mohamed, Nuhad A. Alomair, Sultan Akhtar, Tamer E. Youssef. "Eco-friendly synthesized α-Fe2O3/TiO2 heterojunction with enhanced visible light photocatalytic activity", Journal of Photochemistry and Photobiology A: Chemistry, 2019 Publication	<1%
9	Shelly Tiwari, Anoop Kumar, Gurbir Kaur. "Visible light-responsive photocatalytic-based sustainable construction material for environmental remediation", Ceramics International, 2022 Publication	<1%
10	P. C. Thomas, Vishal John Mathai, Geevarghese Titus. "Emerging Technologies for Sustainability", CRC Press, 2020 Publication	<1%
11	Jorge H. Martínez-Montelongo, Iliana E. Medina-Ramírez, Yolanda Romo-Lozano, Juan Antonio Zapien. "Development of a	<1%

sustainable photocatalytic process for air purification.", Chemosphere, 2020
Publication

12	Tsion Amsalu Fode, Yusufu Abeid Chande Jande, Thomas Kivevele. "Effects of different supplementary cementitious materials on durability and mechanical properties of cement composite – Comprehensive review", Heliyon, 2023 Publication	<1 %
13	www.esp.org Internet Source	<1 %
14	files.library.northwestern.edu Internet Source	<1 %
15	ebin.pub Internet Source	<1 %
16	Achraf Amir Assadi, Oussama Baaloudj, Lotfi Khezami, Naoufel Ben Hamadi, Lotfi Mouni, Aymen Amine Assadi, Achraf Ghorbal. "An Overview of Recent Developments in Improving the Photocatalytic Activity of TiO2-Based Materials for the Treatment of Indoor Air and Bacterial Inactivation", Materials, 2023 Publication	<1 %
17	Vaca, Norma Yolanda Gaibor. "Alkali Activation of Ceramic Solid Wastes to	<1 %

Incorporate in Non-Structural Panels", Universidade do Minho (Portugal), 2024
Publication

18	etd.lib.metu.edu.tr Internet Source	<1%
19	Harsh V. Patel, Myles Greer, Brian Brazil, Wenzheng Yu, Sameer Hamoush, Lifeng Zhang, Renzun Zhao. "Adsorption capacity and mechanism of modified coal flyash (CFA) for per- and polyfluoroalkyl substances (PFAS) in landfill leachate", Journal of Hazardous Materials, 2025 Publication	<1%
20	Hashemi, Mohammad. "Engineering Characteristics of Modified Rollercompacted Concrete Pavement", University of Malaya (Malaysia), 2023 Publication	<1%
21	Submitted to The Hong Kong Polytechnic University Student Paper	<1%
22	isc.rsu.lv Internet Source	<1%
23	www.emmason247.com.ng Internet Source	<1%
24	biotechuv.com Internet Source	

		<1%
25	doc.provincia.pu.it Internet Source	<1%
26	mdpi-res.com Internet Source	<1%
27	www.science.gov Internet Source	<1%
28	Junjie Sun, Yang Hu, Mengfan Guan, Yanbei Hou, Shihua Zhang, Xiuyu Liu, Gang Tang. "Research progress in the application of bulk solid waste in the field of flame retardation", Journal of Environmental Chemical Engineering, 2023 Publication	<1%
29	Marcin Janczarek, Łukasz Klapiszewski, Patryk Jędrzejczak, Izabela Klapiszewska, Agnieszka Ślosarczyk, Teofil Jesionowski. "Progress of functionalized TiO2-based nanomaterials in the construction industry: A comprehensive review", Chemical Engineering Journal, 2021 Publication	<1%
30	ir.canterbury.ac.nz Internet Source	<1%

Exclude quotes	On	Exclude matches	< 10 words
Exclude bibliography	On		